Department of Physics and Astronomy
Heidelberg University

Bachelor Thesis in Physics
submitted by

Lukas Schulz

born in Mayen (Germany)

2025

Topological lattice defects and vortex statistics during supersolid formation in simulations of dilute 2D Bose gases

This Bachelor Thesis has been carried out by Lukas Schulz at the
Kirchhoff Institute for Physics in Heidelberg
under the supervision of
Prof. Thomas Gasenzer

Abstract

In this thesis, we analyze the formation of supersolids in a dilute, planar ^{164}Dy BECs with magnetic dipole-dipole interaction after instantaneous quenches of the s-wave scattering length by solving the eGPE numerically with the split-step Fourier method. Particularly, we extract the algebraic scaling coefficients of the topological lattice defect number $N_D(t) \propto (t - t^*)^\alpha$ as a function of time in the late-time scaling regime in both the droplet and honeycomb phase with a bootstrap fit in datasets with different condensate contrast. Additionally, we quantify the increase in lattice bond angular order post quench and observe algebraic scaling of the angular correlation function $g_6(r) \propto r^{-\eta_6}$, indicative of a hexatic system. Finally, the formation of vortices is investigated in the droplet phase, where we find the vortex number to be described by a Gaussian distribution throughout the time evolution of the condensate post quench. While the interaction between vortices and droplets is significant on small length scales, we find symmetries in the charge sensitive inter-vortex distance distributions and they follow generalized Wigner-Dyson distributions in the limit of large separations.

Zusammenfassung

In dieser Arbeit untersuchen wir die Entstehung von Suprasoliden in planaren ^{164}Dy BEKs mit magnetischer Dipol-Dipol Wechselwirkung nach sprunghafter Änderung der s-Wellen Streulänge, indem die eGPE numerisch mit der split-step Fourier Methode gelöst wird. Insbesondere bestimmen wir die Skalierungsexponenten der Anzahl der topologischen Defekte $N_D(t) \propto (t - t^*)^\alpha$ als Funktion der Zeit im Regime später Zeiten, sowohl in der Tröpfchen- als auch der Bienenwabenphase mit einem Bootstrap Fit in Datensätzen mit unterschiedlichem Kontrast. Außerdem quantifizieren wir die Zunahme der Gitterordnung nach der Änderung der s-Wellen Streulänge und beobachten die algebraische Skalierung der Winkelkorrelationsfunktion $g_6(r) \propto r^{-\eta_6}$, kennzeichnend für hexatische Systeme. Schließlich untersuchen wir die Entstehung von Vortices in der Tröpfchenphase. Hier zeigt sich, dass die Verteilung der Vortexanzahl während der Zeitentwicklung nach der Änderung der s-Wellen Streulänge durch eine Gauß-Verteilung gegeben ist. Auf kleinen Längenskalen gibt es signifikante Wechselwirkungen zwischen Tröpfchen und Vortices. Trotzdem finden wir Symmetrien in den ladungssensitiven inter-Vortex Distanzverteilungen. Diese folgen generalisierten Wigner-Dyson Verteilungen im Limit großer Abstände.

Contents

List of Abbreviations

2D **2**-**D**imensional.

3D **3**-**D**imensional.

BEC **B**ose-**E**instein **C**ondensate and **B**ose-**E**instein **C**ondensation.

DDI **D**ipole-**D**ipole **I**nteraction.

eGPE **e**xtended **G**ross-**P**itaevskii **E**quation.

FFT **F**ast-**F**ourier-**T**ransform.

List of Figures

List of Tables

***Nota bene*:** Throughout this thesis, many integrals will appear, and integration bounds are given only when absolutely necessary. For integrals without an integration domain, the notation $\int \mathrm{d}^n\mathbf{r}$ is understood to include an appropriate integration domain, which will become clear from the context.

Statutory declaration:

I declare that I have authored this thesis independently and that I have used only those sources and resources explicitly quoted.

Eidesstatlich Erklärung:

Ich versichere, dass ich diese Arbeit selbstständig verfasst und keine anderen als die angegebenen Quellen und Hilfsmittel benutzt habe.

Heidelberg, den 14.10.2025 Lukas Schulz

Errata

The following corrections have been made post submission:

Eq. (2.18) Correction of the Fourier transform of the 2D DDI potential, $\tilde{U}_{dd}^{2D}(\tilde{\mathbf{k}}_\perp) \to \tilde{U}_{dd}^{2D}(\mathbf{k}_\perp)$, as derived in Eq. (B.22).

Eq. (C.5) Correction of the effective LHY correction amplitude in computational units by a factor of $1/\pi$, $\gamma_{QF}^{eff} \to 1/\pi \cdot \gamma_{QF}^{eff}$, by the definition of γ_{QF}.

Neither correction influences the results obtained in this thesis as both equations have been implemented correctly in the code executing them.

1 Introduction

Ever since their first theoretical prediction a century ago [1–3], Bose-Einstein condensates (BECs) have played a central role in the development of quantum many-body theory. By condensing into the lowest energy state, all particles making up a BEC can be described by a single wavefunction, which gives rise to interesting quantum phenomena at macroscopic scales. Ranging from early descriptions of superfluidity in helium-4 (^{4}He) [4] and superconductivity [5] to modern applications in cosmology as a means to describe dark matter and dark energy [6], BECs have found their way into many areas of modern theoretical physics.

The advent of powerful laser cooling and trapping techniques [7–10] led to the first experimental realizations of BEC in dilute atomic alkali metal gases of sodium, rubidium, and lithium in 1995 [11–14]. Both the development of efficient trapping and cooling systems as well as the realization of BEC in dilute atomic gases resulted in a Nobel Prize in Physics in 1997 and 2001, respectively [15, 16]. Today, BECs are routinely produced worldwide and are a powerful tool in experimental physics. A review of experimental results concerning BEC with additional dipole interaction may be found in [17].

Ever-increasing computational resources have also introduced the possibility to study BEC by simulations [18–26]. Although computationally expensive, simulations avoid costly and complex experimental infrastructure and provide excellent control over system parameters. We will use numerical methods to simulate a trapped BEC of a dilute dysprosium-164 (^{164}Dy) gas with magnetic dipole interaction. We consider a trapping potential such that the condensate assumes a two-dimensional (2D) shape and restrict dynamics to this plane.

BEC often leads to superfluidity. Although neither phenomenon implies the other [27], superfluidity is often associated with BEC. Apart from being able to flow without viscosity, a peculiar property of superfluids is that their rotation is restricted to quantized eddies called vortices [7, 28]. Superfluids have been observed as early as 1938 [4, 29, 30], with important theoretical framework established in the 1940s [31, 32]. Their first realization in dilute gases followed in 1999 [33] and was verified by the observation of vortices. A comprehensive review of superfluidity may be found in [34]. Vortices can arise in a condensate when it is subjected to sudden changes in a control parameter. We will instantaneously quench the so-called s-wave scattering length (see Sec. 2.2), and track and count vortices throughout the simulated time evolution to obtain vortex number and spacing distributions.

In the 2D geometry, the interplay of contact interactions and dipole-dipole interactions as well as quantum fluctuations can lead to another striking phenomenon known as supersolidity. By breaking translational symmetry, a crystal-like, periodic lattice structure forms in the condensate. The concept of supersolidity was pioneered well after the theoretical establishment of superfluidity [35, 36]. Unlike BEC and superfluidity, the first unambigu-

ous experimental confirmation of supersolidity did not take place in helium [37, 38], but was first realized in condensates of dilute gases in 2017 [39, 40]. While supersolids display solid-like properties through their crystal-like lattice structure, under the circumstances we will consider in this work, they may still exhibit superfluid properties. A condensate in the supersolid phase is still a superfluid, while realized in a dilute atomic gas, as recently demonstrated [41]. Crucially, a condensate in a supersolid state can support the existence of vortices, as we shall demonstrate later. The supersolid phase is special in the sense that it requires the breaking of two symmetries. While the superfluid phase breaks phase invariance, a supersolid additionally breaks continuous translational invariance. We analyze, in the present work, the formation of supersolid lattice structures under different initial conditions. Particularly, we quantify the increase of bond orientational order and the decay of lattice defects in the time evolution of a condensate after forcing it from a uniform state into a supersolid state by instantaneous quenches of the s-wave scattering length.

After a brief introduction to Bose-Einstein condensation in general, we begin by introducing important concepts for modeling a 2D Bose gas with magnetic dipole interaction, foremost the extended Gross-Pitaevskii equation (eGPE) in Sec. 2, and proceed by outlining how to numerically simulate such a system and extract observables of interest, i.e. lattice defects and vortices, in Sec. 3. The results of our defect coarsening analysis are presented in Sec. 4. Sec. 5 is concerned with vortex spacing and number distributions. Supplementary material and mathematical derivations may be found in the Appendix. Here, we also supply basic MATLAB code for numerically finding vortices and lattice defects.

2 Modeling a 2D dipolar Bose gas

2.1 Introduction to Bose-Einstein condensation - a primer

Bose-Einstein condensates have found their way into standard textbook knowledge. Nonetheless, we want to set the stage for our later discussion of 2D planar Bose-Einstein condensates by briefly introducing the concept in general, following closely the derivations presented in [2, 28].

Consider a non-interacting ideal gas of N_{tot} Bosons with mass m, confined to a Volume V. The phase space accessible to a particle with energy E in this system can be written as

$$\Phi(E) = \int_V \mathrm{d}^3\mathbf{r} \int_{E(\mathbf{p})\leq E} \mathrm{d}^3\mathbf{p} = V \cdot \frac{4}{3}\pi \left(2mE\right)^{3/2}, \tag{2.1}$$

by integrating over the confining volume and all possible momenta and using that $E(\mathbf{p}) = \frac{1}{2m}(p_x^2 + p_y^2 + p_z^2)$ in terms of momentum $\mathbf{p} = (p_x, p_y, p_z)^\top$. Note that this dispersion relation is distinctly non-relativistic as we operate in the low energy limit at

small temperatures. If we now quantize phase space in volumes of h^3, we can introduce the density of states $g(E)$, i.e. the number of possible phase space states between E and $E + \mathrm{d}E$, as

$$g(E) = \frac{1}{h^3}\frac{\mathrm{d}\Phi(E)}{\mathrm{d}E} = V\frac{2\pi}{h^3}(2m)^{3/2}E^{1/2}. \tag{2.2}$$

Since we are dealing with bosons, we know that the probability to find a Boson at a given energy and temperature T follows a Bose-Einstein distribution,

$$f_{BE}(E) = \frac{1}{e^{(E-\mu)/k_BT} - 1}, \tag{2.3}$$

for chemical potential μ and Boltzmann constant k_B. With these distributions, we can express the number of bosons at energy E as $N(E) = f_{BE}(E)g(E)$ such that the total number of bosons in our system is given by

$$N_{tot} = \int_0^\infty \mathrm{d}E\, N(E) = V\,\frac{2\pi}{h^3}(2m)^{3/2}\int_0^\infty \mathrm{d}E\,\frac{E^{1/2}}{e^{(E-\mu)/k_BT} - 1}. \tag{2.4}$$

Introducing $z = e^{\mu/k_BT}$, we show in Sec. A that this integral is solved by a power series in z,

$$N_{tot} = V\,\frac{2\pi}{h^3}(2m)^{3/2}\cdot(k_BT)^{3/2}\,\Gamma\left(3/2\right)\sum_{k=1}^{\infty}\frac{z^k}{k^{3/2}}, \tag{2.5}$$

with $\Gamma(x)$ denoting the gamma function. As the Bose-Einstein distribution Eq. (2.3), being a probability distribution, is required to be positive for all E by Kolmogorov's axioms, z is subject to the boundary conditions $0 \leq z \leq 1$. Surprisingly, this yields an upper bound on the total boson number if we set $z = 1$,

$$N_{tot} \leq N_{tot}^{max} = V\frac{2\pi}{h^3}(2mk_BT)^{3/2}\Gamma\left(3/2\right)\zeta\left(3/2\right) \tag{2.6}$$

if we recognize the Riemann zeta function $\zeta\left(\alpha\right) = \sum_{k=1}^{\infty} k^{-\alpha}$ [42]. Note that both $\Gamma(3/2) = \sqrt{\pi}/2$ [7, 43] and $\zeta(3/2) \approx 2.612$ [7, 28] are finite numbers. N_{tot}^{max} is also denoted the critical particle number N_c. However, we do not make any assumptions on the total number of Bosons initially, so there must be a flaw in the argument. The problem starts in Eq. (2.4). Essentially, we assume a continuum of states in the large N_{tot} limit. While this is true at finite energy[1] in the large N_{tot} limit, replacing a sum over discrete energy levels with an integral over a continuous energy spectrum fails to accurately capture the behavior at $E \to \mu$. More rigorously, a system of bosons has a discrete excitation spectrum corresponding to energy levels E_i such that we can write

$$N_{tot} = \sum_{i=0}^{\infty} N_i(E_i) = \sum_{i=0}^{\infty} g_i(E_i)f_{BE}(E_i), \tag{2.7}$$

[1] By finite energy, we mean $E - \mu > 0$.

where $N_i(E_i)$ the occupancy of energy level E_i, $g_i(E_i)$ the degeneracy of energy level E_i and $f_{BE}(E_i)$ the Bose-Einstein distribution evaluated at E_i. Here is where Einstein's realization comes in. There should be no reason as to why we cannot add single particles to the system consecutively. As the total number of particles at finite energy is constrained by above reasoning, the additional particles must 'condense' into the lowest energy state. This is possible as the Bose-Einstein distribution diverges at $E \to \mu$ from above.
This argument may be reversed in the sense that we keep the total number of bosons fixed and read Eq. (2.6) as a function of temperature. If we denote T_c the critical temperature below which $N_{tot} > N_c$, then

$$T_c = \frac{h^2}{2m\pi k_B} \left(\frac{N_{tot}}{V\zeta\left(\frac{3}{2}\right)} \right)^{2/3}. \tag{2.8}$$

Hence, if we cool a system of Bosons with constant particle number N in a constant volume V below the critical temperature T_c, Bose-Einstein condensation sets in. At $T < T_c$, the fraction of bosons in the lowest energy state is given by

$$\frac{N_0}{N_{tot}} = \frac{N_{tot} - N_c}{N_{tot}} = 1 - \left(\frac{T}{T_c} \right)^{3/2}, \tag{2.9}$$

since N_c particles will be excited to energy states unequal to the lowest possible energy state. N_0/N_{tot} is called the condensate fraction.
This condensation has profound consequences. Although we are dealing with macroscopic ensembles, which in experimental realizations have $\mathcal{O}(10^5)$ particles [11, 17, 33, 39], we can describe the entirety of condensed particles in such a system by a single wavefunction. Denote the single-particle ground state, i.e. the state with minimal energy, as $\phi(\mathbf{r})$. Since all particles in the condensed state assume this single-particle state, we have

$$\Psi(\mathbf{r}_1, \cdots, \mathbf{r}_{N_0}) = \prod_{i=1}^{N_0} \phi(\mathbf{r}_i) \tag{2.10}$$

for the wavefunction Ψ describing the many-body system [7, 35]. This gives rise to quantum properties on a macroscopic level.

2.2 Equation of motion - the eGPE

After these general observations, we will now proceed to describe Bose-Einstein condensation in dilute atomic gases with magnetic dipole interaction. The time evolution of a magnetic dipolar condensate with mean field wavefunction Ψ in an external trapping

potential $V(\mathbf{r})$ is described by the eGPE [17, 18, 21, 41, 44]

$$\begin{aligned} i\hbar\frac{\partial\Psi(\mathbf{r},t)}{\partial t} =& \Big\{-\frac{\hbar^2}{2m}\nabla^2 + V(\mathbf{r}) + g_s\left|\Psi(\mathbf{r},t)\right|^2 + \gamma_{QF}\left|\Psi(\mathbf{r},t)\right|^3 \\ &+ \int \mathrm{d}^3\mathbf{r}'\, U_{dd}(\mathbf{r}-\mathbf{r}')\left|\Psi(\mathbf{r}',t)\right|^2\Big\}\Psi(\mathbf{r},t), \end{aligned} \tag{2.11}$$

for an atomic species with mass m. The strength of the contact interaction is quantified by g_s and is given by $g_s = 4\pi\hbar^2 a_s/m$, where a_s denotes the s-wave scattering length [7]. The corresponding scattering pseudo-potential reads[2]

$$U_s(\mathbf{r}-\mathbf{r}') = g_s\delta(\mathbf{r}-\mathbf{r}'), \tag{2.12}$$

and the delta distribution $\delta(\mathbf{r})$ signifies that this potential describes contact interaction. A 2D Bose gas, by definition, is strongly trapped along one direction, which we choose to be aligned with the z-axis. We also consider the condensate to be untrapped in the xy-plane and in a harmonic trap, so the external potential is given by $V(\mathbf{r}) = \frac{m}{2}\omega_z^2 z^2$. Contributions by beyond mean-field quantum fluctuations are captured by Lee-Huang-Yang corrections, $\gamma_{QF} = \frac{32}{3}g_s\sqrt{a_s^3/\pi}\,\mathcal{Q}_5(\epsilon_{dd})$ [21]. These stabilizing contributions were first described in [46] and arise from expanding mean field results in first order of powers of $(\rho a_s^3)^{1/2}$, for ρ being the particle number volume density. Here, $\mathcal{Q}_5(\epsilon)$ takes the form $\mathcal{Q}_5(\epsilon) = \mathrm{Re}\left\{\int_0^1 \mathrm{d}u\,[1+(3u^2-1)\,\epsilon]^{5/2}\right\}$ [18, 41], but we make use of the approximation $\mathcal{Q}_5(\epsilon) \approx 1 + \frac{3}{2}\epsilon^2$ [21, 22] instead and express $\epsilon_{dd} = a_{dd}/a_s$ in terms of the s-wave scattering length and the magnetic dipole length $a_{dd} = m\mu_0\mu_m^2/(12\pi\hbar^2)$ [21]. Finally, since we consider a dipolar gas, a dipole-dipole interaction (DDI) term is needed in the eGPE. It is expressed in terms of a DDI potential $U_{dd}(\mathbf{r}-\mathbf{r}') = \mu_o\mu_m^2\,(1-3\cos^2\theta)\,/(4\pi\,|\mathbf{r}-\mathbf{r}'|^3)$ [18, 21, 22, 41, 47]. The system analyzed in the present work is characterized by polarization of all atomic dipoles in z-direction, $\vec{\mu}_m \parallel \hat{z}$, and θ denotes the angle between this polarization and $\mathbf{r}-\mathbf{r}'$. Each atom carries the magnetic moment $\mu_m = |\vec{\mu}_m|$, and μ_0 denotes the vacuum permeability. The DDI is discussed in more detail in Sec. 2.3.

Notably, we allow for interactions between atoms and therefore deviate from the assumptions made in Sec. 2.1. The mean field treatment of the eGPE is only valid in the dilute limit. Furthermore, we also neglect thermal excitations of the condensate. This is justified in the $T \ll T_c$ limit [28].

The eGPE as stated in Eq. (2.11) describes dynamics along all three spatial dimensions, so it can be simplified by considering the 2D special case at hand. To this end, we make an ansatz of factorization, i.e. $\Psi(\mathbf{r})$ factorizes into a part $\psi(x,y)$ in the xy-plane and a

[2] This expression is only valid at $|\mathbf{r}-\mathbf{r}'| \neq 0$, and in distributional sense, the more rigorous $U_s(\mathbf{r}-\mathbf{r}') \propto \delta(\mathbf{r}-\mathbf{r}')\frac{\partial}{\partial|\mathbf{r}-\mathbf{r}'|}|\mathbf{r}-\mathbf{r}'|$ [45] holds as the differential operator $\frac{\partial}{\partial|\mathbf{r}-\mathbf{r}'|}|\mathbf{r}-\mathbf{r}'|$ is equal to unity except at the origin. However, the pseudo-potential is exact when applied as an operator to wavefunctions subject to $\Psi(\mathbf{r}-\mathbf{r}') \neq 0$ at the origin, and since we evaluate this potential only during numerical simulations where this condition is met, we shall neglect this subtlety.

fixed wavefunction $\varphi(z)$ in z-direction,

$$\Psi(\mathbf{r},t) = \psi(x,y,t)\varphi(z). \tag{2.13}$$

Along the trapping direction, the wavefunction is that of a harmonic oscillator in its ground state due to the harmonic trapping potential,

$$\varphi(z) = \frac{1}{\sqrt{l_z}\pi^{1/4}} \exp\left\{-\frac{1}{2}\frac{z^2}{l_z^2}\right\}, \tag{2.14}$$

where l_z corresponds to the $1/e$ width of the condensate to be determined using a variational approach. In Eq. (2.14), we make a choice of normalization,

$$\int \mathrm{d}z\, |\varphi(z)|^2 = 1, \tag{2.15}$$

by choosing an appropriate prefactor for the exponential term. Since we are considering a system of N atoms, it is convenient to normalize the wavefunction in the xy-plane to this number,

$$\int \mathrm{d}x\mathrm{d}y\, |\psi(x,y)|^2 = N, \tag{2.16}$$

such that the particle number area density is given by $n(x,y) = |\psi(x,y)|^2$. Using the factorization Eq. (2.13) and the normalization Eq. (2.15), we demonstrate in Sec. B that the eGPE in the quasi 2D approach of this thesis reads

$$\begin{aligned} i\hbar\frac{\partial\psi(x,y,t)}{\partial t} = \Bigg\{ & -\frac{\hbar^2}{2m}\left(\frac{\partial^2}{\partial x^2}+\frac{\partial^2}{\partial y^2}\right) + \mathcal{E}_z \\ & + \frac{g_s}{\sqrt{2\pi}l_z}|\psi(x,y,t)|^2 + \sqrt{\frac{2}{5}}\frac{\gamma_{QF}}{\pi^{3/4}l_z^{3/2}}|\psi(x,y,t)|^3 \\ & + \int \mathrm{d}^2\mathbf{r}'_\perp\, U_{dd}^{2D}(\mathbf{r}_\perp - \mathbf{r}'_\perp)\,|\psi(\mathbf{r}'_\perp,t)|^2\Bigg\}\psi(x,y,t), \end{aligned} \tag{2.17}$$

where $\mathcal{E}_z = m\omega_z^2 l_z^2/4 + \hbar^2/(4ml_z^2)$. Here, we introduce $\mathbf{r} = (\mathbf{r}_\perp, z)^\top$ in cylindrical coordinates and a 2D DDI potential where the z degrees of freedom have been integrated out. It has a representation in Fourier space given by

$$\tilde{U}_{dd}^{2D}(\tilde{\mathbf{k}}_\perp) = \mu_0\mu_m^2/(3\cdot\sqrt{2\pi}l_z)\left[2 - 3\sqrt{\pi}\left|\tilde{\mathbf{k}}_\perp\right|\mathrm{erfcx}\left(\tilde{\mathbf{k}}_\perp\right)\right] \tag{2.18a}$$

$$\left[\text{Erratum: } \tilde{U}_{dd}^{2D}(\mathbf{k}_\perp) = \mu_0\mu_m^2/(3\cdot\sqrt{2\pi}l_z)\left[2 - 3\sqrt{\pi}\left|\tilde{\mathbf{k}}_\perp\right|\mathrm{erfcx}\left(\tilde{\mathbf{k}}_\perp\right)\right]\right] \tag{2.18b}$$

in terms of dimensionless scaled momentum $\tilde{\mathbf{k}}_\perp = \mathbf{k}_\perp l_z/\sqrt{2}$ in the radial momentum space plane, i.e. $\mathbf{k} = (\mathbf{k}_\perp, k_z)^\top$, and $\mathrm{erfcx}(x) = e^{x^2}\,\mathrm{erfc}(x)$ denotes the exponentially scaled complementary error function, where $\mathrm{erfc}(x) = 1 - \mathrm{erf}(x)$ is the definition of the

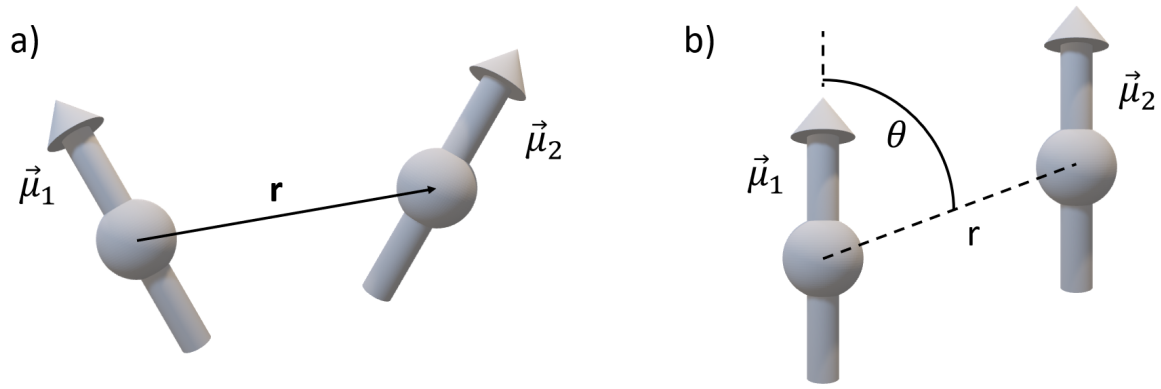

Figure 2.1: Schematic illustration of DDI in the absence (a)) and presence (b)) of polarization. If the dipoles are polarized, $\vec{\mu}_1 \parallel \vec{\mu}_2$, the DDI is fully described by the two scalar quantities θ and $r = |\mathbf{r}|$.

complementary error function, and $\mathrm{erf}(x) = 2/\sqrt{\pi} \int_0^x \mathrm{d}t\, e^{-t^2}$.

2.3 A closer look at DDI

In the previous section, we introduced the eGPE formalism to analyze BECs realized in a dilute atomic gas with natural magnetic dipoles. However, it is not straightforward why it might be insightful to focus on quantum systems with these distinct properties, especially compared to the purely contact interacting BEC.

Contact interaction, in particular the s-wave scattering we consider in this work, is isotropic since the corresponding scattering pseudo-potential Eq. (2.12) depends only on the modulus of the separation of two atoms. Additionally, contact interaction, by design, is short-ranged, which manifests itself in $U_s(\mathbf{r}) \propto \delta(\mathbf{r})$. The DDI, however, is fundamentally different. In general, the interaction of two magnetic dipoles $\vec{\mu}_1$ and $\vec{\mu}_2$ with arbitrary, i.e. unpolarized alignment is characterized by the potential [44, 48]

$$U_{dd}^{\text{unpolarized}}(\mathbf{r}) = \frac{\mu_0}{4\pi} \frac{(\vec{\mu}_1 \cdot \vec{\mu}_2)|\mathbf{r}|^2 - 3\,(\vec{\mu}_1 \cdot \mathbf{r})(\vec{\mu}_2 \cdot \mathbf{r})}{|\mathbf{r}|^5}, \tag{2.19}$$

with $\mathbf{r}$ the vector joining the two dipoles. Since we consider polarization of magnetic dipoles along the trapping direction in our setup, $\vec{\mu} \parallel \hat{z}$, and since the modulus of the magnetic moment is an universal atomic property, we have $\vec{\mu}_1 = \vec{\mu}_2 \equiv \vec{\mu}$ such that the general DDI potential reduces to

$$U_{dd}^{\text{polarized}}(\mathbf{r}) = \frac{\mu_0 |\vec{\mu}|^2}{4\pi} \frac{|\mathbf{r}|^2 - 3\,|\mathbf{r}|^2 \left(\frac{\vec{\mu}}{|\vec{\mu}|} \cdot \frac{\mathbf{r}}{|\mathbf{r}|}\right)^2}{|\mathbf{r}|^5} \equiv \frac{\mu_0 |\vec{\mu}|^2}{4\pi} \frac{1 - 3\cos^2\theta}{|\mathbf{r}|^3} \tag{2.20}$$

in the presence of polarization, as claimed in Sec. 2.2, with $\theta = \sphericalangle(\vec{\mu}, \mathbf{r})$ being the angle enclosed by the polarization direction and the separation vector by construction. Fig. 2.1

illustrates the interaction of dipoles with and without polarization.
The difference to the contact interaction is apparent. Not only is the DDI anisotropic, it is also long-ranged as the pseudo-potential does not vanish at finite dipole separations. With the suggestive notation in Eq. (2.20), we obtain $U_{dd}^{\text{polarized}}(\mathbf{r}) \propto 1/|\mathbf{r}|^3$. It is this long-ranged interaction that is absent in contact interacting gases and ultimately leads to supersolid properties in combination with the other interactions.
Another feature of DDI that is completely absent in case of contact interaction is the fact that DDI is neither strictly attractive nor repulsive. While the sign of g_s dictates, by isotropy, whether or not the contact interaction is attractive or repulsive, the sign of the DDI potential varies with θ. In the polarized case, we distinguish the three different cases

$$\begin{cases} U_{dd}^{\text{polarized}} > 0 & \text{if} \quad [\theta]_\pi \in (\theta_c, \pi - \theta_c) \\ U_{dd}^{\text{polarized}} = 0 & \text{if} \quad [\theta]_\pi = \arccos\left(1/\sqrt{3}\right) \equiv \theta_c \approx 0.955 \\ U_{dd}^{\text{polarized}} < 0 & \text{if} \quad [\theta]_\pi \in [0, \theta_c) \cup (\pi - \theta_c, \pi) \end{cases} \tag{2.21}$$

with $[\theta]_\pi$ the representative of the equivalence class of θ modulo π in the interval $[0, \pi)$ such that the DDI is both attractive and repulsive, depending on θ.
Finally, contact interaction preserves symmetries that are broken in the presence of DDI. The contact interaction potential is invariant under $SO(3)$ rotations since it only depends on the modulus of $\mathbf{r}$. Under $SO(3)$ rotations, the scattering potential behaves as

$$U_s(\mathbf{r}) = g_s\delta(\mathbf{r}) \overset{R\in SO(3)}{\longrightarrow} U_s(\mathbf{r}') = g_s\delta(R\mathbf{r}) = g_s\frac{1}{|\det R|}\delta(\mathbf{r}) = g_s\delta(\mathbf{r}) = U_s(\mathbf{r}), \tag{2.22}$$

in distributional sense. By Noether's theorem, this implies conservation of angular momentum. The anisotropy of the DDI potential breaks this invariance. From a scattering perspective, this leads to unconserved angular momentum in the collision of two atoms in the condensate.
BEC in a strongly interacting dipolar gas was first achieved a decade after the pioneering realizations of BEC in weakly interacting dilute gases in chromium-52 (^{52}Cr) [49]. Chromium provides a unique electronic structure, which leads to a large magnetic moment $\mu_m = 6\mu_B$. In the $^7S_3$ ground state, the electronic configuration $[\text{Ar}]3d^54s^1$ yields six electrons with aligned spins in the valence shell. Bosonic chromium isotopes have vanishing nuclear spin $I = 0$, resulting in the total electronic spin quantum number of 3 and the large magnetic moment. Achieving BEC in ^{52}Cr required the development of novel cooling techniques as losses from two-body collisions with spin relaxation prevent the condensate from reaching degeneracy with the previous cooling techniques as spin relaxation either leads to loss of atoms from the trap or heating of the condensate [50]. To overcome these losses, atoms are transferred to the lowest energetic spin state $m_J = -3$ where energy conservation prevents spin relaxation-induced transitions.
Rare earth metals, specifically magnetic lanthanides, provide another excellent experimen-

tal platform for the realization of highly interacting magnetic BECs. The first lanthanide to be Bose-Einstein condensed was ytterbium-174 in 2003 [51]. However, the ground state electronic configuration $[\mathrm{Xe}]4f^{14}6s^2$ does not yield a magnetic moment, so ytterbium is not interesting in the context of dipolar BECs. Magnetic lanthanides that have been Bose-Einstein condensed include dysprosium (Dy) in 2011 [52], erbium (Er) in 2012 [53], thulium in 2020 [54] and europium in 2022 [55]. Out of these four magnetic lanthanide species, Dy and Er are of particular interest, since their electronic ground state configurations $[\mathrm{Xe}]4f^{10}6s^2\,(^5I_8)$ and $[\mathrm{Xe}]4f^{12}6s^2\,(^3H_6)$ with four and two unpaired electrons in the partially filled $4f$-orbital shell lead to large orbital angular momentum numbers $L = 6$ and $L = 5$. Those couple in the LS-scheme with the spin quantum numbers $S = 2$ and $S = 1$ to large total angular momentum quantum numbers $J = 8$ and $J = 6$ as bosonic dysprosium and erbium are subject to $I = 0$. This results in large magnetic moments, $\mu_m = 10\mu_B$ and $\mu_m = 7\mu_B$, respectively, and makes Dy the lanthanide with the largest natural magnetic moment. Additionally, both Dy and Er possess multiple stable bosonic isotopes, which opens the possibility to study highly magnetic dipolar BECs with great variability in interaction properties such as scattering length and dipole length. They are in general isotope dependent. As of the writing of this thesis, successful BEC has been achieved in Dy isotopes ^{160}Dy, ^{162}Dy and ^{164}Dy [52, 56–60], and in Er isotopes ^{166}Er and ^{168}Er [53, 61], among others, as well as in numerous two-component BECs including both Dy and Er isotopes [62].

As a note, we add that alkali metals, which have been of great interest in the creation of BEC, also feature dipolar properties, as their electronic configuration reads $[\cdot]\mathrm{n}s^1$, where $[\cdot]$ denotes the appropriate noble gas core and n = 2, 3, 4, 5, 6, 7. This leads to a single unpaired electron in the valence shell, which yields a permanent magnetic moment. Apart from the pioneering realization of BEC in sodium, rubidium and lithium in 1995 [11–14] condensation has also been achieved in cesium in 2003 [63] and in potassium in 2007 [64]. Therefore, BEC has been achieved in all stable alkali metals. However, the single unpaired electron yields magnetic moments of at most $1\mu_B$ [17]. Therefore, DDI is negligible against contact interaction in alkali metals, i.e. $\epsilon_{dd} = a_{dd}/a_s \ll 1$ is a small parameter, e.g. in rubidium, we have $\epsilon_{dd} = 0.007$ [48]. Since $a_{dd} \propto \mu_m^2$, ϵ_{dd} is much larger in magnetic lanthanides, e.g. in Dy, we have $\epsilon_{dd} \sim 1$. It is ϵ_{dd} that governs whether or not a dipolar condensate is considered strongly interacting. Since DDI is not negligible against contact interaction in magnetic lanthanides, $\epsilon_{dd} \sim 1$, they are considered truly dipolar quantum gases.

2.4 Phases in a 2D supersolid

Recent publications [21, 22, 40, 41, 58–60] reveal a rich spectrum of crystalline order in 2D magnetic dipolar Bose gases in their ground state, enabled by the interplay of short-ranged contact interaction, quantum fluctuations and long-ranged DDI. These su-

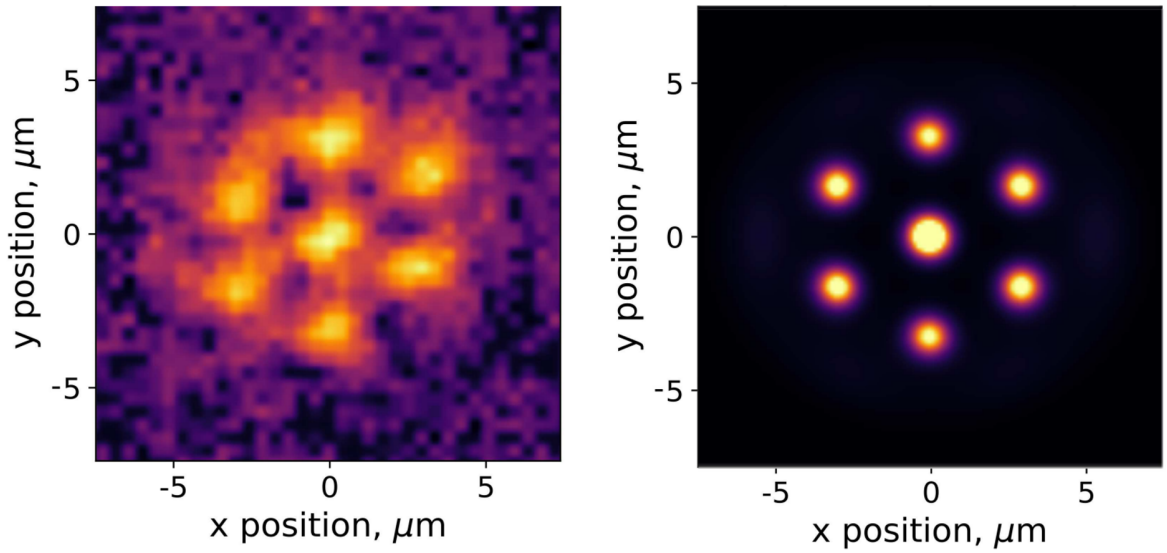

Figure 2.2: Experimental realization of a seven droplet hexagon state in ^{164}Dy in a harmonic trap. The left panel shows an *in-situ* measurement of the density profile, while the right panel displays a simulation of the same trap. Reproduced from [60] under CC BY 4.0.

persolid states exhibit properties of superfluidity as well as long-ranged crystal-like order. A stationary solution to the eGPE with periodic modulation beyond a uniform state that minimizes energy per particle for a given average particle area density $\bar{n}$ is referred to as the ground state. We employ a unit cell treatment to find the ground state for a given set of parameters $\{\bar{n}, a_s\}$, following closely the method described in [22]. This is possible as we evaluate the kinetic operator and the DDI potential in momentum space. The unit cell can interfere with fake Fourier copies of itself, accounting for the long-ranged nature of the DDI. Periodic boundary conditions are implemented as a consequence.

There are several distinct supersolid phases. Most notably, we will consider the droplet and honeycomb phases. In the droplet phase, the condensate clumps into droplets, arranging themselves into a hexagonal lattice. If the condensate is in the honeycomb phase, it arranges itself in a honeycomb-like lattice. These two phases are dual, since the density minima in a honeycomb lattice form a hexagonal lattice. However, a condensate in the honeycomb phase is much more connected, and particles can flow along the honeycomb lattice. Droplets are characterized by a very low particle density between droplets, therefore inhibiting particle flow. In Fig. 2.2, we report an experimental realization of a supersolid in the droplet phase. Numerically obtained ground state density distributions in both the droplet phase and the honeycomb phase may be found in Fig. 3.1.

Apart from these two phases with hexagonal discrete rotational symmetry, there exists a third phase known as the stripe phase. Here, the condensate forms isolated stripes with high particle density separated by parallel stripes with low particle density. The stripe phase is distinct from the droplet and honeycomb phases. While the lattice structure in the latter phases experiences discrete rotational symmetry by $\pi/3$, the lattice of the

stripe phase is only invariant under rotations of π. Additionally, a condensate in the stripe phase is invariant under continuous translations parallel to the stripes and under discrete translations orthogonal to the stripes. Both the droplet and the honeycomb phase only have invariance under discrete translations along the unit cell vectors. Numerically, it is harder to extract lattice order in the stripe phase compared to the other two phases, so we do not consider the stripe phase in the present work.
A common occurrence in all phases is that they lie below the uniform state in terms of a_s, i.e. regardless of $\bar{n}$, the condensate will assume a uniform ground state for high s-wave scattering lengths $a_s \gtrsim a_{dd}$. Reducing a_s will introduce supersolid properties, and smaller s-wave scattering lengths will in general experience less superfluidity. A comprehensive analysis of the superfluid-supersolid phase diagram can be found in [22], Fig. 2 and Fig. 3. In this thesis, we choose our system parameters, specifically the trap frequency ω_z and the atomic species ^{164}Dy similarly, so the phase diagram applies to our system.

2.5 Contrast in a supersolid

An important concept in supersolids is the density contrast [22, 41, 65]

$$C = \frac{|\psi|^2_{\max} - |\psi|^2_{\min}}{|\psi|^2_{\max} + |\psi|^2_{\min}}. \tag{2.23}$$

It serves as an order parameter quantifying crystalline order, and it is computed from the ground state wavefunction over a single unit cell. This is possible due to the periodicity of the ground state. A uniform state has $C = 0$ as the numerator of Eq. (2.23) vanishes in this limit. The other extreme is represented by a state with vanishing density at some points, $|\psi|^2_{\min} = 0$. Here, the contrast tends to $C = 1$. In general, $C > 0$ is indicative of crystalline order and therefore of supersolidity. We will use the contrast to compare datasets obtained with different parameters $\{\bar{n}, a_s\}$.

3 Numerical preliminaries

This section is concerned with numerical methods required to simulate the eGPE as outlined in the previous section and extract observables of interest. We introduce computational units and the split-step Fourier method, as well as explain how we compute the ground state for a given parameter combination $\{\bar{n}, a_s\}$. Additionally, we outline how to find vortices and lattice defects in numerical simulations. Finally, different initialization schemes and the quench method are discussed.

3.1 Computational units and split-step Fourier method

Since our ultimate goal is to put the eGPE on a lattice and simulate it numerically, it is worth introducing computational units. To this end, we consider a harmonic oscillator with oscillator length $l_0 = 1\,\mu$m. Not only does this oscillator define a length scale, it also provides an energy scale $\hbar\omega_0$ via $l_0 = \sqrt{\hbar/(m\omega_0)}$ and a time scale ω_0^{-1}. Although this method is universal and independent of the system, i.e. the choice for l_0 is completely arbitrary, it is motivated by the size of the simulated system. With this, it is possible to cast Eq. (2.17) into a dimensionless differential equation suitable for numerical calculations,

$$\begin{aligned} i\frac{\partial\psi(x,y,t)}{\partial t} = \Bigg\{ &-\frac{1}{2}\left(\frac{\partial^2}{\partial x^2}+\frac{\partial^2}{\partial y^2}\right) + \mathcal{E}_z^{eff} - \mu^{eff} \\ &+ g_s^{eff}\,|\psi(x,y,t)|^2 + \gamma_{QF}^{eff}\,|\psi(x,y,t)|^3 \\ &+ \int \mathrm{d}^2\mathbf{r}'_\perp\, U_{dd}^{2D,eff}(\mathbf{r}_\perp - \mathbf{r}'_\perp)\,|\psi(\mathbf{r}'_\perp,t)|^2 \Bigg\}\psi(x,y,t), \end{aligned} \tag{3.1}$$

as demonstrated in Sec. C.1. Here, we add in the chemical potential in units of $\hbar\omega_0$, $\mu^{eff} = \mu/\hbar\omega_0$[3]. We avoid evaluating expressions with small numerical constants such as $\hbar$ by introducing computational units, where $\mathcal{O}(\hbar) = 10^{-34}$ in SI units.

At this point, the eGPE could be solved numerically. Further considerations are necessary to obtain a feasible solving scheme. Note that computing the derivatives of the kinetic term is computationally expensive, so we resort to evaluate the kinetic term in momentum space where it is diagonal,

$$\begin{aligned} \left(\frac{\partial^2}{\partial x^2}+\frac{\partial^2}{\partial y^2}\right)\psi(x,y) &= \mathcal{F}^{-1}\left[\mathcal{F}\left[\left(\frac{\partial^2}{\partial x^2}+\frac{\partial^2}{\partial y^2}\right)\psi(x,y)\right]\right] \\ &= -\mathcal{F}^{-1}\left[\left(k_x^2+k_y^2\right)\tilde{\psi}(k_x,k_y)\right], \end{aligned} \tag{3.2}$$

and $\mathcal{F}$ the Fourier transform. This allows us to trade a second derivative in real space for a simple multiplication in Fourier space at the cost of having to perform Fourier transforms. However, computation of Fourier transforms (and their inverse) is fast on a discretized space-grid using the Fast-Fourier-Transform (FFT) algorithm [23].

Let us, for the moment, interpret Eq. (3.1) as an operator equation,

$$i\frac{\partial\psi(x,y,t)}{\partial t} = \hat{H}\psi(x,y,t), \tag{3.3}$$

where the Hamiltonian $\hat{H} = \hat{D} + \hat{L} + \hat{N} + \hat{V}_{dd}$ decomposes nicely into a kinetic operator $\hat{D}$, a linear operator $\hat{L}$ from the integration constants of the z integral and the chemical potential, a non-linear operator $\hat{N}$ from the contact interaction and quantum fluctuations,

[3]The eGPE is often written without the chemical potential. Since it represents a constant shift of energy, and since only changes in energy are relevant for the dynamic time evolution of the condensate, it may be neglected. However, when included in the eGPE, it sets the typical energy scale of the system.

as well as a dipole interaction operator $\hat{V}_{dd}$. The formal solution to this equation reads[4]

$$\psi(x, y, t + \Delta t) = e^{-i\hat{H}\Delta t}\psi(x, y, t). \tag{3.4}$$

We have already seen that the dipole interaction potential is best expressed in Fourier space as well[5]. Therefore,

$$\hat{V}_{dd} = \int \mathrm{d}^2\mathbf{r}_\perp \mathcal{F}^{-1}\left[\tilde{U}_{dd}^{2D,eff}(\mathbf{k}_\perp)\mathcal{F}\left[|\psi(\mathbf{r}_\perp)|^2\right]\right]. \tag{3.5}$$

If we further split the kinetic operator $\hat{D} = \hat{D}/2 + \hat{D}/2$, we can express Eq. (3.4) as [23, 24, 28]

$$\psi(x, y, t + \Delta t) = e^{-i\left(\frac{\hat{D}}{2} + \hat{L} + \hat{N} + \hat{V}_{dd} + \frac{\hat{D}}{2}\right)\Delta t}\psi(x, y, t). \tag{3.6}$$

Finally, we obtain

$$\begin{aligned}
\psi(x, y, t + \Delta t) = \; & \mathcal{F}^{-1}\left[e^{-i\frac{\hat{D}}{2}\Delta t}\mathcal{F}\left[e^{-i\left(\hat{L}+\hat{N}+\hat{V}_{dd}\right)\Delta t}\mathcal{F}^{-1}\left[e^{-i\frac{\hat{D}}{2}\Delta t}\mathcal{F}\left[\psi(x, y, t)\right]\right]\right]\right] \\
= \; & \mathcal{F}^{-1}\left[e^{-\frac{i}{2}\frac{1}{2}\mathbf{k}_\perp^2\Delta t}\mathcal{F}\left[e^{-i\left(\hat{N}+\hat{L}+\int \mathrm{d}^2\mathbf{r}_\perp \mathcal{F}^{-1}\left[\tilde{U}_{dd}^{2D,eff}(\mathbf{k}_\perp)\mathcal{F}\left[|\psi(\mathbf{r}_\perp)|^2\right]\right]\right)\Delta t}\right.\right. \\
& \left.\left. \times \; \mathcal{F}^{-1}\left[e^{-\frac{i}{2}\frac{1}{2}\mathbf{k}_\perp^2\Delta t}\mathcal{F}\left[\psi(x, y, t)\right]\right]\right]\right]
\end{aligned} \tag{3.7}$$

by exploiting that the kinetic operator is evaluated best in Fourier space. This is the well-established split-step Fourier method in full glory [23, 44]. This expression is exact in $\mathcal{O}(\Delta t^2)$ as we show in Sec. C.2. The $\mathcal{O}(\Delta t^3)$ error is computed on top.

3.2 Ground state calculations in Wick-rotated time

We have already seen that determining the ground state for a given set of parameters is important in our discussion of supersolid phases, see Sec. 2.4. To find it numerically, we make use of the definition that it is a stationary state, i.e. $\partial\psi/\partial t = 0$. Now, after

[4] Since the Hamiltonian in our case depends on $\psi(t)$ and therefore on t, we do not deal with a generic Schrödinger equation for a time-independent Hamiltonian. The resulting error of neglecting the time dependence of $\hat{H}$ does not increase the $\mathcal{O}(\Delta t^3)$ error from the non-commuting of the operators making up the Hamiltonian if we always use the latest $\psi(t)$ in the non-linear potential terms when numerically advancing by a time-step Δt [24, 28].

[5] Note that there are fast methods to evaluate $\mathrm{erfcx}(x) = e^{x^2}\,\mathrm{erfc}(x)$ that avoid underflow (from $\mathrm{erfc}(x) = 1 - \mathrm{erf}(x)$) and overflow problems (from e^{x^2}) when x is large, e.g. as outlined in [66].

dropping the explicit time dependence of ψ due to stationarity, we can write Eq. (3.1) as

$$\begin{aligned}\mu^{eff}\psi(x,y) = \Bigg\{ -\frac{1}{2}\left(\frac{\partial^2}{\partial x^2} + \frac{\partial^2}{\partial y^2}\right) + \mathcal{E}_z^{eff} + g_s^{eff}|\psi(x,y)|^2 + \gamma_{QF}^{eff}|\psi(x,y)|^3 \\ + \int \mathrm{d}^2\mathbf{r}'_\perp U_{dd}^{2D,eff}(\mathbf{r}_\perp - \mathbf{r}'_\perp)|\psi(\mathbf{r}'_\perp)|^2 \Bigg\}\psi(x,y),\end{aligned} \tag{3.8}$$

which is an eigenvalue problem in operator formalism,

$$\mu^{eff}\psi = \mathcal{L}_{eGPE}^{eff}[\psi]\psi, \tag{3.9}$$

for the effective eGPE operator in computational units

$$\begin{aligned}\mathcal{L}_{eGPE}^{eff}[\psi] = \Bigg\{ -\frac{1}{2}\left(\frac{\partial^2}{\partial x^2} + \frac{\partial^2}{\partial y^2}\right) + \mathcal{E}_z^{eff} + g_s^{eff}|\psi(x,y)|^2 + \gamma_{QF}^{eff}|\psi(x,y)|^3 \\ + \int \mathrm{d}^2\mathbf{r}'_\perp U_{dd}^{2D,eff}(\mathbf{r}_\perp - \mathbf{r}'_\perp)|\psi(\mathbf{r}'_\perp)|^2 \Bigg\}.\end{aligned} \tag{3.10}$$

The ground state as well as all stationary metastable states at higher energies will, by definition, fulfill

$$|\mathcal{L}_{eGPE}^{eff}[\psi]\psi - \mu^{eff}\psi| = 0, \tag{3.11}$$

so we have to verify that a solution to Eq. (3.9) actually minimizes energy. Numerically, we start by minimizing the residuals $r[\psi]$ of Eq. (3.11),

$$r[\psi] = \frac{\int \mathrm{d}^2\mathbf{r}_\perp |\mathcal{L}_{eGPE}^{eff}[\psi]\psi - \mu^{eff}\psi|}{\int \mathrm{d}^2\mathbf{r}_\perp |\mu^{eff}\psi|}, \tag{3.12}$$

and compute the effective chemical potential by means of integrating Eq. (3.9) after multiplying with ψ^* and using the normalization Eq. (2.16),

$$\mu^{eff} = \frac{1}{N}\int \mathrm{d}^2\mathbf{r}_\perp\, \psi^*(\mathbf{r}_\perp)\, \mathcal{L}_{eGPE}^{eff}[\psi]\, \psi(\mathbf{r}_\perp). \tag{3.13}$$

Throughout our quest to find the ground state, we employ the standard method of imaginary time evolution [24]. Considering a system ϕ described by a generic Hamiltonian $\hat{H}$, we can express the time evolution

$$\phi(\mathbf{r}, t+\Delta t) = e^{-i\hat{H}\Delta t}\sum_k c_k(t)\phi_k(\mathbf{r}) = \sum_k c_k(t)e^{-i(E_k-\mu)\Delta t}\phi_k(\mathbf{r}) \tag{3.14}$$

in terms of the eigenfunctions ϕ_k of $\hat{H}$ and time dependent coefficients $c_k(t)$ if we drop factors of $\hbar$. Note that we assume time independence of $\hat{H}$, which for the eGPE is not realized in general, but holds within $\mathcal{O}(\Delta t^2)$ as discussed above. Given that $\hat{H}$ is hermitian, we have real eigenvalues E_k and span the entire Hilbert space accessible to ϕ with ϕ_k. If we exploit that the eigenvalues are in fact the eigenenergies that satisfy

$\hat{H}\phi_k = (E_k - \mu)\phi_k$ and $0 \leq E_k - \mu < E_{k+1} - \mu$, we can Wick rotate our time axis $t \to \tau = -it$ [43] to obtain[6]

$$\phi(\mathbf{r}, \tau + \Delta\tau) = \sum_k c_k(\tau) e^{-(E_k - \mu)\Delta\tau} \phi_k(\mathbf{r}). \tag{3.15}$$

Therefore, modes with higher k will decay quickly, and, with a slight abuse of notation, we can write

$$\lim_{\tau \to \infty} \phi(\tau) = \phi_\mu, \tag{3.16}$$

where the limit is understood to include a renormalization of the wavefunction amplitude after each computational timestep since otherwise $\phi \to 0$. It is also applied in the sense $r[\phi] < \epsilon$ for the residuals of Eq. (3.12) and some numerical cutoff ϵ. In essence, we compute the lowest energy state, i.e. the ground state by solving the stationary eGPE in Wick-rotated time. As we include the chemical potential in the eGPE, the ground state corresponds to the eigenstate with eigenenergy μ, hence the notation $\phi_\mu = \phi_0$. Every initial wavefunction will eventually decay to the ground state, so we can start with a wavefunction sampled from a uniform distribution in the interval $(0, 1)$ normalized to match a given average density $\bar{n}$.

Again following closely the approach outlined in [22], we compute the ground state on a rhombic unit cell defined by the lattice vectors $\mathbf{a_1}$ and $\mathbf{a_2}$, with $|\mathbf{a_1}| = |\mathbf{a_2}| = l_x$, and, matching the anticipated discrete, hexagonal rotational symmetry in both the droplet and honeycomb phase, we choose the angle enclosed by $\mathbf{a_1}$ and $\mathbf{a_2}$ to be $\pi/3$. Since we evaluate the long-ranged DDI operator and the kinetic operator in Fourier space, the unit cell will interfere with fake Fourier-copies of itself during ground state simulations. This results in periodic boundary conditions, but as the system is untrapped in the xy-plane, the ensuing interference does not corrupt the results. Once we have found a ground state wavefunction with above method for a unit cell, we still have to enforce actual minimization of energy [21],

$$\begin{aligned} E[\Psi(\mathbf{r}) = \psi(\mathbf{r}_\perp)\phi(z)] = \int \mathrm{d}^3\mathbf{r}\, \Psi^*(\mathbf{r}) \Bigg[&- \frac{\hbar^2}{2m}\nabla^2 + \frac{1}{2}m\omega_z^2 z^2 + \frac{2}{5}\gamma_{QF}|\Psi(\mathbf{r})|^3 \\ &+ \frac{1}{2}\int \mathrm{d}^3\mathbf{r}' U(\mathbf{r} - \mathbf{r}')|\Psi(\mathbf{r}')|^2 \Bigg] \Psi(\mathbf{r}), \end{aligned} \tag{3.17}$$

for the combined potential

$$U(\mathbf{r} - \mathbf{r}') = U_s(\mathbf{r} - \mathbf{r}') + U_{dd}(\mathbf{r} - \mathbf{r}'), \tag{3.18}$$

to distinguish metastable excited states from the true ground state with minimum energy. To this end, we extract the energy per particle for different ground state wavefunctions

[6] Dropping factors of $\hbar$, Wick-rotating the time axis yields $i\frac{\partial}{\partial t}\phi(t) = \hat{H}\phi(t) \to i\frac{\partial \tau}{\partial t}\frac{\partial}{\partial \tau}\phi(\tau) = -\frac{\partial}{\partial \tau}\phi(\tau) = \hat{H}\phi(\tau)$, effectively removing the i from the Schrödinger equation.

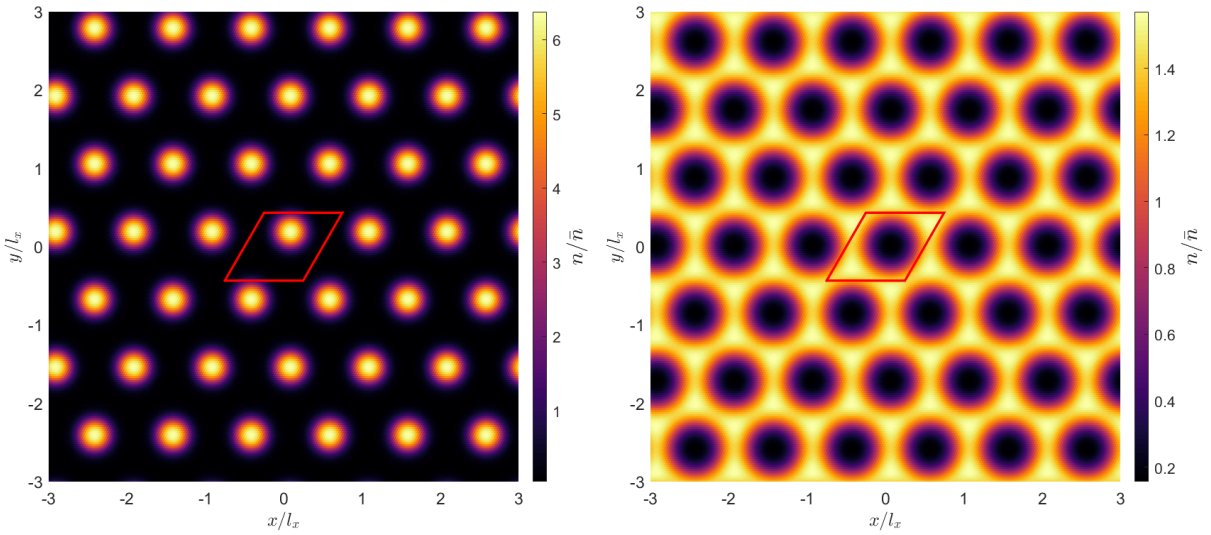

Figure 3.1: Numerically obtained condensate density distributions in the ground state for the droplet phase, $\bar{n} \cdot a_{dd}^2 = 0.075$, $a_s/a_{dd} = 0.745$ (left panel) and honeycomb phase, $\bar{n} \cdot a_{dd}^2 = 0.2$, $a_s/a_{dd} = 0.78$ (right panel). A rhombic unit cell is highlighted in red.

computed for a range of trial values of l_x and l_z within predefined windows, i.e. we allow different unit cell sizes (l_x) and harmonic oscillator length (l_z) for the wavefunction in trapping direction. We use an iterative approach to find l_x, where we progressively shrink the window size based on previous computations of energy per particle. For each trial value l_x, energy per particle is minimized with respect to l_z. Once we find the set $\{l_x, l_z\}$ with minimal energy per particle, these ground state parameters are fixed for a specific parameter combination $\{\bar{n}, a_s\}$. In general, the ground state depends on $\{\bar{n}, a_s\}$. This forces us to recompute the ground state for every single parameter combination.
Fig. 3.1 shows two numerically obtained ground state density distributions in both the droplet and honeycomb phase. Note the similarity to Fig. 2.2. As outlined above, we compute the ground state only on a rhombic unit cell, which is highlighted in red in Fig. 3.1. Subsequent periodic tiling of 2D space yields the ground states over a larger domain. The duality between the droplet and the honeycomb phase discussed in Sec. 2.4 is clearly visible, i.e both the density maxima in the droplet phase as well as the density minima in the honeycomb phase form a hexagonal lattice with discrete rotational invariance under rotations of $\pi/3$ and discrete translational invariance under translations along the unit cell lattice vectors.

3.3 Vortices in a superfluid

Superfluids are subject to a set of hydrodynamic equations describing their behavior. In particular, the velocity field may be written as $\mathbf{v} = \frac{\hbar}{m}\nabla\phi$, for some scalar phase ϕ [7, 28,

34, 35]. As a consequence, a quantized phase-winding $\delta\phi$ exists for any closed contour γ,

$$\delta\phi = \oint_\gamma \nabla\phi \cdot \mathrm{d}\mathbf{s} = 2\pi\, l, \tag{3.19}$$

for some integer l, since the condensate wavefunction must assume the same phase after integer loops of a closed contour. However, any regular function h over a simply connected domain $\mathcal{D}$ fulfills

$$\oint_\gamma \nabla h \cdot \mathrm{d}\mathbf{s} = 0 \tag{3.20}$$

for all closed contours $\gamma \in \mathcal{D}$. Hence, a superfluid is irrotational except for phase winding around singular points called vortices, i.e. the circulation along any closed contour vanishes if the contour does not enclose a vortex.

For the quasi 2D special case at hand, we have invariance of the trapping potential under azimuthal rotations. Phase winding will also occur solely within the radial plane as the separated wavefunction Eq. (2.13) only allows for dynamics in the xy-plane.

It is possible to assign topological charge to each vortex, where the absolute value is given by $|l|$, i.e. the multiplicity of full 2π phase windings. To distinguish clockwise from counter-clockwise rotation, we introduce a relative sign between these two possibilities. The absolute sign is arbitrary and a matter of convention. It is highly unlikely to find vortices with $|l| \neq 1$ under conditions as in the present work. We shall henceforth treat all vortices to have unit charge.

Vortices can be identified with a tiling algorithm. Consider all possible 2×2 tiles of the wavefunction, and for each tile, compute the phase-winding. If it exceeds $2\pi - \epsilon$, for some numerical tolerance ϵ, a vortex is said to be at the center of the tile. Refer to Sec. C.3 for a MATLAB implementation of this algorithm.

3.4 Lattice defects in droplet the phase

Quenching into the droplet phase does not result in a perfect crystal lattice. Different domains of the condensate show different crystal orientations, as depicted in Fig. 3.2. Inevitably, this leads to defects in the crystal lattice. The relaxation of these defects will be analyzed in the next section. We identify the positions of droplets in the xy-plane at first to extract the lattice structure from numerical data. These correspond to local density maxima. However, the condensate will also have fluctuations on sub droplet-size scales, so we have to impose several criteria to accurately capture droplet positions. In general, the set of droplets will form a subset of the local density maxima. Fluctuations on small length scales correspond to high momentum modes in the Fourier transform of the condensate's density. We can remove these local density maxima by convolving a Gaussian kernel with the Fourier transform of the density, exponentially suppressing fluctuations on sub droplet-size scales. Additionally, local density maxima are required

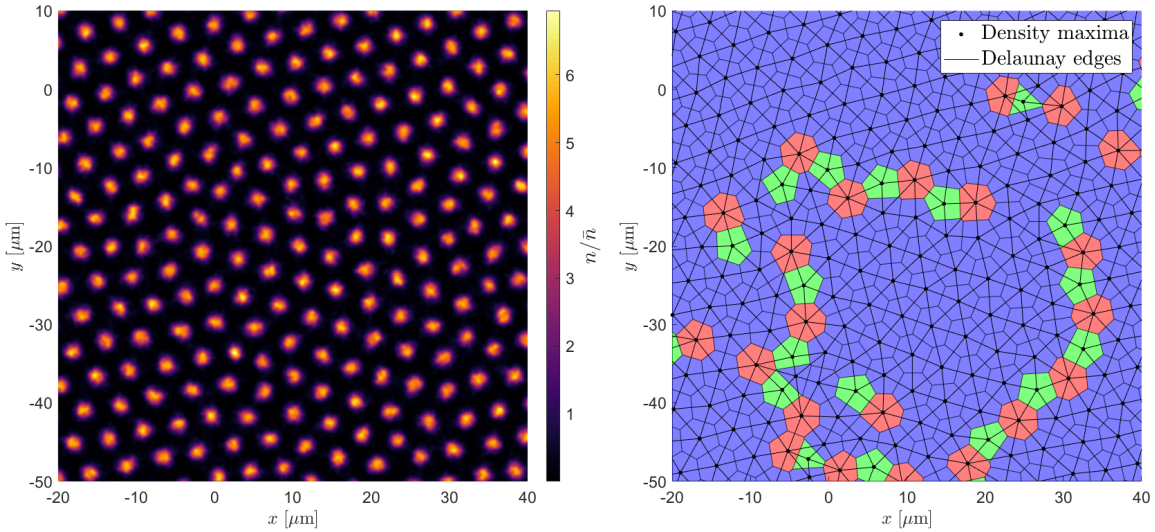

Figure 3.2: Lattice defects in the droplet phase 1500 ms post quench for $\bar{n} = 0.075 \cdot a_{dd}^{-2}$, $a_s/a_{dd} = 0.75$. The left Panel shows the particle area density in the xy-plane. Right Panel: Voronoi tesselation of the xy-plane. Blue Voronoi cells signify neutral density maxima, whereas green cells distinguish negatively charged density maxima from positively charged density maxima in red cells. The Delaunay triangulation and the extracted positions of the density maxima are plotted atop the Voronoi tesselation in black. Both panels show the same 60×60 μm^2 patch of condensate.

to exceed a minimum density, and they must have a minimum separation from the next maximum. We extract droplet positions by matching the density maxima positions to the underlying space grid after retaining only those local density maxima that meet these filtering conditions. For an exact description of the used algorithm, see Sec. C.4. To get a lattice structure from droplet positions, we perform a Delaunay triangulation. This results in a graph whose adjacency matrix describes the lattice bonds. A Delaunay triangulation may be viewed as the dual graph to a Voronoi tessellation. In a Voronoi tesselation, we associate the Voronoi cell R_i to droplet i at position $\mathbf{r_i}$, where a Voronoi cell consists of all the points of the condensate support $\mathcal{D}$ that are closer to $\mathbf{r_i}$ than to any other droplet,

$$R_i = \{\mathbf{r} \in \mathcal{D} \,|\, d(\mathbf{r}, \mathbf{r_i}) \leq d(\mathbf{r}, \mathbf{r_j}) \,\forall j \neq i\}, \tag{3.21}$$

using the Euclidean metric $d(\mathbf{r_1}, \mathbf{r_2}) = \|\mathbf{r_1} - \mathbf{r_2}\|$ [67]. We assign topological charge to each droplet via $Q = (\#\text{bonds} - 6)$, where #bonds is the number of bonds associated with a given droplet. In a Voronoi tessellation with Euclidean metric, a droplet with #bonds outgoing bonds is associated with a Voronoi cell with #bonds edges, so we also have $Q = \#\text{edges} - 6$ for the edges of the Voronoi cells. This definition of topological charge is useful as droplets in a perfect hexagonal lattice will have exactly 6 outgoing bonds connecting to the neighboring droplets. Similar to the vortex charge, defects with $|Q| > 1$ are extremely sparse, so we will consider all defects to have unit charge and only distinguish the sign of the charge.

As discussed in Sec. 2.4, the honeycomb phase is dual to the droplet phase. Therefore, these methods can easily be modified to analyze quenches in the honeycomb phase by replacing maxima with minima and inverting constraints such as a minimum density to a maximum density.

3.5 System setup and quench method

The present work considers a rectangular system with aspect ratio $\sqrt{3}$ since this matches the ideal aspect ratio when tiling 2D space with regular hexagons. We will refer to the shorter dimension as x-direction, and we choose it to be 16 unit-cell lengths l_x in size. Each unit-cell length is assigned 32 grid points.
We consider a dilute gas of ^{164}Dy atoms due to their large natural dipole, $\mu_m = 9.93\,\mu_B$, with μ_B the Bohr magneton [17, 18, 41]. This results in a dipole length of $a_{dd} = 130.8\,a_0$ in terms of the Bohr radius a_0, making this specific atomic species interesting for research [17–19, 41, 52, 59, 60]. To obtain the pancake shape of the trapped cloud, we set $\omega_z = 2\pi \cdot 72.4$ Hz, in accordance with [22]. We explore supersolid formation in the droplet phase in the parameter region given in Tab. 3.1. For the honeycomb phase, we consider $\bar{n} \cdot a_{dd}^2 = \{0.17, 0.2, 0.22\}$ and $a_s/a_{dd} = 0.78$ with uniform initialization. To observe the formation of supersolids, we prepare a condensate in either of two different initial states. Firstly, we consider a uniform state normalized to a given average density,

$$\psi_{\text{initial}}^{\text{uniform}}(x, y) \propto \mathbb{1}(x, y), \tag{3.22}$$

where $\mathbb{1}(x, y)$ denotes assigning unity to each grid point. In this case, the wavefunction is purely real. In the droplet phase, we also analyze the time evolution of systems with different parameters $\{\bar{n}, a_s\}$ when seeded with droplets initially, arranged in a square lattice. As we analyze the formation of lattice structures, seeding the condensate with droplets immediately eradicates the need to form individual droplets initially, but by arranging the droplets without hexagonal symmetry in a square lattice, the time evolution towards the ground state still involves the formation of the characteristic hexagonal lattice. To achieve this biasing of the initial state towards the droplet phase, we start with a uniform wavefunction normalized to unity at each grid point. We add a single droplet per unit cell, where the radial density distribution of a droplet is assumed to be of Gaussian form. Additional noise is added by shifting the positions of the droplets around the centers

$\bar{n} \cdot a_{dd}^2$ \ a_s/a_{dd}	0.745	0.75	0.755	0.76	0.765	0.77	0.775	0.78
0.075	u, l	u, l	u, l	u, l	u, l	u, l	u, l	
0.085		u	u	u	u	u	u	u

Table 3.1: Parameter combinations and initialization schemes used in the droplet phase. We denote uniform initialization with u and square lattice initialization with l.

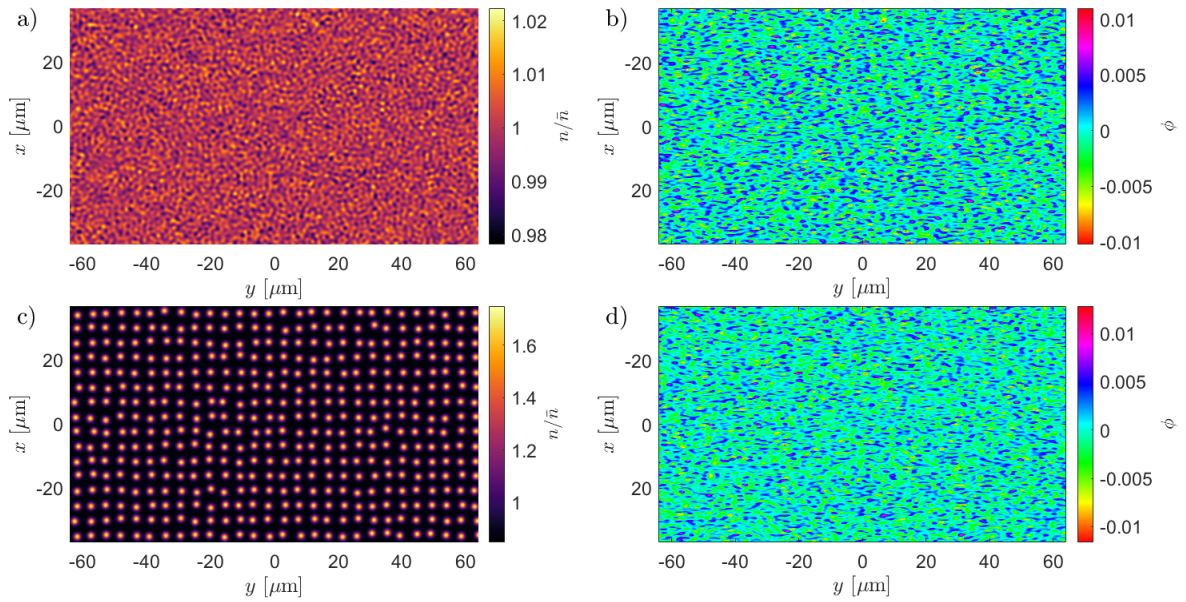

Figure 3.3: Single realizations of different initial states after adding noise in the Truncated-Wigner-approximation. Panels a) and b) show density fluctuations $n/\bar{n}$ and phase fluctuations $\phi(x, y) = arg(\psi(x, y))$ in the uniform initialization scheme, respectively. Panels c) and d) visualize the square lattice initial state.

of the unit cells. Denote the central coordinates of the unit cell i as cx_i and cy_i in x and y direction, respectively. Shifting the central coordinates is done by adding an offset δx_i and δy_i to these central coordinates. The offsets themselves are sampled from a standard normal distribution and scaled to match the length scale of the system. Then, the initial wavefunction reads

$$\psi^{\text{lattice}}_{\text{initial}}(x, y) \propto \left[\mathbb{1}(x, y) + \sum_i \exp\left\{-\frac{(x - cx_i - \delta x_i)^2 + (y - sy_i - \delta y_i)^2}{2\sigma^2}\right\}\right]^{1/2}, \tag{3.23}$$

where σ controls the width of a droplet. The sum $\sum_i$ runs over all unit cells, and the square root ensures that we seed the square lattice pattern into the density.
In the end, we normalize the wavefunction to a given average density such that

$$\bar{n} = \int \tilde{\mathrm{d}}x\tilde{\mathrm{d}}y\, |\psi^{\text{uniform}}_{\text{initial}}(x, y)|^2 = \int \tilde{\mathrm{d}}x\tilde{\mathrm{d}}y\, |\psi^{\text{lattice}}_{\text{initial}}(x, y)|^2, \tag{3.24}$$

for a normalized measure $\tilde{\mathrm{d}}x\tilde{\mathrm{d}}y = \mathrm{d}x\mathrm{d}y \cdot \left(\int \mathrm{d}x\mathrm{d}y\right)^{-1}$, in accordance with Eq. (2.16). We add noise to either of these initial states in the Truncated-Wigner-approximation before starting a simulation. Fig. 3.3 shows two realizations of these initial states. Note that while the phase fluctuations are of the same magnitude across both initialization schemes since they stem solely from the added Truncated-Wigner-noise, density fluctuations are dominated by droplets in the square lattice scheme.
In a uniform state, variations of the wavefunction are of order of the coherence length ξ,

which can be expressed in terms of a_s, $\xi^{-2} = 8\pi\bar{n}a_s$ [7]. This length scale can be used to define a typical energy scale of the uniform system. We use ξ to set an upper energy limit when adding noise to the initial state in the Truncated-Wigner-approximation [68]. At the beginning of a simulation, we set the s-wave scattering length such that the ground state is within the droplet or honeycomb phase, depending on the average density. This corresponds to an instantaneous quench of the s-wave scattering length. Afterwards, the system evolves according to the eGPE towards a supersolid state. For each parameter combination, we consider 3000 independent realizations, i.e. 3000 quenches with noise sampled as above. We let the condensate evolve up to a maximum time $t_{max} = 1.5 \cdot 10^3$ ms and numerically advance the eGPE in time steps of $\Delta t = 10^{-2}$ ms.

3.6 Periodic boundary conditions and distance measure on a finite grid

Solving the eGPE with the split-step Fourier method implements periodic boundary conditions. This has important consequences when computing the lattice structure with a Delaunay triangulation. On a finite space-grid, all droplets close to the grid boundary will be identified as lattice defects since the droplets existing beyond the boundary of the grid are absent in simulations. To correct for this error, we pad the simulated patch of condensate with itself. More precisely, we extend the simulated grid by about two unit cell lengths in each dimension before identifying density maxima (minima) in the droplet (honeycomb) phase and performing the Delaunay triangulation to obtain the lattice structure. This is done by computing the density $n(x, y) = |\psi(x, y)|^2$ over the original grid and subsequent padding of n with itself, where we choose the size of the padding to be 70 grid points. Since a unit cell is assigned 32 grid points, this corresponds to more than two unit cell lengths. Effectively, this enforces

$$n(x, y) = n(x + L_x, y) \tag{3.25}$$

and

$$n(x, y) = n(x, y + L_y). \tag{3.26}$$

L_x (L_y) denotes the size of the simulated system in x (y) direction, i.e. in our case $L_x = 16\, l_x$ ($L_y = \sqrt{3} \times 16 l_x$). Then we compute the lattice structure from this padded, i.e. spatially extended density and restrict the subsequent analysis to lattice points within the originally simulated domain. This approach ensures that we accurately account for the lattice structure at the boundaries of the simulated system.

Periodic boundary conditions also impact how to calculate distances in the simulated system. The distance measure has to be wrapped around the boundary of the space-grid. Consider two points in the system with coordinates $\mathbf{r_i} = (x_i,\, y_i)$, $i = 1, 2$. Then the naïve

Euclidean metric yields the distance

$$d = \sqrt{(x_1 - x_2)^2 + (y_1 - y_2)^2} \equiv \sqrt{(\Delta x)^2 + (\Delta y)^2} \tag{3.27}$$

between these points. If we are mindful of periodic boundary conditions, we have to replace

$$\Delta x \to \tilde{\Delta} x = \min(|\Delta x|, L_x - |\Delta x|) \tag{3.28}$$

and

$$\Delta y \to \tilde{\Delta} y = \min(|\Delta y|, L_y - |\Delta y|), \tag{3.29}$$

respectively. All distances reported in the subsequent analysis are understood in this periodic Euclidean metric.

3.7 Numerical simulation and evaluation environment

We outline our numerical procedures used to generate the results presented in this thesis to conclude our numerical discussions and demonstrate the key data generation, reduction, and analysis methods to the reader.

After setting the important parameters $\{\bar{n}, a_s\}$ and choosing an initialization scheme, a simulation run starts by computing the ground state within the unit cell treatment. Then, we simulate 3000 independent time evolutions after quenching the s-wave scattering length using the ground state parameters $\{l_x, l_y\}$ and the split-step Fourier method. We extract and store the vortex positions and vortex charge as well as the density maxima (minima) positions in the droplet (honeycomb) phase and the results of the Delaunay triangulation in millisecond intervals during the simulations. Extracting vortex and defect positions directly during the simulation greatly reduces the amount of generated data. Otherwise, we would have to store the condensate wavefunction at each evaluation time step and compute the observables of interest in a later step. A pair of vortex or defect coordinates consists of two floating point numbers, so even storing several hundred coordinates is more memory efficient than storing arrays the size of our system, i.e. 512×886 complex floating point numbers. All simulations are independent since they represent independent noise realizations. This allows us to compute the simulations in parallel on the CPU cluster Helix within the bwHPC environment, see also the Acknowledgments section.

In a next step, we abstract from the physical properties of the simulated condensate and compute all observables such as inter-defect distances or correlation functions necessary for our analysis in Sec. 4 and Sec. 5 for each quench individually. Again exploiting their independence, we developed highly parallelized algorithms that run on the CPU cluster on 64 CPUs in parallel. Executing this intermediate analysis for each simulation individually on the CPU cluster has two advantages.

Firstly, the cluster offers enough memory to execute the evaluation of the individual simulations in parallel, thus greatly reducing the computational time needed for this analysis

step.
Secondly, by splitting the simulation and the analysis step into two sets of programs, we obtain a highly flexible software architecture that can easily be modified to compute further observables from the fundamental vortex and defect properties, i.e. positions and charge.
For this thesis, we accumulated over 250 years of CPU time on the Helix cluster during the data generation and analysis process.
Finally, we have reduced the need for computational resources and memory to a level manageable with a standalone computer. In the last data reduction step, we collect the data from individual quenches and compute ensemble averages, probability distributions, and statistical fluctuations across all simulations with a given parameter combination $\{\bar{n}, a_s\}$. Now the data is in a form that allows us to compute fits and generate the figures we report in our analysis.
This data generation and reduction process is repeated for every parameter combination $\{\bar{n}, a_s\}$ and initialization scheme.
We have implemented all of the above in MATLAB. In the following, we give an overview of the software development necessary to obtain the results outlined in this thesis. We expanded the eGPE solver provided by W. Kirkby to include the square lattice initialization scheme and the vortex and lattice defect finding algorithms. The parallelized intermediate data analysis step consists of nine programs totaling about 450 lines of code. We wrote about 50 programs for the data aggregation, evaluation, and plotting step of the analysis, with well over 5000 lines of code.

4 Topological lattice defects and bond-order correlations

This section presents the analysis of the decay of lattice defects during supersolid formation, for both the droplet phase in Sec. 4.2 and the honeycomb phase in Sec. 4.6. We also analyze the increase in bond-order correlation in the droplet phase in Sec. 4.4 and in the honeycomb phase in Sec. 4.7.

4.1 Algebraic scaling regimes of the lattice defect coarsening

Fig. 4.1 shows the time evolution of the lattice defect number $N_D(t)$ obtained for the specific parameter combination $\bar{n} \cdot a_{dd}^2 = 0.075$, $a_s/a_{dd} = 0.76$. Further parameter combinations are discussed in more detail in Sec. D.1. Initially, the lattice defect number increases rapidly in time. This is due to the applied filtering criteria discussed in Sec. 3.4 as they prevent tracking of vortices with limited density contrast. Additionally, the displayed data stems from quenches within the uniform initialization scheme such that

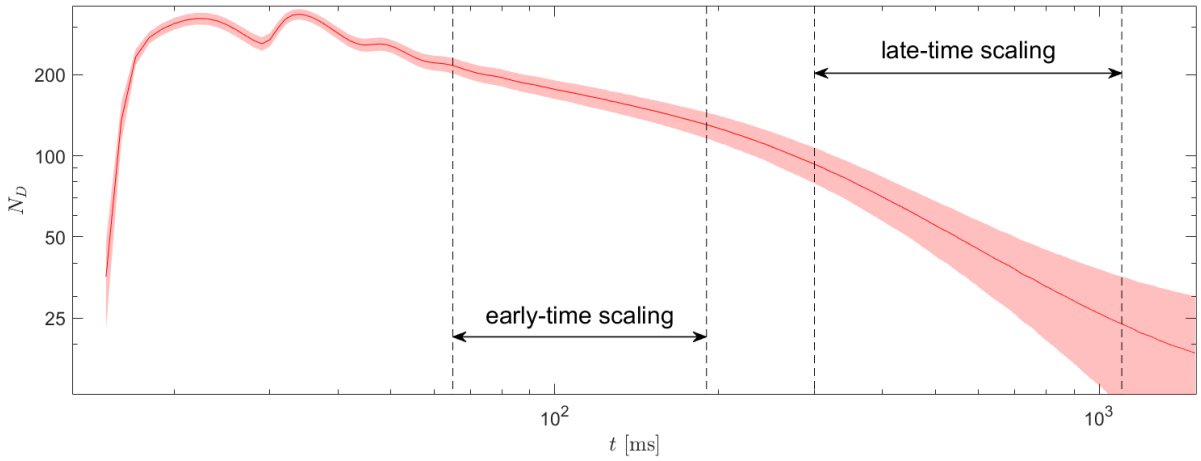

Figure 4.1: Time evolution of the lattice defect number $N_D(t)$ in the droplet phase for $\bar{n} \cdot a_{dd}^2 = 0.075$, $a_s/a_{dd} = 0.76$ and uniform initialization. Shading in red shows the statistical fluctuation of the defect number across 3000 quenches with independent noise realizations. Dashed lines in black indicate the approximate temporal boundaries of the two distinct algebraic scaling regimes.

the condensate has to form droplets and a lattice structure does not exist immediately post quench. The log-log plot clearly shows two different algebraic scaling regimes where the defect number exhibits algebraic scaling with different scaling exponents. A steeper slope and subsequently a faster lattice defect decay is observable in the late-time scaling regime. We focus the following analysis and discussion on this regime as the lattice defect number has larger numerical support in the late-time scaling regime owing to the fact that we extract the lattice defect number over a linearly spaced temporal grid. We observe that the late-time scaling regime does not extend to the latest simulated times, which can be linked to the formation of long-lived global grain boundaries, as discussed in Sec. 4.3.

4.2 Late-time scaling exponents of the lattice defect coarsening in the droplet phase

Our analysis begins by extracting the scaling exponents of the time evolution of the defect number $N_D(t)$ in the late-time scaling regime discussed in the previous section Sec. 4.1, using the ansatz

$$N_D(t) = A \cdot (t - t^*)^{\alpha}\,, \tag{4.1}$$

where A denotes a normalization constant and t^* a time shift included in the algebraic decay fit. Scaling with $(t - t^*)^{\alpha}$ is understood in the following sense: a system with arbitrary initial state at $t = 0$ will evolve until $t = t_1$ according to some non-algebraic prescaling. At this time the system reaches the same state as if it had evolved for some $t_2 \neq t_1$ according to the algebraic decay. At times $t > t_1$, scaling according to Eq. (4.1) applies, and $t^* = t_1 - t_2$. This gives rise to both positive and negative t^*.
To extract the algebraic decay constant α and t^* from data, we observe that $N_D(t)^{1/\beta}$

will form a linear function only for the right value of $\beta = \alpha$. t^* is then easily extracted as the intercept of $N_D(t)^{1/\beta}$ with the t-axis. This method is described in [69]. We detect defect numbers ranging from $\mathcal{O}(10^2)$ at the beginning of a quench to $\mathcal{O}(10^1)$ at the end of a quench due to our system size. Since t^* and α are independent of the overall normalization, it is numerically beneficial to reduce the normalization by an order of magnitude to get $\mathcal{O}(1)$ numbers. This improves numerical stability when computing $N_D(t)^{1/\beta}$ over a range of possible β, especially if β is negative and close to zero. That leads to

$$\left(\frac{N_D(t)}{10}\right)^{1/\beta} = \left(\frac{A}{10}\right)^{1/\beta} \cdot (t - t^*)^{\alpha/\beta}, \tag{4.2}$$

such that if we divide by the prefactor of the right hand side of Eq. (4.2), denote the corresponding left hand side as $\widetilde{N}(t)$, and for $\alpha = \beta$, we get a linear function with unit slope,

$$\widetilde{N}(t) = t - t^*. \tag{4.3}$$

The optimum β is found by computing the left hand side of Eq. (4.2) over a range of possible β and minimizing the squares of the residuals of a linear fit to the transformed defect number $\widetilde{N}$. The results are plotted in Fig. 4.2. In our fit, we exclude early time steps, where the supersolid is still forming and exhibiting algebraic scaling in the early-time scaling regime, and late time steps, where most of the defects have already decayed. Once we compute α and t^*, it is possible to compare them across datasets by considering them to be a function of the density contrast. For each parameter combination, the contrast is computed from the numerically obtained ground state wavefunction using Eq. (2.23).

4.2.1 Bootstrap fit with non-Gaussian errors

The errors of the transformed defect number $\widetilde{N}(t)$ shown in Fig. 4.2, panels a) through c), are obtained by taking the standard deviation across all 3000 quenches for every timestep. However, as we shall see in Sec. 4.3, the defect number does not scatter around its mean in a Gaussian fashion. Therefore, we cannot apply a naïve χ^2 minimization scheme. Instead, we resort to a method known as bootstrapping [70]. This technique does not require Gaussian errors since it resamples the original dataset with replacement and fits the best α for all generated bootstrap datasets. Each bootstrap sample yields an individual α and t^*. Contrary to the defect number, their distribution scatters uniformly around a mean, as we confirmed in Fig. D.2 in Sec. D.2. It is justified to estimate the error of α and t^* by taking the standard deviation across these distributions. This yields the errors reported in Fig. 4.2, panels d) and e).

Although the bootstrap method is a powerful method in theory, it comes with its own drawbacks when implemented on a real-world computer. Consider the data presented in Fig. 4.2. We report the time evolution of the defect number for 21 different parameter

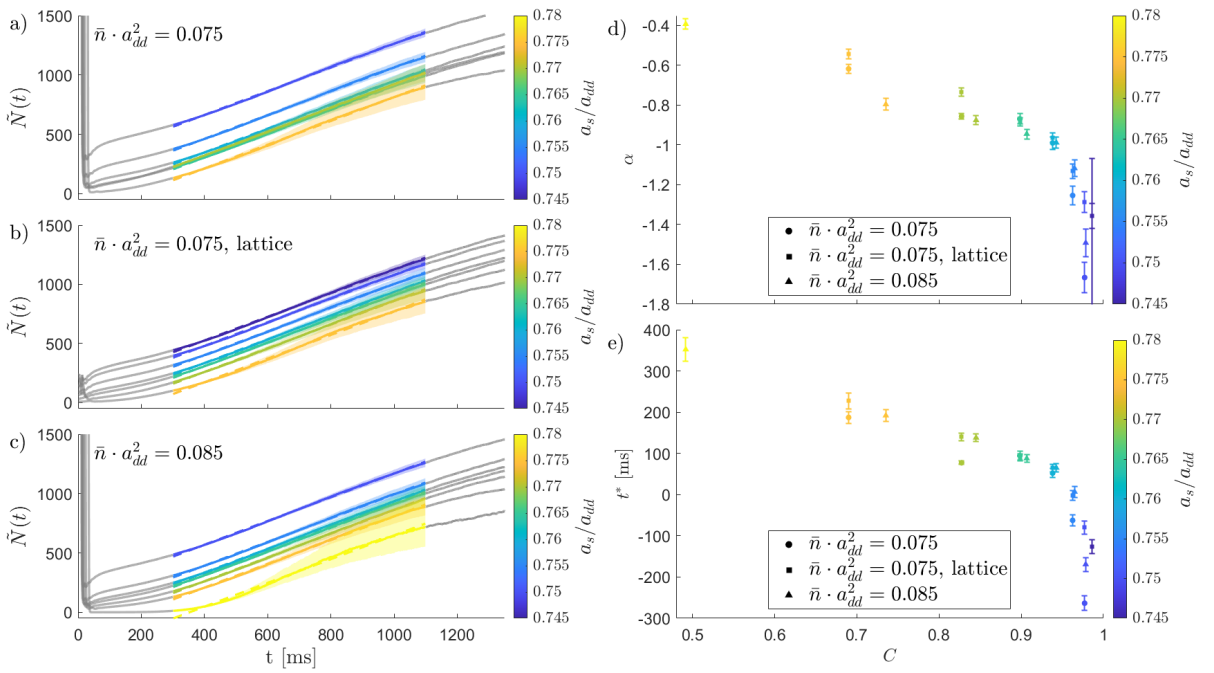

Figure 4.2: Lattice defect decay in the droplet phase for different initial states. Panel a) shows the defect coarsening for $\bar{n} \cdot a_{dd}^2 = 0.075$ and at different scattering length with uniform initial state. Panel b) holds data recorded with the same parameters as in a), but with a square lattice initial state. In c), we report defect coarsening at a higher average density $\bar{n} \cdot a_{dd}^2 = 0.085$. Color distinguishes different a_s, while data shown in gray corresponds to early and late times excluded from the fit. Dashed-lines represent the best linear fit obtained by the bootstrap method and shading indicates error regions for data considered in fitting. Note that the χ^2-fit for $\bar{n} \cdot a_{dd}^2 = 0.075$, $a_s/a_{dd} = 0.745$ has not converged, so we shall exclude this parameter combination from further analysis. Panel d) shows the extracted scaling exponents, and the corresponding t-axis intercepts are depicted in panel e) as a function of contrast C. For better readability, errors in d) and e) are scaled by factor of 5 and 20, respectively. Results are obtained for 500 bootstrap resamplings.

combinations $\{\bar{n}, a_s\}$ and initialization schemes. For every parameter combination, we generate 500 bootstrap resamplings. For each resampling, we fit a linear function in the minimum χ^2 scheme to the transformed defect number $\widetilde{N}(t)$ computed over a range of 200 β. In total, this amounts to 2.1 million linear fits. This situation quickly deteriorates and consumes more than reasonable amounts of computational resources unless some numerical methods are applied to save computational resources and make the bootstrap applicable. Firstly, fits to different bootstrap samples are independent, so we can run them in parallel efficiently without the need to feed back information across fits. Additionally, we do not explicitly compute χ^2 and minimize this quantity with a standard minimizer. Instead we make use of the fact that we fit a linear function of the form

$$\widetilde{N}(t) = \theta_1 \cdot t + \theta_0, \tag{4.4}$$

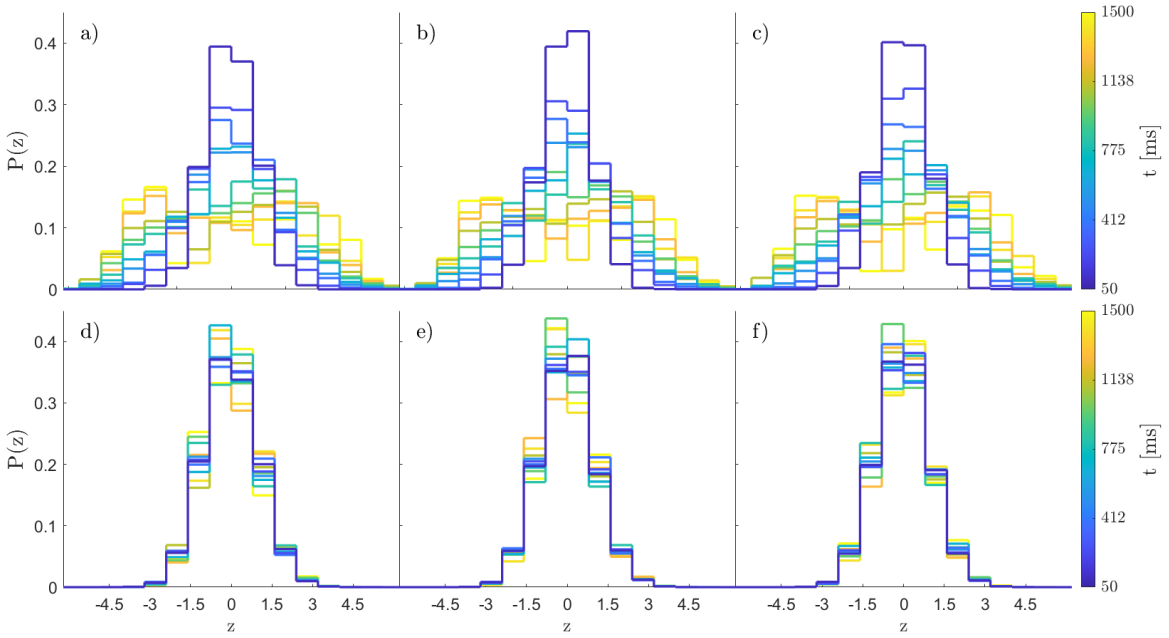

Figure 4.3: Time evolution of defect number distributions for $a_s/a_{dd} = 0.76$. Top panels a) through c) show the time evolution of the defect number distributions for $\bar{n}\cdot a_{dd}^2 = 0.075$ with uniform initialization, $\bar{n}\cdot a_{dd}^2 = 0.075$ with square lattice initialization and $\bar{n}\cdot a_{dd}^2 = 0.085$ with uniform initialization, respectively, when standardized according to Eq. (4.7). In the lower panels d) through f), we report Poissonian distributions standardized in the same fashion, and sampled 10^5 times with means according to the corresponding distribution from the panels above.

where the fit parameter θ_1 denotes the slope of Eq. (4.2). t^* is given by $-\theta_0/\theta_1$. If we introduce the weight matrix

$$W = \mathrm{diag}\left(\sigma^2_{\widetilde{N}(t_1)}, \cdots, \sigma^2_{\widetilde{N}(t_n)}\right)^{-1} = \mathrm{diag}\left(1/\sigma^2_{\widetilde{N}(t_1)}, \cdots, 1/\sigma^2_{\widetilde{N}(t_n)}\right) \tag{4.5}$$

for the resampled time indices $t_1, \cdots, t_n$ and the variance $\sigma^2_{\widetilde{N}(t_i)}$ of $\widetilde{N}$ at time index t_i taken across all 3000 quenches under the assumption of vanishing covariance, we can compute the optimum fit parameters $\theta = (\theta_0, \theta_1)^\top$ that minimize χ^2 using computationally cheap matrix multiplication [71],

$$\theta = \left(X^\top W X\right)^{-1} \cdot \left(X^\top W \widetilde{\mathbf{N}}\right). \tag{4.6}$$

Here, $\widetilde{\mathbf{N}}$ is a column vector where the i-th entry is given by $\widetilde{N}(t_i)$, and $X = \begin{pmatrix} t_1 & 1 \\ \vdots & \vdots \\ t_n & 1 \end{pmatrix}$ a $n \times 2$ matrix.

4.3 Defect types and their unbinding modes

The evaluation of the previous section is purely concerned with the time evolution of the defect number. We proceed by investigating different defect types and unbinding modes in the droplet phase. To analyze the decay modes of defects, we report the time evolution of the defect number distributions post quench in Fig. 4.3. Here, we plot the probability density $P(z)$ instead of $P(N_D(t))$. It is insightful to consider a Poissonian standardization,

$$z(t) = \frac{N_D(t) - \langle N_D(t) \rangle}{\sqrt{\langle N_D(t) \rangle}}, \tag{4.7}$$

as the number of defects decays over time, with $\langle \cdot \rangle$ denoting the mean over all 3000 quenches. This approach allows us to compare distributions with time-shifting means in a single plot.

While the defect number is distributed according to a Poissonian immediately post quench (t = 50 ms), distributions quickly spread. At the end of the simulated time period (t = 1500 ms), the defect number distributions no longer have a single maximum. Instead, they show a local minimum at the mean defect number $z = 0$, with one maximum to either side. This indicates that the system evolves towards two different final states with different decay modes. It also justifies the exclusion of late time steps in the fitting procedure as in the previous section because the decay mode with lower defect number might simply run out of defects to decay.

In a 2D solid, one may distinguish the different lattice defect types disclinations, dislocations and grain boundaries [72].

Disclinations are point-like lattice defects that destroy both translational order as well as angular order. They are defined as lattice points with non-zero charge. We have periodic boundary conditions as we evaluated the kinetic operator and the long-ranged DDI in momentum space. This implies that on a finite domain, disclinations must be generated as pairs, thus not contributing a total charge. We find these pairs to be tightly bound (c.f. Sec. 4.5). Fig. 4.4 illustrates the two fundamental disclinations in a lattice with otherwise hexagonal symmetry with positive and negative unit charge.

Dislocations form another type of point-like lattice defect. In 2D, they terminate an additional layer of lattice points, in our case droplets, stuck partway into the crystal. They preserve angular order, but destroy translational order. Due to periodic boundary conditions, dislocations will always appear as pairs with opposing Burgers-vectors, and each dislocation consists of a pair of defects with opposing charge. Thus, a dislocation may be viewed as a bound pair of disclinations.

Grain boundaries constitute topological line defects. They correspond to the boundaries of domains rotated with respect to each other and may be viewed as a string of dislocations. Again due to periodic boundary conditions, grain boundaries are always closed.

All of the above leads to a vanishing total charge, which we observe in our system (c.f.

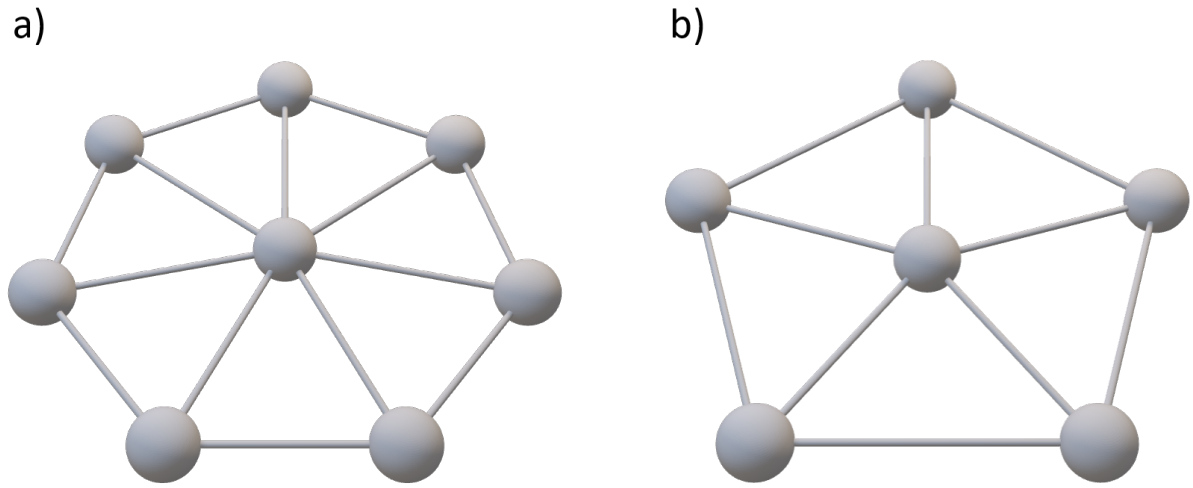

Figure 4.4: Fundamental disclinations in a hexagonal lattice. Panel a) shows a disclination where the central lattice point has seven neighbors, hence it is a defect with positive unit charge. A disclination with negative unit charge is shown in panel b).

Sec. D.3).

These different types of defects are closely related to the observed defect number distributions. Dislocations can move along the additional layer of droplets they terminate, and two pairs of dislocations can annihilate. The relaxation is more nuanced with grain boundaries. Domains with different crystal orientation will grow in time, but since we simulate a finite system, this process cannot continue indefinitely. A common occurrence is the appearance of a pair of grain boundaries running in parallel along the shorter x-dimension. Due to periodicity, the simulated grid is effectively the surface of a torus, so those closed grain boundaries are especially hard to relax. A growing of one crystal domain necessitates shrinking of the remaining crystal domain. If these kind of grain boundaries appear, they are usually long-lived and cause the peak with high defect number observed in the defect number distributions Fig. 4.3.

In Fig. 4.5, we visualize two different final states after 1500 ms time evolution for independent noise realizations within the uniform initialization scheme. Panels a) and b) show the appearance of a pair of dislocations that terminate an additional droplet crystal layer. Panels c) and d) report the formation of a pair of parallel grain boundaries along the x-dimension. While the two crystal domains between these grain boundaries with different crystal orientations are completely devoid of any lattice defects, these grain boundaries constitute of the order of $2L_x/l_x = 32$ long-lived lattice defects. The former final state corresponds to a final state with lower than average defect number, while the latter constitutes a final state within the peak with higher than average defect number visible in the defect number distributions Fig. 4.3.

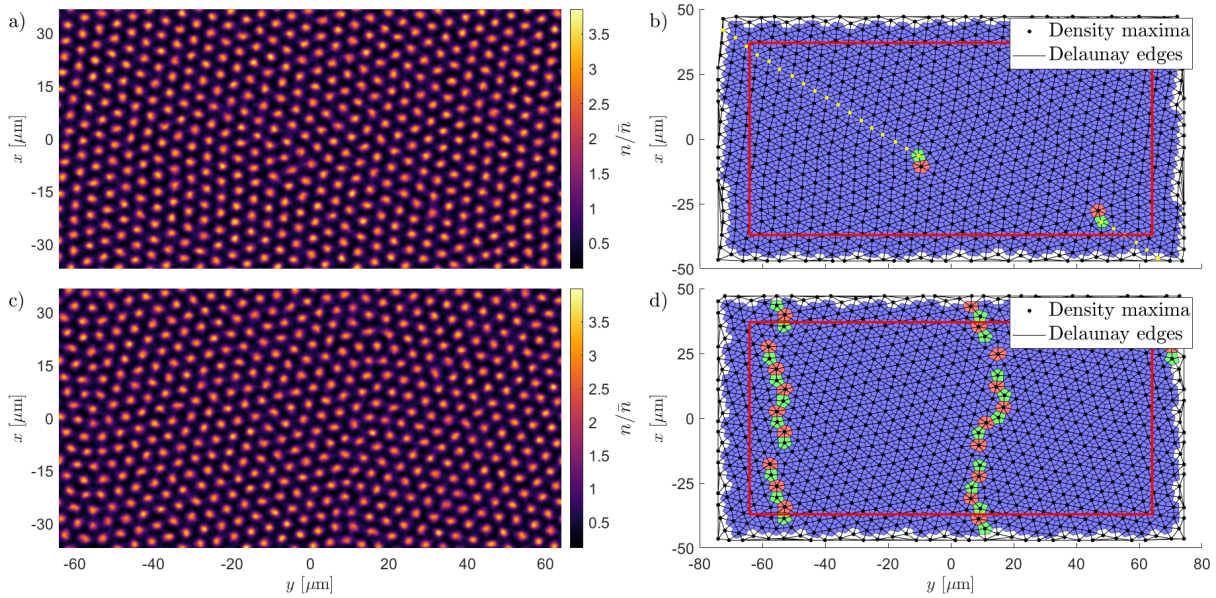

Figure 4.5: Final states after 1500 ms time evolution for independent uniform initializations in the droplet phase, $\bar{n}\cdot a_{dd}^2 = 0.075$, $a_s/a_{dd} = 0.77$. Panels a) and c) show the density distributions of the different final states while the corresponding Voronoi tesselations are reported in panels b) and d). Blue Voronoi cells signify neutral density maxima, whereas green cells distinguish negatively charged maxima from positively charged maxima in red cells. The Delaunay triangulation and the extracted positions of the density maxima are plotted in black atop the Voronoi tesselation. The red rectangles in b) and d) visualize the simulated space-grid corresponding to the support of the density distributions shown in a) and c), respectively, while Voronoi cells and density maxima beyond these rectangles are a result of the padding discussed in Sec. 3.6. Density maxima plotted in yellow in b) highlight the additional droplet crystal layer terminated by the pair of dislocations.

4.4 Angular correlation function g_6 - a hexatic system

Another way to quantify order in a lattice is given by the angular correlation function, which measures correlation of bond orientational order and is given by [73, 74]

$$g_6(r) = \langle \Psi_6^*(r_i)\Psi_6(r_j)\rangle_{|r_i - r_j|\in[r,r+\mathrm{d}r]}, \tag{4.8}$$

for some numerically important bin size $\mathrm{d}r$, with the local bond orientational order parameter

$$\Psi_6(r_i) = \frac{1}{N_i}\sum_k e^{6i\theta_{ik}}. \tag{4.9}$$

Here, the sum $\sum_k$ runs over the N_i lattice neighbors of lattice point i at position r_i. θ_{ik} denotes the angle enclosed by the bond-vector connecting lattice point i to lattice point k and an arbitrary reference axis we take to be $\hat{y} = \begin{pmatrix}0, 1\end{pmatrix}^\top$, and $\langle\cdot\rangle$ refers to the average over all pairs i, j such that $|r_i - r_j| \in [r, r + \mathrm{d}r]$. By symmetry, imaginary parts cancel out and g_6 is real.

Although it might appear lucrative to extract g_6 over as large radii as possible, we have

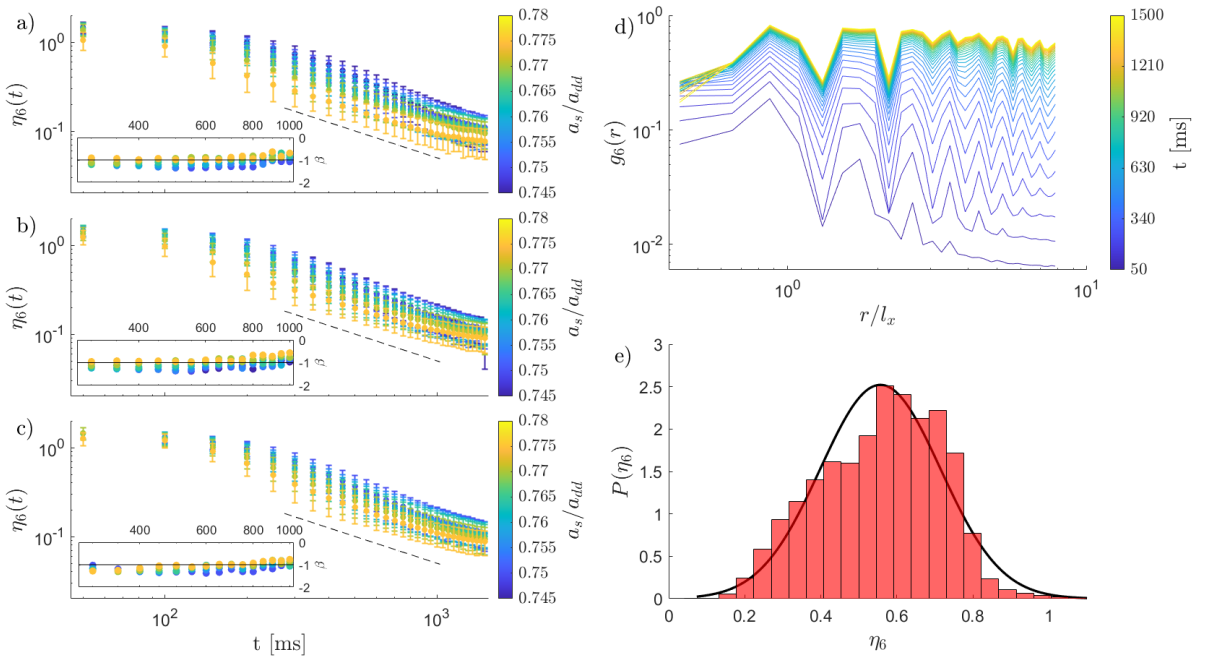

Figure 4.6: Panels on the left side show the time evolution of $\eta_6(t)$ for $\bar{n} \cdot a_{dd}^2 = 0.075$ with uniform initialization (a)), $\bar{n} \cdot a_{dd}^2 = 0.075$ with square lattice initialization (b)), and $\bar{n} \cdot a_{dd}^2 = 0.085$ with uniform initialization (c)), respectively. Color distinguishes different a_s/a_{dd}, and the dashed lines serve to trace t^{-1} scaling. Insets report the local slope β, with black lines signaling $\beta = -1$. Panel d) conveys a single recorded time evolution of $g_6(r)$, for $\bar{n} \cdot a_{dd}^2 = 0.075, a_s/a_{dd} = 0.76$, and with square lattice initialization. Color indicates different times. We omit errors for readability purposes and only report the average g_6 value, taken over 3000 quenches. The results of the bootstrap fit to this data at $t = 300$ ms for 10^5 resamplings are shown in panel e), with a gaussian distribution in black for comparison.

to be mindful of periodic boundary conditions. They require 'wrapping' of the distance measure across the boundaries of the grid, i.e. two lattice points on opposite sides of the grid might actually be close when taking periodicity into account. Thus, since we want to avoid autocorrelation and double counting of lattice parts at different radii, we restrict our analysis of g_6 to distances $r < 8\,l_x$. It is also useful not to evaluate g_6 on length scales smaller than l_x. If there are droplets at these scales, they will induce a defect, thus causing a sudden decrease in g_6 when approaching radii comparable to the unit cell length from above (see Fig. 4.6, panel d)).

A perfect crystal lattice experiences bond orientational order correlation over an infinite range, and therefore $g_6(r) \propto const.$. In a fluid, bond orientational order is short-ranged and decays as $g_6(r) \propto e^{-r/\xi_6}$ for some characteristic correlation length ξ_6, while $g_6(r) \propto r^{-\eta_6}$ in the intermediate hexatic phase [72]. Thus, orientational order is only quasi long-ranged.

We observe that our system is best described by $g_6(r) \propto r^{-\eta_6(t)}$, with the spatial decay constant $\eta_6(t)$ decaying algebraically in time itself. For every time step, we extract η_6 with a bootstrap approach similar to the bootstrap in Sec. 4.2, and the approach is validated

by the obtained η_6 distributions shown in Fig. 4.6, panel e). Although η_6 is not distributed in a strictly gaussian fashion, this panel still justifies to get an estimator of the true η_6 value by taking the mean across all resamplings, and estimate an error based on the width of the distribution. The time behavior of η_6 is given by power law scaling $\eta_6(t) \propto t^{\beta}$, as shown in Fig. 4.6, panels a) through c). β can be computed as the slope in log-log space, $\beta = d\log\eta/d\log t$. Since g_6 has been computed at times t_i with finite separation, we show the finite distance instantaneous slope

$$\beta_{\text{inst}}(t_i) = \frac{\log\eta(t_{i-1}) - \log\eta(t_{i+1})}{\log t_{i-1} - \log t_{i+1}} \tag{4.10}$$

in the insets of Fig. 4.6, panels a) through c).
At late times, η_6 decreases in absolute value, which signals a slower increase in correlation. As discussed in Sec. 4.3, this can be traced back to the formation of grain boundaries spanning the entire system, i.e. a quasi-stable state where a uniform increase in domain size is no longer possible.

4.4.1 χ_6 - another approach to bond orientational order

The analysis in the previous section relies heavily on the supersolid experiencing a hexatic phase, i.e. $g_6(r,t) \propto r^{-\eta_6(t)}$. As $g_6(r)$ is subject to extensive influence of finite size effects in the range accessible to the present work[7], we test the hexatic assumption by computing the angular susceptibility

$$\chi_6 = \langle|\Psi_6^{\text{sub}}|^2\rangle, \tag{4.11}$$

as suggested in [75]. We redefine the local bond orientational order parameter Eq. (4.9) to span a subsystem,

$$\Psi_6^{\text{sub}} = \frac{1}{N_{\text{sub}}}\sum_i \frac{1}{N_i}\sum_k e^{6i\theta_{ik}}, \tag{4.12}$$

where the sum $\sum_i$ runs over the N_{sub} lattice points in a given subsystem, $\sum_k$ sums the N_i nearest neighbors of a given lattice point, θ_{ik} as defined before, and $\langle\cdot\rangle$ denotes the average over different subsystems with the same size. Since our system is rectangular with aspect ratio $\sqrt{3}$, we compute χ_6 for subsystems with the same aspect ratio. To this end, we simply tile the entire system with rectangles of size $l \times \sqrt{3}\cdot l$, and $l/l_x \in \{1,2,4,8\}$.
χ_6 serves to distinguish different phases. A perfect, infinite solid is subject to $\chi_6 = 1$ due to long-ranged order, and the lack of this order prompts a fluid to behave as $\chi_6 \propto 1/N_{\text{sub}}$. A uniform hexatic phase with quasi long-ranged order can be distinguished from the two

[7] We expect neighboring lattice points to be separated by the unit cell length l_x in a periodic hexagonal lattice. If we observe the next lattice point at more than unit cell length separation, it likely constitutes a defect and hence decreases g_6. Generalizations hold for the k-th nearest lattice point, causing an oscillatory behavior of g_6. This leads to the sudden decrease of g_g at $r/l_x \sim 1.5$ clearly visible in Fig. 4.6. As the number of lattice points enclosed in a spherical shell of thickness dr in $d = 2$ dimensions increases as $2\pi r\mathrm{d}r$, the magnitude of this effect decreases and g_6 is less oscillatory at larger radii.

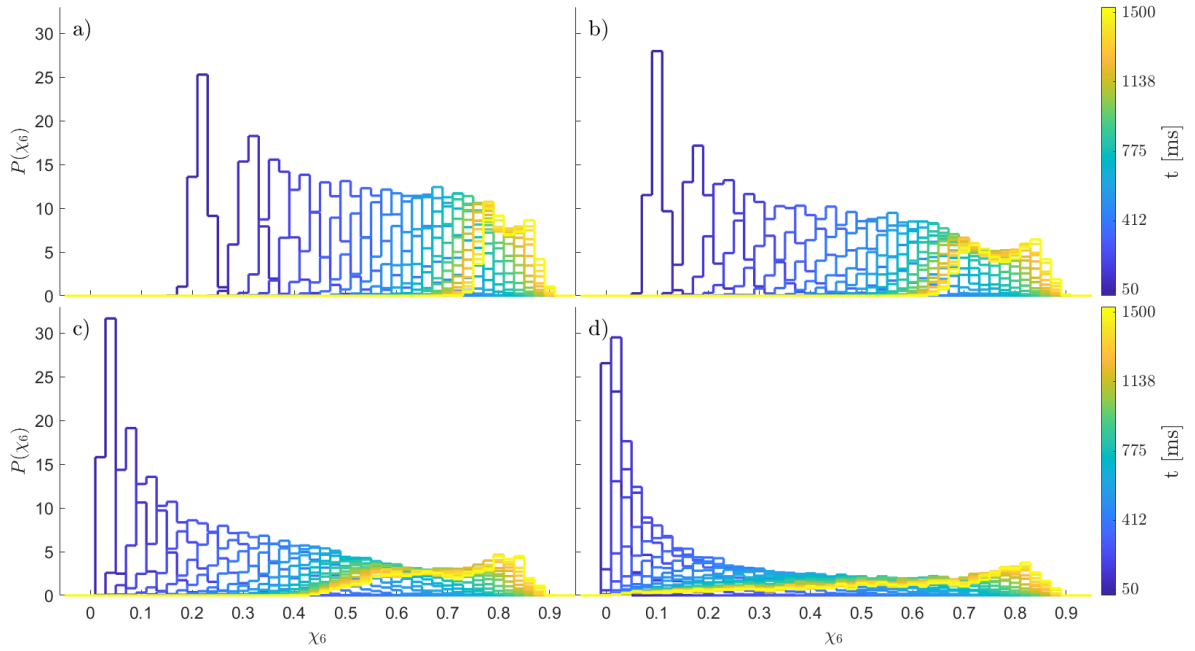

Figure 4.7: Time evolution of χ_6 distributions for $\bar{n} \cdot a_{dd}^2 = 0.075$, $a_s/a_{dd} = 0.760$ and uniform initialization. Panels a) through d) show χ_6 distributions recorded for increasing subsystems of size $l \times \sqrt{3} \cdot l$, where $l/l_x \in \{1, 2, 4, 8\}$ in panel {a), b), c), d)}.

extremes if the χ_6 distributions are qualitatively irrespective of the subsystem size [75]. We observe the latter to be the case in our system, as demonstrated in Sec. 4.5.

4.4.2 Defect pair formation and inter-defect distance

Another approach to distinguishing a fluid from a hexatic phase is presented by the inter-defect distance. In the hexatic phase, disclinations are bound by a logarithmic potential while being free in a fluid [72]. Therefore, if we observe clustering of defects into pairs, i.e. if the inter-defect distance is one lattice bond, the system is in a hexatic phase. We find overwhelming evidence for this clustering (Sec. 4.5). This also rules out the possibility to estimate the growing of the length scale $\xi(t)$ from the inter-defect distance, as has been done for vortices in a uniform superfluid [19].
Together with the χ_6 analysis, we conclude that the hexatic assumption is reasonable despite prominent finite size effects.

4.5 Substantiation of the hexatic assumption

In Sec. 4.4, we claim to analyze a system in a hexatic phase, and outline two approaches to validate this assumption beyond the shape of $g_6(r)$, namely the angular susceptibility and the inter-defect distance. Here, we supply aforementioned evidence justifying the hexatic assumption.

4.5.1 Hexatic properties of χ_6

Fig. 4.7 holds several important conclusions. In general, and irrespective of subsystem size, χ_6 increases as a function of time. This indicates an increase in bond orientational correlation, which matches closely with the $g_6(r)$ analysis. A second key observation is that for a given time, the overall shape of the χ_6 distributions is similar for different subsystem sizes. There is only a minor shift towards lower values of χ_6 and a broadening of the distribution with increasing subsystem size. Larger subsystems are more likely to include grain boundaries, which destroy angular order and decrease χ_6. The broadening is a result of averaging as there are less subsystems with increasing subsystem size. A single grain boundary therefore has a major impact on the χ_6 distribution in large subsystem, but influences only a minor number of subsystems if the size of the subsystem is small. Crucially, the χ_6 distributions cannot be viewed as the sum of a solid-like and a fluid-like distribution, which would be the case in an inhomogeneous two-phase system.
We find this pattern across the entirety of the explored parameter space, and validate the hexatic assumption.
For the sake of completeness and to avoid ambiguities, we want to add that there is another conflicting definition of the angular susceptibility [72] including the square of the mean Ψ_6^{sub},

$$\chi_6 = \langle |\Psi_6^{\text{sub}}|^2 \rangle - \langle |\Psi_6^{\text{sub}}| \rangle^2, \tag{4.13}$$

with the modified local bond orientational order parameter as in Eq. (4.12). However, we make use of the simpler definition Eq. (4.11) because we are only interested in the qualitative interpretation of χ_6 presented above. Using the square of the mean instead of the variance has the benefit that it allows to distinguish solid-like ($\chi_6 \approx 1$) from fluid-like ($\chi_6 \approx 0$) phases directly, and it is straightforward to spot a superposition of a solid-like and a fluid-like distribution indicative of an inhomogeneous two-phase system.

4.5.2 Inter-defect distance across the parameter space

We observe strong clustering of lattice defects (see Fig. 4.8) across the entirety of the traversed parameter space. As a crystal is by definition subject to periodicity, it can be insightful not to measure the distance to the nearest defect in harmonic oscillator units or even μm. Instead, we report the graph distance d. To this end, we construct a graph out of the lattice structure, with droplets corresponding to vertices, and inter-droplet bonds defining the adjacency in that fully connected, planar, undirected, unit-weighted graph. For any lattice defect, i.e. for each vertex with adjacency unequal to six, we compute the number of edges separating this lattice defect from the next. By quoting the distance in the number of edges, we account for the inherent discreteness of the problem.
Almost the entire probability weight is concentrated in the first bin, i.e. at one edge separation corresponding to clustered defects. Finding a separation of more than one

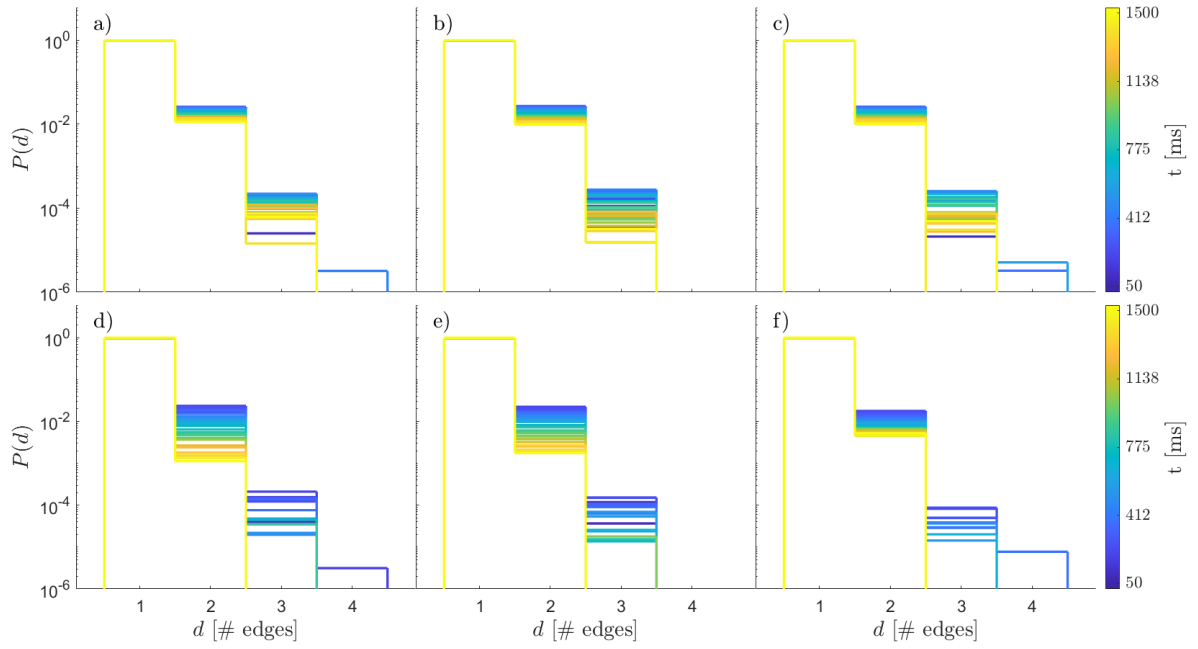

Figure 4.8: Time evolution of graph distance distribution to the nearest lattice defect. Panels left to right show different initial conditions: $\bar{n} \cdot a_{dd}^2 = 0.075$ with uniform initialization (a), d)), $\bar{n} \cdot a_{dd}^2 = 0.075$ with square lattice initialization (b), e)) and $\bar{n} \cdot a_{dd}^2 = 0.085$ with uniform initialization (c), f)). Upper panels hold data recorded at the lowest respective scattering length ($a_s/a_{dd} = 0.745$ in a), b) and $a_s/a_{dd} = 0.75$ in c)), while the lower panels represent the largest analyzed scattering length ($a_s/a_{dd} = 0.775$ in d), e) and $a_s/a_{dd} = 0.78$ in f)), and color serves to distinguish different times.

edge is increasingly unlikely, with the probability density decreasing by about two orders of magnitude for any additional edge, and we find this observation to hold true irrespective of initial conditions.

Although this result is far more indirect than the shape of the χ_6 distributions, it still serves as a cross-check to validate the hexatic assumption and rules out a fluid phase with free disclinations.

4.6 Late-time scaling exponents of the lattice defect coarsening in the honeycomb phase

We largely employ the same methods as in the droplet phase to analyze the defect coarsening in the honeycomb phase. Similar to Fig. 4.2, we report the time evolution of the transformed defect number for different states in the honeycomb phase in Fig. 4.9, panels a) through c), where we extract the scaling exponent α and t^* with a bootstrap fit in panels d) and e), respectively.

Irrespective of average particle area density, we find the same time evolution of the defect number distribution as in Fig. 4.3. The condensate evolves towards two distinct final states. One final state is devoid of defects, representing the true supersolid ground state. On the other hand, there is a second final state with finite defect number, corresponding

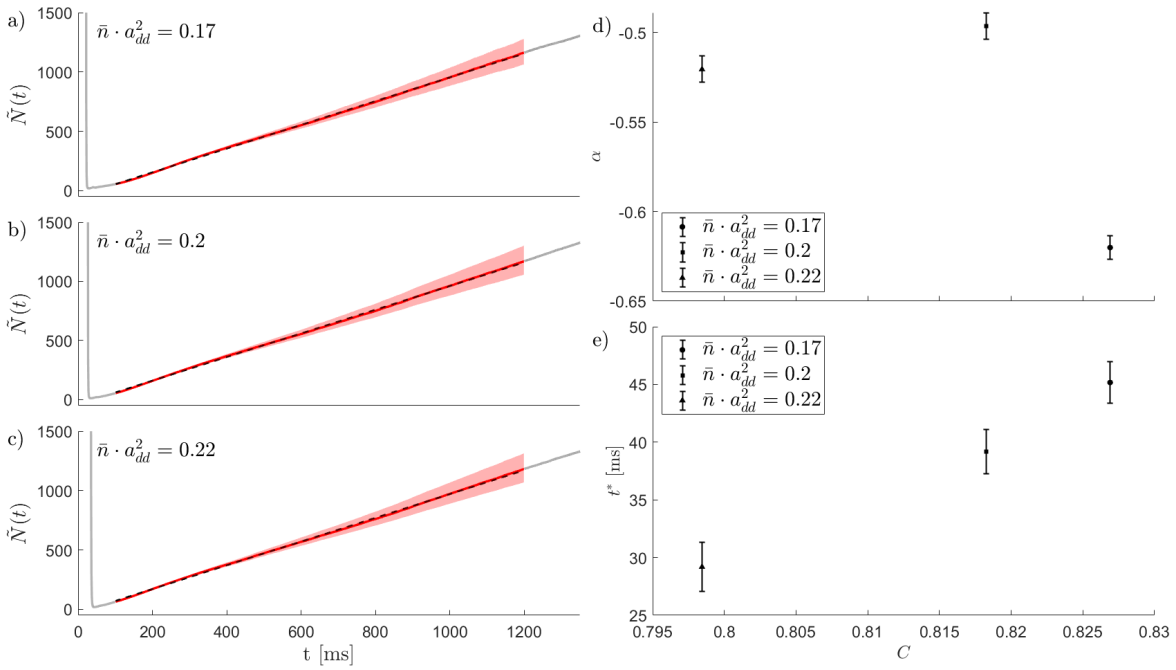

Figure 4.9: Lattice defect decay in the honeycomb phase for different average densities. Panels {a), b), c)} show the defect coarsening for $\bar{n} \cdot a_{dd}^2 = \{0.17, 0.2, 0.22\}$ and $a_s/a_{dd} = 0.78$. Data shown in gray corresponds to early and late times excluded from the fit. Dashed lines represent the best linear fit obtained by the bootstrap method and shading indicates error regions for data considered in fitting. Panel d) shows the extracted scaling exponents, and the corresponding t-axis intercepts are depicted in panel e) as a function of density contrast C. For better readability, errors in d) and e) are scaled by a factor of 5. Results after 5000 bootstrap resamplings.

to a final state with global grain boundaries. This shows that the honeycomb experiences the same defect decay modes as the droplet phase.

4.7 Angular correlation in the honeycomb phase

In analogy to the droplet phase, we find the different states in the honeycomb phase to behave as a hexatic system as well, as verified in Sec. D.4. Fig. 4.10 shows the algebraic decay of both $g_6(r) \propto r^{-\eta_6}$ with notable finite-size effects (panel d)) and $\eta_6(t) \propto t^{-\beta}$ (panels a) through c)). The bootstrap approach is validated in panel e).

4.8 Interpretation of topological defect coarsening

While we have already discussed the different defect decay modes in Sec. 4.3, we have yet to discuss the scaling exponents of the algebraic decay of both the defect number and the angular correlation function. In the droplet phase, the defect decay is faster at larger contrast. This matches closely with a faster increase in bond orientational order, i.e. larger $|\beta_{\text{inst}}|$. This result seems counterintuitive at first. At lower contrasts, there is a larger superfluid background promoting particle flow between droplets, which should

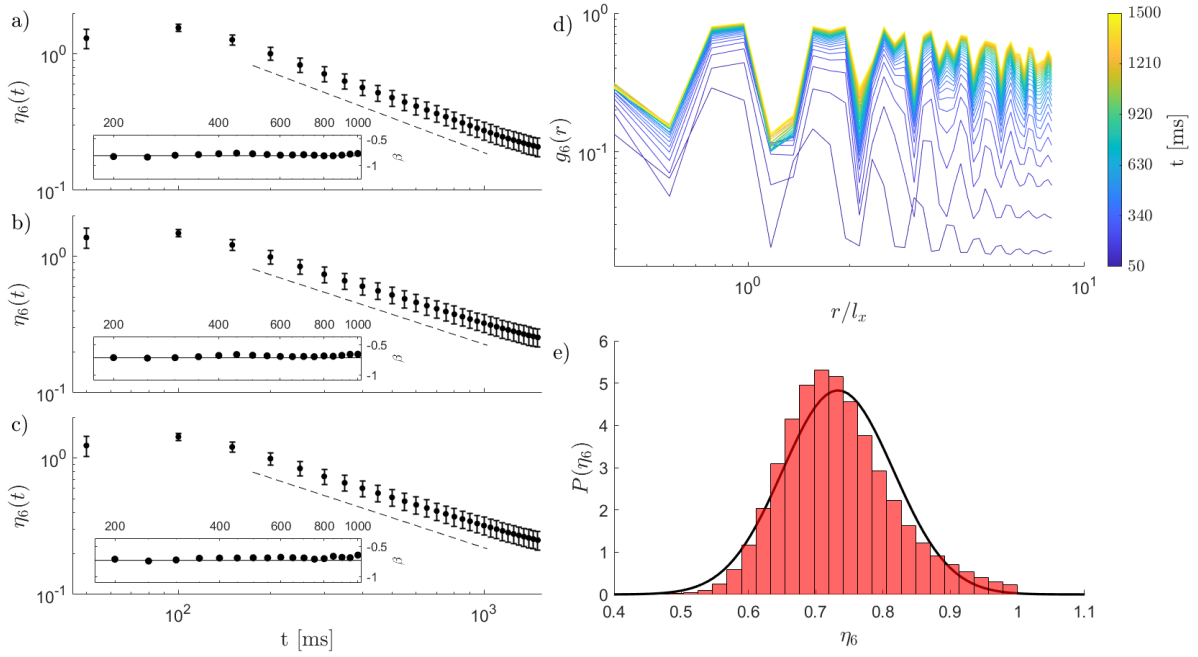

Figure 4.10: Panels {a), b), c)} show the time evolution of $\eta_6(t)$ for $\bar{n} \cdot a_{dd}^2 = \{0.17, 0.2, 0.22\}$ and $a_s/a_{dd} = 0.78$. Insets report the local slope β, with black solid and dashed lines signaling $\beta = \{-0.845 \pm 0.010, -0.729 \pm 0.006, -0.734 \pm 0.008\}$ in {a), b), c)}. Panel d) conveys a single recorded time evolution of $g_6(r)$, for $\bar{n} \cdot a_{dd}^2 = 0.2, a_s/a_{dd} = 0.78$. Color indicates different times. We omit errors for readability purposes and only report the average g_6 value, taken over 3000 quenches. The η_6 results of the bootstrap fits to $g_6(r) \propto r^{-\eta_6}$ at $t = 300$ ms for 10^6 resamplings are shown in panel e), with a gaussian distribution in black for comparison.

increase the relaxation speed. However, particles can also be redistributed in the system by moving droplets themselves, thus keeping the particles within the same droplet. This is to be expected in the large contrast regime. Additionally, a lattice defect presents less of a disturbance of the condensate's density in the low contrast regime as the modulation around the average particle area density is small. This is in opposition to the high density regime, where the condensate density vanishes between droplets. Thus, a lattice defect is a large deviation from the energetically favorable ground state. Finally, an increase in contrast is associated with an increase of the relative strength of the DDI compared to contact interaction in the quenches considered in the present work. As the long-ranged DDI is responsible for the appearance of supersolid properties, the faster defect decay in the large contrast regime might be a result of this relative increase in DDI strength. Ultimately, the exact decay mechanism remains elusive within the scope of this work, and we will discuss possible methods to distinguish particle exchange between droplets vs. redistribution of droplets in Sec. 6.

We also observe that the time shift t^* in the algebraic scaling decreases with increasing contrast in the droplet phase. The decrease in $t^* = t_1 - t_2$ has a simple interpretation. In the high contrast regime, the transition time between the early-time and late-time scaling regimes shifts towards later times (as discussed in Sec. D.1) such that at the onset time t_1

of the algebraic scaling in the late-time scaling regime, many lattice defects have already decayed and we have $t_2 > t_1$. A smaller defect number at the beginning of the algebraic late-time scaling corresponds to a larger t_2 since t_2 denotes the time needed for the defect number to decay to its initial value at the onset of the late-time algebraic scaling regime. Remarkably, initializing the system with droplets in a square lattice has no major impact, neither on the scaling exponent α nor on t^*. This emphasizes that the ground state contrast is an appropriate measure to compare datasets with different initial conditions. In the honeycomb phase, it is harder to interpret the decay coefficients. As we consider quenches to the same s-wave scattering length with different average densities, an increase in contrast does not correspond to an increase in relative DDI strength. Additionally, we analyze only three different parameter combinations in the honeycomb phase with similar contrast, which limits the ability to give general conclusions. Nonetheless, we make several observations that allow first conclusions. At constant scattering length, increasing the average density reduces contrast as the honeycomb lattice is forced to expand and broaden into the low density regions by added particles. This increases the minimum density and therefore reduces contrast. Additionally, t^* increases with contrast. This shows that prescaling is faster at greater average densities, indicating a promotion of particle flow in a broadened lattice. The scaling exponents, however, do not reveal a clear pattern because we only analyze the defect decay with three different parameter combinations, as discussed above.

5 Vortex statistics

Vortices constitute another type of defect, albeit not to the supersolid crystal structure itself, but rather to the condensate, as the local density vanishes at the core of a vortex [7]. Instantaneous quenches of the s-wave scattering length represent a violent disruption to a BEC, especially since we quench across the superfluid-supersolid phase boundary. This leads to the formation of vortices. We find a non-universal dependence of the vortex number N_v on initial conditions. In particular, we observe wildly varying N_v as a function of a_s/a_{dd}. The deeper the quench, i.e. the smaller a_s/a_{dd}, the larger N_v. Fig. 5.1 shows the initial vortex number N_v^0 at the first recorded timestep $t_0 = 50$ ms post quench for quenches in the droplet phase. The initial vortex number varies by 3 (!) orders of magnitude in the range $0.745 \leq a_s/a_{dd} \leq 0.765$. For greater scattering length, we do not observe vortices at $t \geq 50$ ms. The honeycomb phase is completely devoid of vortices in the parameter space explored by the present work. Therefore, we restrict our vortex statistics analysis to quenches with $\{\bar{n} \cdot a_{dd}^2, a_s/a_{dd}\} = \{0.075, 0.745\}$. Here, we operate in the large N limit where the mean vortex number stays sufficiently large throughout the quench to get statistically meaningful results.

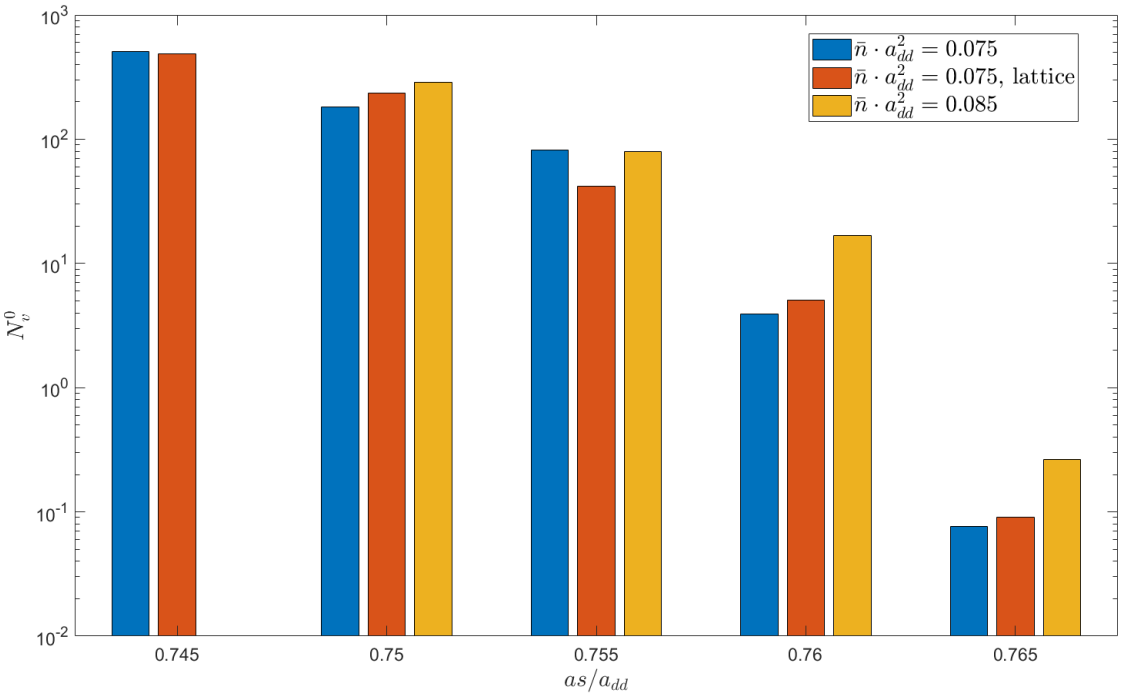

Figure 5.1: Vortex number 50 ms post quench in the droplet phase for different average densities and initialization schemes.

5.1 Vortex spacing distribution

Quenches of the chemical potential lead to vortices distributed according to a Wigner-Dyson distribution in a uniform condensate [25, 67], where the distance s between vortices obeys

$$P(S = s/\langle s \rangle) = \frac{\pi}{2} S \exp\left(-\frac{\pi}{4} S^2\right), \tag{5.1}$$

immediately post quench, and $S = s/\langle s \rangle$ in terms of the mean vortex spacing $\langle s \rangle$. Specifically, $P(S)\mathrm{d}S$ yields the probability to find the nearest vortex at a normalized distance between S and $S + \mathrm{d}S$, and $N_v - 1$ vortices at greater distances. This can be generalized to the k-th nearest neighbor spacing distribution [67][8],

$$P^{(k)}(S) = \frac{2}{(k-1)!} r^{2k} S^{2k-1} \exp\left(-r^2 S^2\right), \tag{5.2}$$

with $r = \Gamma(\frac{1}{2} + k)/\Gamma(k)$, and $\Gamma(x)$ the gamma function. Analogously to Eq. (5.1), the distribution in Eq. (5.2) describes the probability to find the k-th nearest vortex at a normalized distance between S and $S + \mathrm{d}S$, with $k - 1$ vortices at a smaller distance

[8] Note that Eq. (17) of [67] erroneously uses r^{2k-1} instead of r^{2k}, whereas the correct r^{2k} is used in Eq. (A5). The correct exponent of r is a result of the normalization condition $\int_0^\infty \mathrm{d}S\, P^{(k)}(S) = 1$. We obtain $\int_0^\infty \mathrm{d}S\, P^{(k)}(S) = \frac{2}{(k-1)!} r^{2k} \int_0^\infty \mathrm{d}S\, S^{2k-1} \exp\left(-r^2 S^2\right) \overset{u=r^2S^2}{=} \frac{2}{(k-1)!} r^{2k} \int_0^\infty \mathrm{d}u\, \frac{1}{2r^2} \left(\frac{u}{r^2}\right)^{k-1} \exp(-u) = \frac{\Gamma(k)}{(k-1)!} = 1$ using the definition of the gamma function and $\Gamma(k) = (k-1)!\, \forall\, k \in \mathbb{N}^+$, as required.

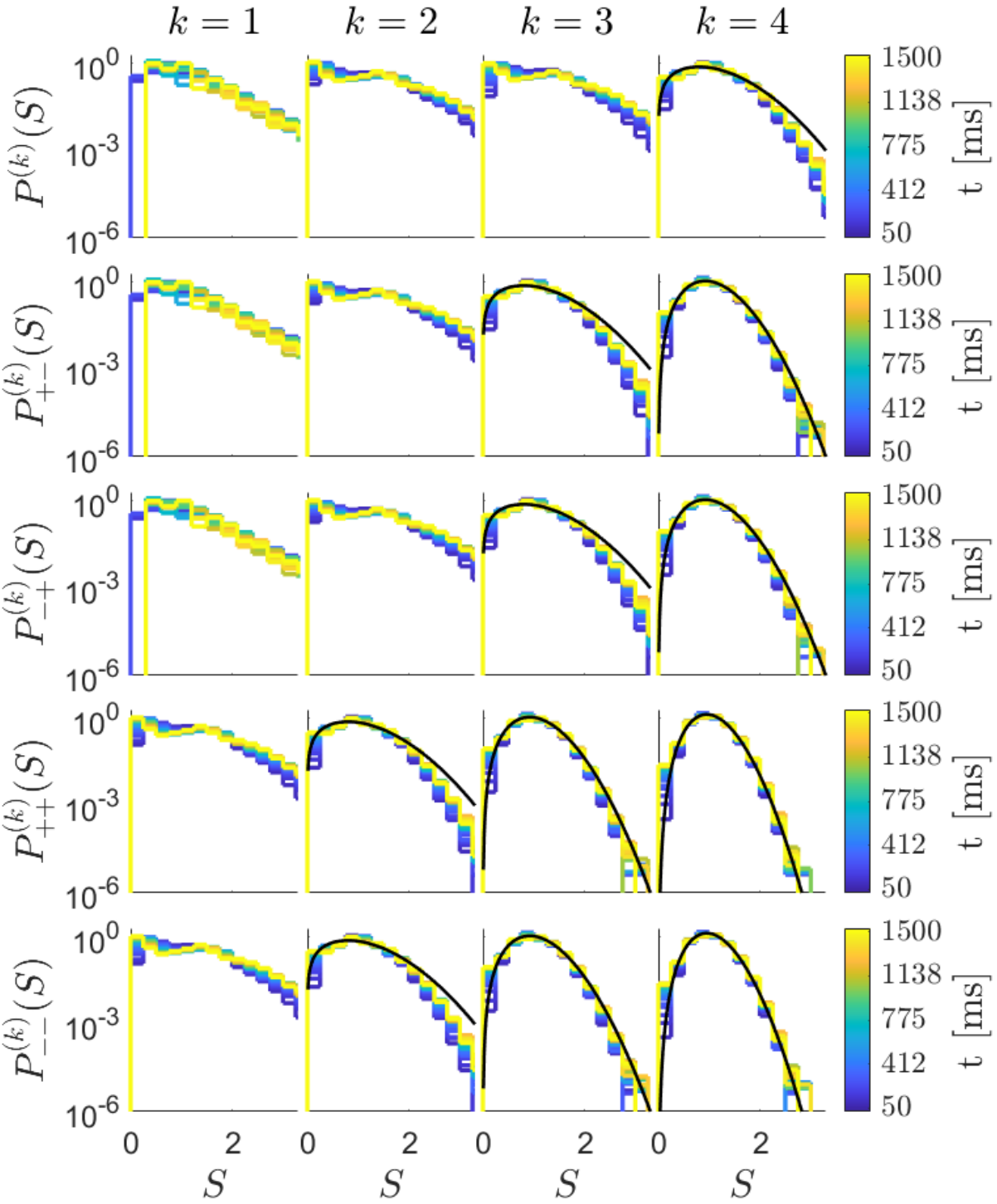

Figure 5.2: Time evolution of vortex spacing distributions for $\bar{n} \cdot a_{dd}^2 = 0.075$ and $a_s/a_{dd} = 0.745$ with uniform initialization. Panels left to right distinguish increasing k, while panels top to bottom display vortex spacing distributions under different charge constraints. Color indicates different times. Plotted in black are generalized Wigner-Dyson distributions $\tilde{P}^{(k)}(S)$. We show $\tilde{P}^{(1)}(S)$ in the row corresponding to $P^{(k)}(S)$, $\tilde{P}^{(1)}(S)$ and $\tilde{P}^{(2)}(S)$ in the rows corresponding to $P^{(k)}_{+-}(S)$ and $P^{(k)}_{-+}(S)$, and $\tilde{P}^{(1)}(S)$, $\tilde{P}^{(2)}(S)$, and $\tilde{P}^{(3)}(S)$ in the rows corresponding to $P^{(k)}_{++}(S)$ and $P^{(k)}_{--}(S)$, from left to right. Logarithmic y-axis serve to highlight deviations in the tails of the distributions where probability weight is low.

and $N_v - k - 1$ vortices at a greater distance. These distributions are independent of the vortex charge and refer to a generic vortex. We will also analyze these spacing distributions considering topological vortex charge, and use the notation $P^{(k)}_{QQ'}$ to refer to the conditioned k-th nearest vortex spacing distribution, given that the reference vortex at $s = 0$ has charge Q, and the k-th nearest vortex at distance s has charge Q'. Note that also the mean vortex spacing $\langle s \rangle$ used in the normalization $S = s/\langle s \rangle$ is calculated with charge constraints applied to the inter-vortex distances, i.e. in the calculation of a charge constrained inter-vortex distance distribution, the distances are normalized to an average separation calculated from inter-vortex distances obtained from vortices fulfilling the given constraints. Additionally, we will henceforth denote the theoretical prediction Eq. (5.2) as $\tilde{P}^{(k)}(s)$ to distinguish measured quantities from theoretical predictions. Note that we consider all vortices to carry unit charge as discussed in Sec. 3.3 and only distinguish the signs of their respective charges. As we treat these distributions as an ensemble average,

$$P^{(k)}_{QQ'}(S) = P^{(k)}_{QQ'}\left(\frac{s_{ij}}{\langle s_{ij} \rangle}\right)_{s_{ij} \in [s, s+\mathrm{d}s];\, i,j = 1 \ldots N_v}, \tag{5.3}$$

where s_{ij} denotes the distance from the i'th vortex to the j'th vortex, i.e we do not consider a single vortex as the origin, we expect the symmetries $P^{(k)}_{+-} = P^{(k)}_{-+}$ and $P^{(k)}_{++} = P^{(k)}_{--}$ in the conditioned vortex spacing distributions.

In our data presented in Fig. 5.2, we observe several symmetries. Firstly, we observe $P^{(k)}_{+-}(S) = P^{(k)}_{-+}(S)$ and $P^{(k)}_{++}(S) = P^{(k)}_{--}(S)$ for all $k = 1, 2, 3, 4$, as expected. However, there are the additional symmetries $P^{(1)}(S) = P^{(1)}_{+-}(S)$, $P^{(2)}(S) = P^{(3)}(S)$, $P^{(4)}(S) = P^{(3)}_{+-}(S)$ and $P^{(k+1)}_{+-}(S) = P^{(k)}_{++}(S)$ for $k = 2, 3, 4$. These symmetries reveal clustering of vortices into pairs, where a pair consists of two vortices with opposing topological charge. Suppose all vortices cluster into pairs with opposing charge, then $P^{(1)}(S) = P^{(1)}_{+-}(S)$. Also, since the second and third nearest vortices constitute a pair, we have $P^{(2)}(S) = P^{(3)}(S)$ if the pair separation distance is much larger than the binding length of a vortex pair. Finally, since every reference vortex is bound to a vortex with opposing charge, we have $P^{(k+1)}_{+-}(S) = P^{(k)}_{++}(S)$ for $k = 2, 3, 4$. Quantitatively, we observe convergence of the vortex spacing distributions to generalized Wigner-Dyson distributions with increasing k. While the shape of distributions at small k remains elusive, we have $P^{(3)}_{++}(S) = \tilde{P}^{(2)}(S)$ and $P^{(4)}_{++}(S) = \tilde{P}^{(3)}(S)$. The symmetries given above also imply $P^{(4)}_{+-}(S) = \tilde{P}^{(2)}(S)$.

The fact that the vortex spacing distributions in the supersolid phase differ significantly from vortex spacing distributions in a uniform phase is expected, for two reasons.

Firstly, the Wigner-Dyson distribution arises from the assumption that the vortex spacing follows Poisson arrivals on a plane, i.e. the vortex distances to a reference point obey Poissonian statistics [76]. This, in turn, assumes translational invariance since the reference point is arbitrary, and no position is favored with respect to another location. However, translational invariance of the condensate density is broken in the supersolid

phase by construction. As vortices in a supersolid concentrate in regions with low particle area densities [41], translational invariance is also broken for vortex distribution. In particular, vortices nest in the low density regions between droplets.
Secondly, vortices themselves interact with a logarithmic potential where vortices with opposing charge attract each other [25, 67]. As we allow for dynamics, i.e. we do not extract vortex spacing distributions immediately post quench, the vortex spacing distributions are significantly altered by inter-vortex interactions and interactions between vortices and droplets. On large scales, i.e. at vortex spacing distances larger than l_x, however, the vortex-droplet interaction is negligible. The vortex-vortex interaction is also short-ranged due to the logarithmic potential. Consequently, we expect to recover generalized Wigner-Dyson distributions on large scales and correspondingly in the large k regime, which is realized in our data. This shows that the vortex spacings initially obey Poissonian statistics, but vortex-droplet and inter-vortex interactions quickly alter spacing distributions on small length scales.

5.2 Vortex number distribution

Another important distribution is the vortex number distribution $P(N_v)$, which describes the probability density distribution to find a given vortex number N_v in a single quench. The formation of vortices can be modeled by a binomial distribution [67],

$$P(N_v) = \binom{N_d}{N_v} p^{N_v} (1-p)^{N_d - N_v}, \tag{5.4}$$

where $N_d = A/\xi_v^2$ denotes the number of expected domains for vortex formation in a BEC of size A, and p describes the probability to form a vortex in a given domain. ξ_v is the typical length scale of vortex formation. A binomial distribution tends to a Gaussian distribution in the large N_v limit,

$$P(N_v) \propto \exp\left\{ -\frac{(N_v - \langle N_v \rangle)^2}{\langle N_v \rangle} \right\}, \tag{5.5}$$

with $\langle N_v \rangle$ the average vortex number at a given timestep taken across all 3000 quenches. Eq. (5.4) only makes assumptions on the formation process of vortices, and, *a priori*, must not be assumed to hold throughout the time evolution post quench. However, we find this to be the case in our data shown in Fig. 5.3. The vortex number distribution remains Gaussian throughout the quench, albeit with a time-dependent mean. Unlike the lattice defect unbinding mechanism (see Fig. 4.3), this indicates uniform annihilation of vortex anti-vortex pairs, i.e. pairs of vortices with opposing topological charge.

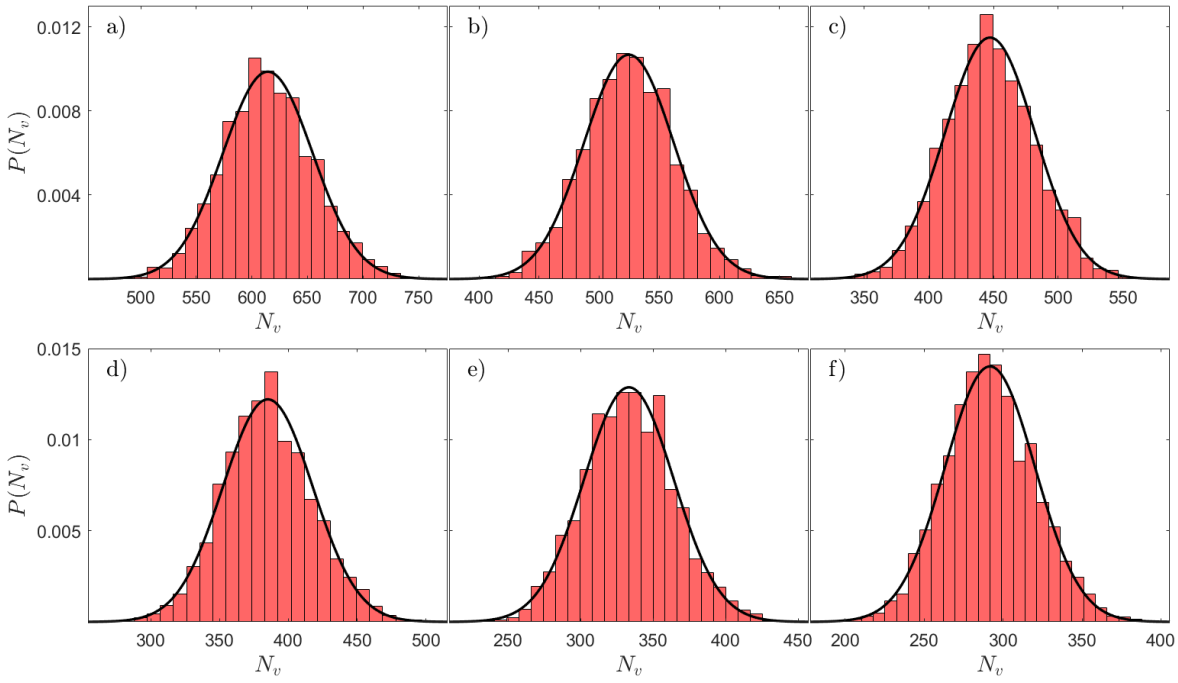

Figure 5.3: Time evolution of the vortex number distribution for $\{\bar{n} \cdot a_{dd}^2, a_s/a_{dd}\} = \{0.075, 0.745\}$ and uniform initialization. Red histograms show the data from all 3000 quenches, and plotted in black is a Gaussian according to Eq. (5.5). Panels {a), b), c), d), e), f)} correspond to times $\{1, 2, 3, 4, 5, 6\} \cdot 250$ ms post quench.

5.3 Supersolid influence on vortices

The presence of vortices in the supersolid phase highlights that a condensate in this phase still exhibits superfluid properties. However, it is striking to observe more vortices at small scattering lengths, corresponding to supersolid states with large contrast $C \to 1$. Superfluidity can be quantified using the superfluid fraction f_s. At nonzero temperature, Landau's two component theory of superfluidity [31] predicts that the superfluid density does not coincide with the total density. There is a 'normal' component that lacks superfluid properties, and f_s describes the fraction of a system with superfluid properties. In our setup, we do not consider thermal occupation and thus, in a state lacking supersolidity, i.e. $C \to 0$, we have $f_s = 1$. However, by breaking continuous translational invariance in a supersolid state, f_s can deviate from unity even at zero temperature, and the phase diagram [22] shows that states with larger contrast will in general experience lower f_s. From this, we conclude that supersolidity protects vortices from annihilating quickly via the droplet-vortex interaction. By nesting in the low density regions between droplets, vortices are not free to move like in a uniform state, so supersolidity influences vortex annihilation beyond the inter-vortex interaction with logarithmic potential. This matches closely with the deviations of the vortex spacing distributions from generalized Wigner-Dyson distributions observed in Sec. 5.1.

We note that contrast also has an influence on the generation of vortices. In the low contrast regime, the background density remains high, and, as the density must vanish at the

core of a vortex, this inhibits the generation of vortices. On the other hand, supersolids in the high contrast regime are already subject to very low minimum densities by definition of the contrast Eq. (2.23), which promotes the creation of vortices.

6 Conclusion and outreach

In this thesis, we have analyzed the formation process of 2D supersolids after quenches of the s-wave scattering length. We showed that the number of lattice defects experiences two algebraic scaling regimes with different scaling exponents in the droplet phase. In the late-time scaling regime, the defect decay is faster if the condensate is subject to large contrasts. However, the exact defect decay mechanism remains elusive. In both the droplet and the honeycomb phase, the forming supersolid is found to experience the quasi long-ranged bond angular order typical for a hexatic system, prompting the algebraic decay of the angular bond-order correlation function $g_6(r) \propto r^{-\eta_6}$. Again, matching closely the defect of lattice defects, bond order is increasing faster in the large contrast regime.
Additionally, investigating vortices, their spacing distributions and their number distributions, we have observed a hallmark property of superfluids. Apart from vortex droplet interactions on small length scales, we find that the distribution of vortices in a supersolid can be modeled by Poissonian arrivals on a plane. This manifests itself in the emergence of Wigner-Dyson-like vortex spacing distributions. We conclude that the vortex anti-vortex annihilation process is unimodal as the defect number distribution remains Gaussian throughout the time evolution of the condensate post quench.
Finally, we remark on a systematic error we committed in the analysis of both $\widetilde{N}_D(t)$ and $g_6(r)$. With the benefit of hindsight, and acknowledging the observed algebraic scaling, these quantities should be extracted over logarithmically spaced domains. In our analysis, they were extracted over linear domains, which leads to unequal sensitivity, i.e. fits are dominated by properties in the large t and large r regime, respectively.
Concluding, we want to point out several possible continuations to this thesis.
The analysis of the lattice defect decay process has been restricted to the late-time scaling regime. However, the presented methods could also be applied to the early-time algebraic scaling regime. Additionally, the influence of initial conditions on the transition time between the different scaling regimes may be analyzed in more detail.
Beyond the reuse of the discussed methods, we propose five additional methods to further the understanding of the supersolid formation process.
Firstly, in the droplet phase, it would be beneficial to analyze the systems for global phase coherence. Especially for deep quenches, i.e. quenches with low a_s, it cannot be ruled out that the system transitions to an isolated droplet regime lacking phase coherence and therefore losing supersolid properties. A global measure for phase coherence is given by

$$\mathcal{P}(t) = 1 - \frac{2}{\pi} \frac{\int \mathrm{d}^2\mathbf{r}_\perp \, |\phi(\mathbf{r}_\perp, t) - \langle\phi(t)\rangle| n(\mathbf{r}_\perp, t)}{\int \mathrm{d}^2\mathbf{r}_\perp \, n(\mathbf{r}_\perp, t)}, \tag{6.1}$$

which measures the local deviation of the condensate phase ϕ from the average phase $\langle\phi(t)\rangle = 1/N \cdot \int \mathrm{d}^2\mathbf{r}_\perp \, n(\mathbf{r}_\perp, t)\phi(\mathbf{r}_\perp, t)$, with an appropriate branch choice for ϕ [26]. A lack of phase coherence is indicated by $\mathcal{P} \to 0$, whereas a supersolid is subject to $\mathcal{P} \sim 1$. Secondly, to further the understanding of the defect relaxation process in the droplet phase, it is insightful to identify if the relaxation process is driven by the movement of droplets or by inter-droplet particle exchange. The former case is characterized by correlation of droplet positions and positions of large phase gradients, as the velocity field in a superfluid is given by the gradient of the phase, see Sec. 3.3. In the latter case, phase gradients will be high in regions of low density between the droplets. Therefore, we propose the measure

$$\mathcal{M}(t) = \frac{\int \mathrm{d}^2\mathbf{r}_\perp \, |\nabla\phi(\mathbf{r}_\perp, t)| n(\mathbf{r}_\perp, t)}{\left(\int \mathrm{d}^2\mathbf{r}_\perp \, |\nabla\phi(\mathbf{r}_\perp, t)|\right) \cdot \left(\int \mathrm{d}^2\mathbf{r}_\perp \, n(\mathbf{r}_\perp, t)\right)}. \tag{6.2}$$

This measure has the following clear interpretation. If condensate flow is on average the same in high-density regions as elsewhere, then $\mathcal{M} = 1$. However, if particle flow is enhanced in droplets, i.e. the relaxation process is driven by the redistribution of droplets, then $\mathcal{M} > 1$, whereas inter-droplet particle exchange is characterized by $\mathcal{M} < 1$.

Thirdly, another aspect of hexatic systems can be analyzed. This thesis has focused on angular correlations. However, hexatic systems also display short-ranged orientational order, i.e. $g_{\mathbf{G}}(r = |\mathbf{r}_i - \mathbf{r}_j|) = \langle e^{i\mathbf{G}[\mathbf{u}(\mathbf{r}_i) - \mathbf{u}(\mathbf{r}_j)]} \rangle \propto e^{-r/\xi_{\mathbf{G}}}$ [72, 74]. Here, $\mathbf{G}$ denotes a reciprocal lattice vector, $\xi_{\mathbf{G}}$ the translational correlation length and $\mathbf{u}(\mathbf{r})$ the displacement field, i.e. the deviation of droplet positions from their expected positions in a perfect lattice in the droplet phase and analogously the deviation of density minima positions from their expected positions in the honeycomb phase. Extracting the translational correlation function will help to further understand the hexatic nature of the systems at hand.

Fourthly, it might be insightful to redo above analysis under variations of the system size. Although periodic boundary conditions minimize finite size effects, some features of the defect decay still depend on the system size. Increasing the simulated grid yields access to $g_6(r)$ over a larger domain, decreasing the influence of short-ranged fluctuations to the $g_6 \propto r^{-\eta_6}$ fit. The influence of finite size effects may also be suppressed by decreasing the bin size $\mathrm{d}r$ in the computation of g_6, thus increasing the number of data points included in the fit. Additionally, the total number of initial lattice defects is proportional to the area of the condensate, whereas global grain boundaries result in a number of defects proportional to the number of unit cells along the shorter dimension, thus scaling linearly with L_x. Simulating the condensate over larger domains could therefore help to determine the decay coefficients more easily in the $N_D(t) \propto (t - t^*)^\alpha$ fits.

Finally, should experiments ever realize 2D supersolids in the droplet or honeycomb phase

over as large domains as analyzed in this thesis and investigate the lattice formation process, they will not be able to reproduce the quasi 2D approach of this thesis exactly. In nature, the underlying physics described by the eGPE is realized in three dimensions. Although computationally expensive, it might thus be useful to compare the results of this thesis to results of full three-dimensional (3D) simulations and redo the lattice formation analysis on particle area densities obtained by either integrating the 3D particle volume densities along the trapping direction or considering 2D slices of the particle volume density perpendicular to the trapping direction. This will show whether or not reducing the effective dimensionality of the system influences the scaling coefficients and could serve to validate the obtained results.

7 Acknowledgments

We happily acknowledge support by the state of Baden-Württemberg through bwHPC and the German Research Foundation (DFG) through grant INST 35/1597-1 FUGG. This project relies heavily on the use of numerical methods and would not have been feasible without access to the resources provided by bwHPC.
A further resource integral to this work is MathWorks software package MATLAB, where a student license has been provided via Heidelberg University through a Baden-Württemberg Landeslizenz. We used additional MATLAB functionality regarding colormaps provided by [77] in the generation of the figures Fig. 3.1, Fig. 3.2, Fig. 3.3, Fig. 4.5, and Fig. C.1.
Another important software package to this thesis is the typesetting system LaTeX, which we used to write and format this document.
We thank W. Kirkby, A. Oros, N. Rasch, and T. Gasenzer for fruitful discussions and valuable insights on quench dynamics in 2D dipolar Bose gases. W. Kirkby in particular has been a constant source of inspiration, and he has provided the split-step Fourier method eGPE solver we adapted to generate the data analyzed in this work.
Throughout this thesis, we have used the pronoun 'we' to refer to the collective readers and the author. However, we want to clarify that all results and methods presented have been obtained by L. Schulz, unless otherwise explicitly specified in the References or Acknowledgments sections.

All these formal acknowledgments aside, I wish to extend my personal gratitude towards several people.
Wyatt, thank you for being a patient supervisor and for always answering my questions. I have enjoyed our meetings, and you have taught me a lot.
Susanne, Roland, and Jakob, thank you for your linguistic and stylistic advice.
Finally, I want to thank my parents for always encouraging and supporting me in my academic pursuits.

References

[1] S. N. Bose, Plancks Gesetz und Lichtquantenhypothese, Z. Phys. **26**, 178-181 (1924) (cit. on p. 1)

[2] A. Einstein, Quantentheorie des einatomigen idealen Gases, via Universität Münster, Sitzungsberichte der Preussischen Akademie der Wissenschaften, Physikalisch-mathematische Klasse, 261-267 (1924) (cit. on pp. 1, 2)

[3] A. Einstein, Quantentheorie des einatomigen idealen Gases, via Universität Münster, Sitzungsberichte der Preussischen Akademie der Wissenschaften, Physikalisch-mathematische Klasse, 3-14 (1925) (cit. on p. 1)

[4] F. London, On the Bose-Einstein Condensation, Phys. Rev. **54**(11), 947-954 (1938) (cit. on p. 1)

[5] L. N. Cooper, Bound Electron Pairs in a Degenerate Fermi Gas, Phys. Rev. **104**(4), 1189-1190 (1956) (cit. on p. 1)

[6] S. Das and R. K. Bhaduri, Bose-Einstein condensate in cosmology, arXiv:1808.10505v3 [gr-qc] (2018) (cit. on p. 1)

[7] C. J. Pethick and H. Smith, Bose-Einstein Condensation in dilute Gases, Cambridge University Press, England, 10.1017/CBO978-0-51-175558-3 (2001), (cit. on pp. 1, 3, 4, 5, 16, 21, 38)

[8] S. Chu, L. Hollberg, J. E. Bjorkholm, A. Cable, and A. Ashkin, Three-dimensional viscous confinement and cooling of atoms by resonance radiation pressure, Phys. Rev. Lett. **55**(1), 48-53 (1985) (cit. on p. 1)

[9] P. D. Lett, R. N. Watts, C. I. Westbrook, W. D. Phillips, P. L. Gould, and H. J. Metcalf, Observation of Atoms Laser Cooled below the Doppler Limit, Phys. Rev. Lett. **61**(2), 169-173 (1988) (cit. on p. 1)

[10] A. Aspect, E. Arimondo, R. Kaiser, N. Vansteenkiste, and C. Cohen-Tannoudji, Laser Cooling below the One-Photon Recoil Energy by Velocity-Selective Coherent Population Trapping, Phys. Rev. Lett. **61**(7), 826-829 (1988) (cit. on p. 1)

[11] K. B. Davis, M.-O. Mewes, M. R. Andrews, N. J. van Druten, D. S. Durfee, D. M. Kurn, and W. Ketterle, Bose-Einstein Condensation in a Gas of Sodium Atoms, Phys. Rev. Lett. **75**(22), 3969-3974 (1995) (cit. on pp. 1, 4, 9)

[12] M. H. Anderson, J. R. Ensher, M. R. Matthews, C. E. Wieman, and E. A. Cornell, Observation of Bose-Einstein Condensation in a Dilute Atomic Vapor, Science **269**(5221), 198-201 (1995) (cit. on pp. 1, 9)

[13] C. C. Bradley, C. A. Sackett, J. J. Tollett, and R. G. Hulet, Evidence of Bose-Einstein Condensation in an Atomic Gas with Attractive Interactions, Phys. Rev. Lett. **75**(9), 1687-1691 (1995) (cit. on pp. 1, 9)

[14] C. C. Bradley, C. A. Sackett, J. J. Tollett, and R. G. Hulet, Evidence of Bose-Einstein Condensation in an Atomic Gas with Attractive Interactions, Phys. Rev. Lett. **79**(6), 1170 (1997) (cit. on pp. 1, 9)

[15] Advanced information, NobelPrize.org, Nobel Prize Outreach 2025. Thu. 9 Oct 2025 (2025) (cit. on p. 1)

[16] Advanced information, NobelPrize.org, Nobel Prize Outreach 2025. Thu. 9 Oct 2025 (2025) (cit. on p. 1)

[17] L. Chomaz, I. Ferrier-Barbut, F. Ferlaino, B. Laburthe-Tolra, B. L. Lev, and T. Pfau, Dipolar physics: a review of experiments with magnetic quantum gases, Rep. Prog. Phys. **86**(2), 026401 (2023) (cit. on pp. 1, 4, 5, 9, 19)

[18] W. Kirkby, H. Salman, T. Gasenzer, and L. Chomaz, Kibble-Zurek scaling of the superfluid-supersolid transition in an elongated dipolar gas, arXiv:2411.18395 [cond-mat.quant-gas] (2024) (cit. on pp. 1, 5, 19)

[19] N. Rasch, L. Chomaz, and T. Gasenzer, Anomalous non-thermal fixed point in a quasi-two-dimensional dipolar Bose gas, arXiv:2506.01653 [cond-mat.quant-gas] (2025) (cit. on pp. 1, 19, 33, 65)

[20] M. Karl and T. Gasenzer, Strongly anomalous non-thermal fixed point in a quenched two-dimensional Bose gas, arXiv:1611.01163v3 [cond-mat.quant-gas] (2016) (cit. on pp. 1, 65)

[21] R. N. Bisset, R. M. Wilson, D. Baillie, and P. B. Blakie, Ground-state phase diagram of a dipolar condensate with quantum fluctuations, Phys. Rev. A **94**(3), 033619 (2016) (cit. on pp. 1, 5, 9, 15)

[22] B. T. E. Ripley, D. Baillie, and P. B. Blakie, Two-dimensional supersolidity in a planar dipolar Bose gas, arXiv:2308.16416 [cond-mat.quant-gas] (2023) (cit. on pp. 1, 5, 9, 10, 11, 15, 19, 43)

[23] A. Minguzzia, S. Succib, F. Toschib, M.P. Tosia, and P. Vignolo, Numerical methods for atomic quantum gases with applications to Bose–Einstein condensates and to ultracold fermions, Phys. Rep. **395**(4-5), 223-355 (2004) (cit. on pp. 1, 12, 13)

[24] L. Fioroni, L. Gravina, J. Stefaniak, A. Baumgärtner, F. Finger, D. Dreon, and T. Donner, A Python GPU-accelerated solver for the Gross-Pitaevskii equation and applications to many-body cavity QED, arXiv:2404.14401v3 [physics.comp-ph] (2024) (cit. on pp. 1, 13, 14)

[25] A. del Campo, F. J. Gómez-Ruiz, and H.-Q. Zhang, Locality of spontaneous symmetry breaking and universal spacing distribution of topological defects formed across a phase transition, Phys. Rev. B **106**(14), L140101 (2022) (cit. on pp. 1, 39, 42)

[26] W. Kirkby, T. Bland, F. Ferlaino, and R. N. Bisset, Spin rotons and supersolids in binary antidipolar condensates, arXiv:2301.08007v3 [cond-mat.quant-gas] (2023) (cit. on pp. 1, 45)

[27] E. H. Lieb, R. Seiringer, and J. Yngvason, Superfluidity in dilute trapped Bose gases, Phys. Rev. B **66**(13), 134529 (2002) (cit. on p. 1)

[28] C. F. Barenghi and N. G. Parker, A primer on quantum fluids, arXiv:1605.09580v2 [cond-mat.quant-gas] (2016) (cit. on pp. 1, 2, 3, 5, 13, 16)

[29] J. F. Allen and A. D. Misener, Flow of Liquid Helium II, Nature **141**(3558), 75 (1938) (cit. on p. 1)

[30] P. Kapitza, Viscosity of Liquid Helium below the λ-Point, Nature **141**(3558), 74 (1938) (cit. on p. 1)

[31] L. Landau, Theory of the Superfluidity of Helium II, Phys. Rev. **60**(4), 356-358 (1941) (cit. on pp. 1, 43)

[32] N. Bogolubov, ON THE THEORY OF SUPERFLUIDITY, Journal of Physics **11**, 23-33 (1947) (cit. on p. 1)

[33] M. R. Matthews, B. P. Anderson, P. C. Haljan, D. S. Hall, C. E. Wieman, and E. A. Cornell, Vortices in a Bose-Einstein Condensate, Phys. Rev. Lett. **83**(13), 2498-2501 (1999) (cit. on pp. 1, 4)

[34] A. J. Leggett, Superfluidity, Rev. Mod. Phys. **71**(2), S318 (1999) (cit. on pp. 1, 16)

[35] D. J. Thouless, The flow of a dense superfluid, Annals of Physics **52**(3), 403-427 (1969) (cit. on pp. 1, 4, 17)

[36] A. F. Andreev and I. M. Lifshitz, Quantum theory of defects in crystals, Sov. Phys. JETP. **29**, 1107–1113 (1969) (cit. on p. 1)

[37] E. Kim and M. H. W. Chan, Probable observation of a supersolid helium phase, Nature **427**(6971), 225–227 (2004) (cit. on p. 2)

[38] D. Y. Kim and M. H. W. Chan, Absence of Supersolidity in Solid Helium in Porous Vycor Glass, Phys. Rev. Lett. **109**(15), 155301 (2012) (cit. on p. 2)

[39] J. R. Li, J. Lee, W. Huang, S. Burchesky, B. Shteynas, F. Ç. Top, A. O. Jamison, and W. Ketterle, A stripe phase with supersolid properties in spin–orbit-coupled Bose–Einstein condensates, Nature **543**(7643), 91–94 (2017) (cit. on pp. 2, 4)

[40] J. Léonard, A. Morales, P. Zupancic, T. Esslinger, and T. Donner, Supersolid formation in a quantum gas breaking continuous translational symmetry, arXiv:1609.09053v1 [cond-mat.quant-gas] (2017) (cit. on pp. 2, 9)

[41] E. Casotti, E. Poli, L. Klaus, A. Litvinov, C. Ulm, C. Politi, M. J. Mark, T. Bland, and F. Ferlaino, Observation of vortices in a dipolar supersolid, arXiv:2403.18510v2 [cond-mat.quant-gas] (2024) (cit. on pp. 2, 5, 9, 11, 19, 42)

[42] B. Riemann, Über die Anzahl der Primzahlen unter einer gegebenen Größe, via Akademiebibliothek der Berlin-Brandenburgischen Akademie der Wissenschaften, Monatsberichte der Preussischen Akademie der Wissenschaften, Gesamtsitzung, 671-680 (2023) (cit. on p. 3)

[43] M. E. Peskin and D. V. Schroeder, An Introduction to Quantum Field Theory, CRC Press, USA, 10.1201/9780429503559 (1995), (cit. on pp. 3, 15, 54)

[44] K. Goral, K. Rzazewski, and T. Pfau, Bose-Einstein condensation with magnetic dipole-dipole forces, arXiv:cond-mat/9907308v2 (2000) (cit. on pp. 5, 7, 13)

[45] K. Huang and C. N. Yang, Quantum-Mechanical Many-Body Problem with Hard-Sphere Interaction, Phys. Rev. **105**(3), 767-775 (1957) (cit. on p. 5)

[46] T. D. Lee, K. Huang, and C. N. Yang, Eigenvalues and Eigenfunctions of a Bose System of Hard Spheres and Its Low-Temperature Properties, Phys. Rev. **106**(6), 1135-1145 (1957) (cit. on p. 5)

[47] P. Pedri and L. Santos, Two-Dimensional Bright Solitons in Dipolar Bose-Einstein Condensate, Phys. Rev. Lett. **95**(20), 200404 (2005) (cit. on pp. 5, 57)

[48] R. N. Bisset, Theoretical Study of the Trapped Dipolar Bose Gas in the Ultra-Cold Regime, University of Otago (2013) (cit. on pp. 7, 9)

[49] A. Griesmaier, J. Werner, S. Hensler, J. Stuhler, and T. Pfau, Bose-Einstein Condensation of Chromium, Phys. Rev. Lett. **94**(16), 160401 (2005) (cit. on p. 8)

[50] S. Hensler, J. Werner, A. Griesmaier, P. O. Schmidt, A. Goerlitz, T. Pfau, S. Giovanazzi, and K. Rzazewski, Dipolar Relaxation in an ultra-cold Gas of magnetically trapped chromium atoms, arXiv:quant-ph/0307184 (2003) (cit. on p. 8)

[51] Y. Takasu, K. Maki, K. Komori, T. Takano, K. Honda, M. Kumakura, T. Yabuzaki, and Y. Takahashi, Spin-Singlet Bose-Einstein Condensation of Two-Electron Atoms, Phys. Rev. Lett. **91**(4), 040404 (2003) (cit. on p. 9)

[52] M. Lu, N. Q. Burdick, S. H. Youn, and B. L. Lev, Strongly Dipolar Bose-Einstein Condensate of Dysprosium, Phys. Rev. Lett. **107**(19), 190401 (2011) (cit. on pp. 9, 19)

[53] K. Aikawa, A. Frisch, M. Mark, S. Baier, A. Rietzler, R. Grimm, and F. Ferlaino, Bose-Einstein Condensation of Erbium, Phys. Rev. Lett. **108**(21), 210401 (2012) (cit. on p. 9)

[54] E. T. Davletov, V. V. Tsyganok, V. A. Khlebnikov, D. A. Pershin, D. V. Shaykin, and A. V. Akimov, Machine learning for achieving Bose-Einstein condensation of thulium atoms, Phys. Rev. A **102**(1), 011302(R) (2020) (cit. on p. 9)

[55] Y. Miyazawa, R. Inoue, H. Matsui, G. Nomura, and M. Kozuma, Bose-Einstein Condensation of Europium, Phys. Rev. Lett. **129**(22), 223401 (2022) (cit. on p. 9)

[56] Y. Tang, N. Q. Burdick, K. Baumann, and B. L. Lev, Bose–Einstein condensation of ^{162}Dy and ^{160}Dy, New J. Phys. **17**(4), 045006 (2015) (cit. on p. 9)

[57] L. Tanzi, E. Lucioni, F. Famà, J. Catani, A. Fioretti, C. Gabbanini, R. N. Bisset, L. Santos, and G. Modugno, Observation of a Dipolar Quantum Gas with Metastable Supersolid Properties, Phys. Rev. Lett. **122**(13), 130405 (2019) (cit. on p. 9)

[58] F. Böttcher, J.-N. Schmidt, M. Wenzel, J. Hertkorn, M. Guo, T. Langen, and T. Pfau, Transient Supersolid Properties in an Array of Dipolar Quantum Droplets, Phys. Rev. X **9**(1), 011051 (2019) (cit. on p. 9)

[59] L. Chomaz et al., Long-Lived and Transient Supersolid Behaviors in Dipolar Quantum Gase, Phys. Rev. X **9**(2), 021012 (2019) (cit. on pp. 9, 19)

[60] T. Bland, E. Poli, C. Politi, L. Klaus, M. A. Norcia, F. Ferlaino, L. Santos, and R. N. Bisset, Two-Dimensional Supersolid Formation in Dipolar Condensates, arXiv:2107.06680v2 [cond-mat.quant-gas] (2022) (cit. on pp. 9, 10, 19)

[61] L. Chomaz, S. Baier, D. Petter, M. J. Mark, F. Wächtler, L. Santos, and F. Ferlaino, Quantum-Fluctuation-Driven Crossover from a Dilute Bose-Einstein Condensate to a Macrodroplet in a Dipolar Quantum Fluid, Phys. Rev. X **6**(4), 041039 (2016) (cit. on p. 9)

[62] A. Trautmann, P. Ilzhöfer, G. Durastante, C. Politi, M. Sohmen, M. J. Mark, and F. Ferlaino, Dipolar Quantum Mixtures of Erbium and Dysprosium Atoms, arXiv:1807.07555 [cond-mat.quant-gas] (2018) (cit. on p. 9)

[63] T. Weber, J. Herbig, M. Mark, H.-C. Nägerl, and R. Grimm, Bose-Einstein Condensation of Cesium, Science **299**(5604), 232-235 (2003) (cit. on p. 9)

[64] G. Roati, M. Zaccanti, C. D'Errico, J. Catani, M. Modugno, A. Simoni, M. Inguscio, and G. Modugno, ^{39}K Bose-Einstein condensate with tunable interactions, Phys. Rev. Lett. **99**(1), 010403 (2007) (cit. on p. 9)

[65] P. B. Blakie, Superfluid fraction tensor of a two-dimensional supersolid, arXiv:2308.14001v1 [cond-mat.quant-gas] (2023) (cit. on p. 11)

[66] W. J. Cody, Performance evaluation of programs for the error and complementary error functions, ACM Trans. Math. Softw. **16**(1), 29-37 (1990) (cit. on p. 13)

[67] M. Thudiyangal and A. del Campo, Universal Vortex Statistics and Stochastic Geometry of Bose-Einstein Condensation, arXiv:2401.09525v1 [cond-mat.quant-gas] (2024) (cit. on pp. 18, 39, 42)

[68] P. B. Blakie, A. S. Bradley, M. J. Davis, R. J. Ballagh, and C. W. Gardiner, Dynamics and statistical mechanics of ultra-cold Bose gases using c-field techniques, arXiv:0809.1487 [cond-mat.stat-mech] (2008) (cit. on p. 21)

[69] M. Gazo, A. Karailiev, T. Satoor, C. Eigen, M. Gałka, and Z. Hadzibabic, Universal Coarsening in a Homogeneous Two-Dimensional Bose Gas, arXiv:2312.09248v2 [cond-mat.quant-gas] (2024) (cit. on p. 25)

[70] B. Efron, Bootstrap Methods: Another Look at the Jackknife, Ann. Statist. **7**(1), 1-26 (1979) (cit. on p. 25)

[71] V. Blobel and E. Lohrmann, Statistische und numerische Methoden der Datenanalyse, chapter 7, Vieweg+Teubner Verlag Wiesbaden, Germany, 10.1007/978-3-663-05690-4 (2013), (cit. on p. 27)

[72] K. J. Strandburg, Two-dimensional melting, Rev. Mod. Phys. **60**(1), 161-207 (1988) (cit. on pp. 28, 31, 33, 34, 45)

[73] R. P. A. Dullens, M. C. D. Mourad, D. G. A. L. Aarts, J. P. Hoogenboom, and W. K. Kegel, Shape-Induced Frustration of Hexagonal Order in Polyhedral Colloids, Phys. Rev. Lett. **96**(2), 028304 (2006) (cit. on p. 30)

[74] R. Gruber et al., Real-time observation of topological defect dynamics mediating two-dimensional skyrmion lattice melting, Nature Nanotechnology **1748**(3395) (2025) (cit. on pp. 30, 45)

[75] K. J. Strandburg, J. A. Zollweg, and G. V. Chester, Bond-angular order in two-dimensional Lennard-Jones and hard-disk systems, Phys. Rev. B **30**(5), 2755-2759 (1984) (cit. on pp. 32, 33)

[76] A. M. Mathai, An Introduction to Geometrical Probability: Distributional Aspects with Applications, Vol. 1, section 2.4, CRC Press, USA (1999), (cit. on p. 41)

[77] A. Biguri, Perceptually uniform colormaps, MATLAB Central File Exchange (2025) (cit. on p. 46)

[78] R. Oloff, Wahrscheinlichkeitsrechnung und Maßtheorie, section 7.11, Springer Spektrum Berlin, Heidelberg, Germany, 10.1007/978-3-662-53024-5 (2017), (cit. on p. 53)

[79] I. S. Gradshteyn and I. M. Ryzhik, Table of integrals, series, and products, 6$^{\text{th}}$ edition, section 8.25, Academic Press, USA, 10.1016/B978-0-12-294757-5 (2000), (cit. on p. 57)

[80] H. F. Baker, Alternants and Continuous Groups, Proceedings of the London Mathematical Society **2**(3), 24-27 (1905) (cit. on p. 59)

[81] O. Forster and F. Lindemann, Analysis 1, 13$^{\text{th}}$ edition, section 20.6, Springer Spektrum Wiesbaden, Germany, 10.1007/978-3-658-40130-6 (2023), (cit. on p. 65)

Appendix

A A standard integral in statistical physics

Here, we want to present an evaluation of the integral

$$I = \int_0^\infty \mathrm{d}E \, \frac{E^{1/2}}{e^{(E-\mu)/k_BT} - 1}. \tag{A.1}$$

If we introduce $x = E/k_BT$ and $z = e^{\mu/k_BT}$, then

$$I = (k_BT)^{3/2} \int_0^\infty \mathrm{d}x \, \frac{x^{1/2}}{e^x/z - 1}. \tag{A.2}$$

Now we recognize the geometric series,

$$\frac{1}{e^x/z - 1} = \frac{ze^{-x}}{1 - ze^{-x}} = \frac{1 + ze^{-x} - 1}{1 - ze^{-x}} = -1 + \frac{1}{1 - ze^{-x}} = -1 + \sum_{k=0}^{\infty} \left(ze^{-x}\right)^k = \sum_{k=1}^{\infty} \left(ze^{-x}\right)^k, \tag{A.3}$$

where convergence at finite energy is ensured by $|ze^{-x}| = \left|e^{(\mu-E)/k_BT}\right| \leq 1$ as $\mu \leq 0$. Otherwise, the Bose-Einstein distribution Eq. (2.3) would not be positive, as required. This casts I into the form

$$I = (k_BT)^{3/2} \int_0^\infty \mathrm{d}x \, x^{1/2} \sum_{k=1}^{\infty} (ze^{-x})^k, \tag{A.4}$$

which, by using the Fubini-Tonelli theorem [78], may be written as[9]

$$I = (k_BT)^{3/2} \sum_{k=1}^{\infty} z^k \int_0^\infty \mathrm{d}x \, x^{1/2} e^{-kx}. \tag{A.5}$$

Finally, by means of partial integration and substitution, we can express I as

$$\begin{aligned} I &= (k_BT)^{3/2} \sum_{k=1}^{\infty} z^k \left[\underbrace{\frac{\sqrt{x}}{-k} e^{-kx} \Big|_0^\infty}_{=0} - \int_0^\infty \mathrm{d}x \frac{1}{-2k} \frac{1}{\sqrt{x}} e^{-kx} \right] \\ &\overset{u=\sqrt{kx}}{=} (k_BT)^{3/2} \sum_{k=1}^{\infty} z^k \int_0^\infty \frac{\mathrm{d}u}{k^{3/2}} e^{-u^2} = (k_BT)^{3/2} \sum_{k=1}^{\infty} z^k \frac{\sqrt{\pi}}{2k^{3/2}}. \end{aligned} \tag{A.6}$$

[9] We have $I \propto \int_0^\infty \mathrm{d}x \sum_{k=1}^{\infty} x^{1/2} \left(ze^{-x}\right)^k \equiv \int_0^\infty \mathrm{d}x \sum_{k=1}^{\infty} f_k(x)$. Since all $f_k(x)$ are non-negative functions for all x, k in the relevant domain, $x \geq 0$, $k > 0$, and since all f_k are smooth measurable functions dominated by the integrable function $|f_k(x)| \leq g(x) = x^{1/2}e^{-x}$, which obeys $\int_0^\infty \mathrm{d}x \, x^{1/2}e^{-x} = \Gamma(3/2) = \sqrt{\pi}/2 < \infty$, the theorem applies.

This integral (dropping factors of k_BT from the $x = E/k_BT$ substitution) is a special case of the more general

$$I(\alpha) = \int_0^\infty \mathrm{d}x \frac{x^\alpha}{e^x/z - 1}, \tag{A.7}$$

which, by the same calculation as above, may be brought into the form

$$I(\alpha) = \sum_{k=1}^{\infty} z^k \int_0^\infty \mathrm{d}x\, x^\alpha e^{-kx}. \tag{A.8}$$

Introducing the substitution $t = kx$, we have

$$I(\alpha) = \sum_{k=1}^{\infty} z^k \int_0^\infty \frac{\mathrm{d}t}{k} \left(\frac{t}{k}\right)^\alpha e^{-t} = \sum_{k=1}^{\infty} \frac{z^k}{k^{\alpha+1}} \Gamma(\alpha+1) \tag{A.9}$$

by definition of the gamma function [43]. If we set $\alpha = 1/2$, and recognize $\Gamma(3/2) = \sqrt{\pi}/2$, we recover the result of Eq. (A.6).

B Derivation of the 2D eGPE

In this section, we want to explicitly show the steps necessary to arrive at the 2D eGPE Eq. (2.17). Starting from Eq. (2.11) and inserting the separated spatial wavefunction Eq. (2.13), we arrive at

$$\begin{aligned} i\hbar \frac{\partial \psi(x,y,t)}{\partial t}\varphi(z) = \Big\{ &-\frac{\hbar^2}{2m}\nabla^2 + \frac{m}{2}\omega_z^2 z^2 + g_s \left|\psi(x,y,t)\varphi(z)\right|^2 + \gamma_{QF}\left|\psi(x,y,t)\varphi(z)\right|^3 \\ &+ \int \mathrm{d}^3\mathbf{r}' U_{dd}(\mathbf{r}-\mathbf{r}') \left|\psi(x',y',t)\varphi(z')\right|^2 \Big\} \psi(x,y,t)\varphi(z), \end{aligned} \tag{B.1}$$

assuming a constant wavefunction in z-direction, $\partial\varphi(z,t)/\partial t = 0$, i.e. $\varphi(z,t) = \varphi(z)$. We proceed by multiplying this equation by $\varphi^*(z)$ and integrating over z term by term. Then the LHS reads

$$i\hbar \frac{\partial \psi(x,y,t)}{\partial t} \int \mathrm{d}z \left|\varphi(z)\right|^2 \overset{Eq.\ (2.15)}{=} i\hbar \frac{\partial \psi(x,y,t)}{\partial t}. \tag{B.2}$$

For the kinetic term, we have

$$\begin{aligned} &-\frac{\hbar^2}{2m}\int \mathrm{d}z\, \varphi^*(z)\nabla^2 \left[\psi(x,y,t)\varphi(z)\right] \\ &= -\frac{\hbar^2}{2m}\int \mathrm{d}z \left[\left(\frac{\partial^2}{\partial x^2} + \frac{\partial^2}{\partial y^2}\right)\psi(x,y,t)\left|\varphi(z)\right|^2 + \psi(x,y,t)\varphi^*(z)\frac{\partial^2}{\partial z^2}\varphi(z)\right], \end{aligned} \tag{B.3}$$

and using Eq. (2.14), the second derivative of $\varphi(z)$ can be evaluated explicitly

$$\begin{aligned}\frac{\partial^2}{\partial z^2}\varphi(z) &= \frac{1}{\sqrt{l_z}\pi^{1/4}}\frac{\partial^2}{\partial z^2}\exp\left\{-\frac{1}{2}\frac{z^2}{l_z^2}\right\} \\ &= -\frac{\partial}{\partial z}\left[\frac{z}{l_z^2}\varphi(z)\right] = \left[-\frac{1}{l_z^2}+\frac{z^2}{l_z^4}\right]\varphi(z),\end{aligned} \tag{B.4}$$

so the kinetic term can be expressed as

$$\begin{aligned}&-\frac{\hbar^2}{2m}\int \mathrm{d}z\,\varphi^*(z)\nabla^2\left[\psi(x,y,t)\varphi(z)\right] \\ &= -\frac{\hbar^2}{2m}\left\{\left(\frac{\partial^2}{\partial x^2}+\frac{\partial^2}{\partial y^2}\right)-\frac{1}{l_z^2}+\frac{1}{l_z\sqrt{\pi}}\int \mathrm{d}z\frac{z^2}{l_z^4}\exp\left\{-\frac{z^2}{l_z^2}\right\}\right\}\psi(x,y,t) \\ &= -\frac{\hbar^2}{2m}\left\{\left(\frac{\partial^2}{\partial x^2}+\frac{\partial^2}{\partial y^2}\right)-\frac{1}{2l_z^2}\right\}\psi(x,y,t)\end{aligned} \tag{B.5}$$

by evaluating the standard second moment Gaussian integral[10] and using the normalization condition Eq. (2.15). The same integral appears in the potential term,

$$\frac{m}{2}\omega_z^2\left\{\int \mathrm{d}z\,z^2\left|\varphi(z)\right|^2\right\}\psi(x,y,t) = \frac{m}{2}\omega_z^2\frac{l_z^2}{2}\psi(x,y,t). \tag{B.6}$$

The contact interaction and quantum fluctuation terms involve integrals over powers of the absolute value of $\varphi(z)$,

$$\begin{aligned}\int \mathrm{d}z\left|\varphi(z)\right|^n &= \left(\frac{1}{\sqrt{l_z}\pi^{1/4}}\right)^n\int \mathrm{d}z\exp\left\{-\frac{n}{2}\frac{z^2}{l_z^2}\right\} \\ \overset{u=\sqrt{n}z}{=} &\left(\frac{1}{\sqrt{l_z}\pi^{1/4}}\right)^n\frac{1}{\sqrt{n}}\int \mathrm{d}u\exp\left\{-\frac{1}{2}\frac{u^2}{l_z^2}\right\} = \left(\frac{1}{\sqrt{l_z}\pi^{1/4}}\right)^n\sqrt{\frac{2\pi}{n}}l_z.\end{aligned} \tag{B.7}$$

This yields

$$g_s\left\{\int \mathrm{d}z\left|\varphi(z)\right|^4\right\}\left|\psi(x,y,t)\right|^2\psi(x,y,t) = \frac{g_s}{\sqrt{2\pi}l_z}\left|\psi(x,y,t)\right|^2\psi(x,y,t) \tag{B.8}$$

and

$$\gamma_{QF}\left\{\int \mathrm{d}z\left|\varphi(z)\right|^5\right\}\left|\psi(x,y,t)\right|^3\psi(x,y,t) = \sqrt{\frac{2}{5}}\frac{\gamma_{QF}}{\pi^{3/4}l_z^{3/2}}\left|\psi(x,y,t)\right|^3\psi(x,y,t), \tag{B.9}$$

---

[10] $\frac{1}{l_z\sqrt{\pi}}\int_{-\infty}^{\infty}\mathrm{d}z\,\frac{z^2}{l_z^4}e^{-\frac{z^2}{l_z^2}} \overset{u=z/l_x}{=} \frac{1}{l_z^2\sqrt{\pi}}\int_{-\infty}^{\infty}\mathrm{d}u\,u\cdot ue^{-u^2} \overset{\text{P. I.}}{=} \frac{1}{l_z^2\sqrt{\pi}}\left[\underbrace{-\frac{1}{2}ue^{-u^2}\Big|_{-\infty}^{\infty}}_{=0}-\int_{-\infty}^{\infty}\mathrm{d}u\left(-\frac{1}{2}e^{-u^2}\right)\right]$
$= \frac{1}{2l_z^2}\cdot\frac{1}{\sqrt{\pi}}\int_{-\infty}^{\infty}\mathrm{d}u\,e^{-u^2} = \frac{1}{2l_z^2}$

respectively. Finally, we have to consider the DDI term. Inserting

$$(x-x')^2+(y-y')^2 \equiv |\mathbf{r}_\perp-\mathbf{r}'_\perp|^2 \tag{B.10}$$

and

$$\cos\theta = \frac{z-z'}{\sqrt{|\mathbf{r}_\perp-\mathbf{r}'_\perp|^2+(z-z')^2}} \tag{B.11}$$

into the expression for the DDI potential, it reads

$$U_{dd}(\mathbf{r}-\mathbf{r}') = \frac{\mu_0\mu_m^2}{4\pi}\frac{|\mathbf{r}_\perp-\mathbf{r}'_\perp|^2-2(z-z')^2}{\left[|\mathbf{r}_\perp-\mathbf{r}'_\perp|^2+(z-z')^2\right]^{5/2}}. \tag{B.12}$$

After multiplying the eGPE with $\varphi^*(z)$ and integrating along z, the DDI can be described by

$$\begin{aligned}&\int \mathrm{d}^2\mathbf{r}'_\perp \int \mathrm{d}z'\mathrm{d}z \frac{\mu_0\mu_m^2}{4\pi}\frac{|\mathbf{r}_\perp-\mathbf{r}'_\perp|^2-2(z-z')^2}{\left[|\mathbf{r}_\perp-\mathbf{r}'_\perp|^2+(z-z')^2\right]^{5/2}}|\psi(\mathbf{r}'_\perp,t)|^2|\varphi(z')|^2|\varphi(z)|^2\psi(\mathbf{r}_\perp,t)\\ &\quad=\int \mathrm{d}^2\mathbf{r}'_\perp\int \mathrm{d}u\, U_{dd}(\mathbf{r}_\perp-\mathbf{r}'_\perp,u)\left(|\varphi|^2*|\varphi|^2\right)(u)|\psi(\mathbf{r}'_\perp,t)|^2\psi(\mathbf{r}_\perp,t).\end{aligned} \tag{B.13}$$

Here we have shifted the z' integral by $u=z-z'$. The appearing convolution is straightforward to evaluate using the explicit form of $\varphi(z)$ as in Eq. (2.14),

$$\left(|\varphi|^2*|\varphi|^2\right)(u) = \frac{1}{\pi l_z^2}\int \mathrm{d}w\, e^{-\frac{w^2}{l_z^2}}e^{-\frac{(w-u)^2}{l_z^2}} = \frac{e^{-\frac{u^2}{l_z^2}}}{\pi l_z^2}\int \mathrm{d}w \exp\left\{-2\frac{w^2}{l_z^2}+2\frac{uw}{l_z^2}\right\} = \frac{e^{-\frac{1}{2}\frac{u^2}{l_z^2}}}{\sqrt{2\pi}l_z}, \tag{B.14}$$

so the dipolar interaction term reads

$$\begin{aligned}&\int \mathrm{d}^2\mathbf{r}'_\perp\int \mathrm{d}u\, U(\mathbf{r}_\perp-\mathbf{r}'_\perp,u)\left(|\varphi|^2*|\varphi|^2\right)(u)|\psi(\mathbf{r}'_\perp,t)|^2\psi(\mathbf{r}_\perp,t)\\ &\quad=\int \mathrm{d}^2\mathbf{r}'_\perp U_{dd}^{2D}(\mathbf{r}_\perp-\mathbf{r}'_\perp)|\psi(\mathbf{r}'_\perp,t)|^2\psi(\mathbf{r}_\perp,t).\end{aligned} \tag{B.15}$$

In real space, we can express the 2D DDI potential as

$$U_{dd}^{2D}(\mathbf{r}_\perp-\mathbf{r}'_\perp) = \int \mathrm{d}u\,\frac{\mu_0\mu_m^2}{4\pi}\frac{1}{\sqrt{2\pi}l_z}\frac{|\mathbf{r}_\perp-\mathbf{r}'_\perp|^2-2u^2}{\left[|\mathbf{r}_\perp-\mathbf{r}'_\perp|^2+u^2\right]^{5/2}}\exp\left\{-\frac{1}{2}\frac{u^2}{l_z^2}\right\}. \tag{B.16}$$

Since this expression still involves an integral, which is numerically expensive to evaluate at every iteration, we further analyze above expression in Fourier space. Here, the DDI potential after integrating out the z degree of freedom reads

$$\tilde{U}_{dd}^{2D}(\mathbf{k}_\perp) = \int \frac{\mathrm{d}k_z}{2\pi}\tilde{U}_{dd}(\mathbf{k}_\perp,k_z)e^{-\frac{1}{2}k_z^2l_z^2}, \tag{B.17}$$

and we can use the well-known Fourier transform of the DDI potential in three dimensions [47],

$$U_{dd}(\mathbf{r}_\perp, z) = \frac{\mu_0\mu_m^2}{4\pi}\frac{1-3z^2/|\mathbf{r}|^2}{|\mathbf{r}|^3} \xrightarrow{\mathcal{F}} \tilde{U}_{dd}(\mathbf{k}_\perp, k_z) = \frac{\mu_0\mu_m^2}{3}\left(\frac{3k_z^2}{|\mathbf{k}|^2}-1\right), \tag{B.18}$$

to explicitly evaluate the k_z integral. We find

$$\tilde{U}_{dd}^{2D}(\mathbf{k}_\perp) = \int \frac{\mathrm{d}k_z}{2\pi}\frac{\mu_0\mu_m^2}{3}\left(\frac{3k_z^2}{|\mathbf{k}|^2}-1\right)e^{-\frac{1}{2}k_z^2 l_z^2} = \frac{\mu_0\mu_m^2}{3}\int\frac{\mathrm{d}k_z}{2\pi}\frac{2k_z^2-|k_\perp|^2}{k_z^2+|\mathbf{k}_\perp|^2}e^{-\frac{1}{2}k_z^2 l_z^2}. \tag{B.19}$$

The appearing fraction of sums of squared momenta can be split using polynomial long division,

$$\frac{2k_z^2-|\mathbf{k}_\perp|^2}{k_z^2+|\mathbf{k}_\perp|^2} = 2-3\frac{|\mathbf{k}_\perp|^2}{k_z^2+|\mathbf{k}_\perp|^2}, \tag{B.20}$$

and the integration bounds can be changed by symmetry of integration, $\int_{-\infty}^{\infty}\mathrm{d}k_z \to 2\int_0^\infty \mathrm{d}k_z$, to obtain

$$\begin{aligned}\int \mathrm{d}k_z \frac{2k_z^2-|\mathbf{k}_\perp|^2}{k_z^2+|\mathbf{k}_\perp|^2}e^{-\frac{1}{2}k_z^2 l_z^2} &= 2\int \mathrm{d}k_z\, e^{-\frac{1}{2}k_z^2 l_z^2} - 6\,|\mathbf{k}_\perp|^2\int_0^\infty \mathrm{d}k_z \frac{e^{-\frac{1}{2}k_z^2 l_z^2}}{k_z^2+|\mathbf{k}_\perp|^2}\\ &= 2\frac{\sqrt{2\pi}}{l_z} - 6\,|\mathbf{k}_\perp|^2\frac{\pi}{2\,|\mathbf{k}_\perp|^2}\operatorname{erfc}\left(\frac{|\mathbf{k}_\perp|\,l_z}{\sqrt{2}}\right)e^{\frac{1}{2}|\mathbf{k}_\perp|^2 l_z^2}\\ &= \frac{\sqrt{2\pi}}{l_z}\left[2-3\sqrt{\pi}\frac{|\mathbf{k}_\perp|\,l_z}{\sqrt{2}}\operatorname{erfcx}\left(\frac{|\mathbf{k}_\perp|\,l_z}{\sqrt{2}}\right)\right].\end{aligned} \tag{B.21}$$

Here, $\operatorname{erfcx}(k) = e^{k^2}\operatorname{erfc}(k)$ denotes the exponentially scaled complementary error function. The non-trivial k_z-integral is of known form and may be found e.g. in [79]. Collecting all terms results in

$$\tilde{U}_{dd}^{2D}(\mathbf{k}_\perp) = \frac{\mu_0\mu_m^2}{3}\frac{1}{\sqrt{2\pi}l_z}\left[2-3\sqrt{\pi}\frac{|\mathbf{k}_\perp|\,l_z}{\sqrt{2}}\operatorname{erfcx}\left(\frac{|\mathbf{k}_\perp|\,l_z}{\sqrt{2}}\right)\right]. \tag{B.22}$$

C Numerical prerequisites

C.1 Variable transformation to computational units

We introduce the dimensionless computational units $\tilde{t} = \omega_0 t$, $\tilde{l} = l/l_0$ to make the eGPE dimensionless and divide Eq. (2.17) by $\hbar\omega_0$. Then, term by term, we have

$$\frac{1}{\hbar\omega_0}i\hbar\frac{\partial\psi}{\partial t} = i\frac{\partial\psi}{\partial(\omega_o t)} = i\frac{\psi}{\partial\tilde{t}}, \tag{C.1}$$

$$\begin{aligned}\frac{\mathcal{E}_z}{\hbar\omega_0} &= \frac{1}{4}\left(\frac{m\omega_z^2 l_z^2}{\hbar\omega_0} + \frac{\hbar^2}{m l_z^2 \hbar\omega_0}\right) = \frac{1}{4}\left(\frac{\omega_z^2}{\omega_0^2}\frac{l_z^2}{l_0^2} + \frac{l_0^2}{l_z^2}\right) \\ &\equiv \frac{1}{4}\gamma_z^2 \tilde{l}_z^2 + \frac{1}{4\tilde{l}_z^2} \equiv \mathcal{E}_z^{eff},\end{aligned} \tag{C.2}$$

$$\frac{1}{\hbar\omega_0}\left(-\frac{\hbar^2}{2m}\right)\left[\frac{\partial^2}{\partial x^2} + \frac{\partial^2}{\partial y^2}\right] = -\frac{l_0^2}{2}\left[\frac{\partial^2}{\partial x^2} + \frac{\partial^2}{\partial y^2}\right] = -\frac{1}{2}\left[\frac{\partial^2}{\partial \tilde{x}^2} + \frac{\partial^2}{\partial \tilde{y}^2}\right], \tag{C.3}$$

$$\frac{1}{\hbar\omega_0}\frac{g_s}{\sqrt{2\pi}l_z}|\psi|^2 = \frac{4\pi}{\sqrt{2\pi}}\frac{\hbar^2 a_s}{\hbar\omega_0 m l_z}|\psi|^2 = \frac{4\pi}{\sqrt{2\pi}}\frac{l_0 a_s}{\tilde{l}_z}|\psi|^2 = \frac{4\pi}{\sqrt{2\pi}}\frac{l_0^2 \tilde{a}_s}{\tilde{l}_z}|\psi|^2 \equiv g_s^{eff}|\psi|^2, \tag{C.4}$$

$$\begin{aligned}&\frac{1}{\hbar\omega_0}\sqrt{\frac{2}{5}}\frac{\gamma_{QF}}{\pi^{3/4} l_z^{3/2}}|\psi|^3 = \sqrt{\frac{2}{5}}\frac{32\pi^{1/2}}{3\pi^{3/4}}\frac{g_s a_s^{3/2}}{\hbar\omega_0 l_z^{3/2}}\mathcal{Q}_5(\epsilon_{dd})|\psi|^3 \\ &= \sqrt{\frac{2}{5}}\frac{128\pi^{3/2}}{3\pi^{3/4}}\frac{\hbar^2 a_s^{5/2}}{\hbar\omega_0 m l_z^{3/2}}\mathcal{Q}_5(\epsilon_{dd})|\psi|^3 = \sqrt{\frac{2}{5}}\frac{128\pi^{3/4}}{3}\frac{l_0^{1/2} a_s^{5/2}}{\tilde{l}_z^{3/2}}\mathcal{Q}_5(\epsilon_{dd})|\psi|^3 \\ &= \sqrt{\frac{2}{5}}\frac{128\pi^{3/4}}{3}\frac{l_0^3 \tilde{a}_s^{5/2}}{\tilde{l}_z^{3/2}}\mathcal{Q}_5(\epsilon_{dd})|\psi|^3 \equiv \gamma_{QF}^{eff}|\psi|^3,\end{aligned} \tag{C.5a}$$

$$\begin{aligned}&\Big[\text{Erratum: } \frac{1}{\hbar\omega_0}\sqrt{\frac{2}{5}}\frac{\gamma_{QF}}{\pi^{3/4} l_z^{3/2}}|\psi|^3 = \sqrt{\frac{2}{5}}\frac{32\pi^{-1/2}}{3\pi^{3/4}}\frac{g_s a_s^{3/2}}{\hbar\omega_0 l_z^{3/2}}\mathcal{Q}_5(\epsilon_{dd})|\psi|^3 \\ &= \sqrt{\frac{2}{5}}\frac{128\pi^{1/2}}{3\pi^{3/4}}\frac{\hbar^2 a_s^{5/2}}{\hbar\omega_0 m l_z^{3/2}}\mathcal{Q}_5(\epsilon_{dd})|\psi|^3 = \sqrt{\frac{2}{5}}\frac{128\pi^{-1/4}}{3}\frac{l_0^{1/2} a_s^{5/2}}{\tilde{l}_z^{3/2}}\mathcal{Q}_5(\epsilon_{dd})|\psi|^3 \\ &= \sqrt{\frac{2}{5}}\frac{128}{3\pi^{1/4}}\frac{l_0^3 \tilde{a}_s^{5/2}}{\tilde{l}_z^{3/2}}\mathcal{Q}_5(\epsilon_{dd})|\psi|^3 \equiv \gamma_{QF}^{eff}|\psi|^3,\Big]\end{aligned} \tag{C.5b}$$

$$\begin{aligned}&\frac{1}{\hbar\omega_0}\int \mathrm{d}^2\mathbf{r}'_\perp U_{dd}^{2D}(\mathbf{r}_\perp - \mathbf{r}'_\perp)|\psi(\mathbf{r}'_\perp)|^2 \\ &= \frac{1}{\hbar\omega_0}\frac{\mu_0\mu_m^2}{4\pi}\frac{1}{\sqrt{2\pi}l_z}\int \mathrm{d}^2\mathbf{r}'_\perp \int \mathrm{d}u \frac{|\mathbf{r}_\perp - \mathbf{r}'_\perp|^2 - 2u^2}{\left[|\mathbf{r}_\perp - \mathbf{r}'_\perp|^2 + u^2\right]^{5/2}}\exp\left\{-\frac{1}{2}\frac{u^2}{l_z^2}\right\}|\psi(\mathbf{r}'_\perp)|^2 \\ &= \frac{1}{\hbar\omega_0}\frac{12\pi\hbar^2 a_{dd}}{4\pi m}\frac{1}{\sqrt{2\pi}l_z}\int \mathrm{d}^2\left(l_0^2\tilde{\mathbf{r}}'_\perp\right)\int \mathrm{d}\left(l_0\tilde{u}\right)\frac{l_0^2}{l_0^5}\frac{|\tilde{\mathbf{r}}_\perp - \tilde{\mathbf{r}}'_\perp|^2 - 2\tilde{u}^2}{\left[|\tilde{\mathbf{r}}_\perp - \tilde{\mathbf{r}}'_\perp|^2 + \tilde{u}^2\right]^{5/2}}\exp\left\{-\frac{1}{2}\frac{\tilde{u}^2}{\tilde{l}_z^2}\right\}|\psi(\tilde{\mathbf{r}}'_\perp)|^2 \\ &= \frac{3}{\sqrt{2\pi}}\frac{\tilde{a}_{dd} l_0^2}{\tilde{l}_z}\int \mathrm{d}\tilde{\mathbf{r}}'_\perp \int \mathrm{d}\tilde{u}\frac{|\tilde{\mathbf{r}}_\perp - \tilde{\mathbf{r}}'_\perp|^2 - 2\tilde{u}^2}{\left[|\tilde{\mathbf{r}}_\perp - \tilde{\mathbf{r}}'_\perp|^2 + \tilde{u}^2\right]^{5/2}}\exp\left\{-\frac{1}{2}\frac{\tilde{u}^2}{\tilde{l}_z^2}\right\}|\psi(\tilde{\mathbf{r}}'_\perp)|^2 \\ &\equiv \int \mathrm{d}^2\tilde{\mathbf{r}}'_\perp U_{dd}^{2D,eff}(\tilde{\mathbf{r}}_\perp - \tilde{\mathbf{r}}'_\perp)|\psi(\tilde{\mathbf{r}}'_\perp)|^2.\end{aligned} \tag{C.6}$$

After dropping the tildes and collecting all terms, this yields the dimensionless 2D eGPE quoted in Eq. (3.1) after adding in the chemical potential. Note that numerical coefficients in the terms describing contact interactions and dipolar interactions and quantum fluctuations carry additional powers of l_0, e.g. $[g_s^{eff}] = [l_0^2] = 2$, where $[\cdot]$ denotes the length dimension. They are needed to cancel dimension-full normalization constants of $\psi(x, y, t)$. Since $\int \mathrm{d}x\mathrm{d}y\,|\psi(x, y, t)|^2 = N$ and $[N] = 0$, we conclude $[|\psi(x, y, t)|] = \left[l_0^{-1}\right] = -1$ as

$[dx] = [dy] = [l_0] = 1$, so each power of $|\psi(x, y, t)|$ requires a power of l_0 to get a dimensionless equation, such that e.g. $[g_s^{eff}|\psi|^2] = 2 - 2 = 0$.

C.2 Numerical error of the split-step Fourier method

To exploit numerical advantages by evaluating the kinetic operator in Fourier space, the time evolution operator $\hat{U}(\Delta t) = e^{-i\hat{H}\Delta t}$ has to be factorized into the components of the Hamiltonian. Denoting $i\hat{X} = \hat{D}\Delta t$ and $i\hat{Y} = \left(\hat{L} + \hat{N} + \hat{V}_{dd}\right)\Delta t$, the time evolution operator reads

$$\hat{U}(\Delta t) = \exp\left\{\hat{X} + \hat{Y}\right\}. \tag{C.7}$$

However, in Eq. (3.7), we claim the time evolution operator to take the form

$$\hat{U}(\Delta t) = \exp\left\{\frac{1}{2}\hat{X}\right\} \cdot \exp\left\{\hat{Y}\right\} \cdot \exp\left\{\frac{1}{2}\hat{X}\right\} \tag{C.8}$$

up to second order in Δt. Since in general the appearing operators do not commute, the Baker-Campbell-Hausdorff-Dynkin formula [80]

$$\begin{aligned}\exp\{\hat{A}\} \cdot \exp\{\hat{B}\} = \exp\Bigg\{ &\hat{A} + \hat{B} + \frac{1}{2}\Big[\hat{A}, \hat{B}\Big] + \frac{1}{12}\Big[\hat{A}, \Big[\hat{A}, \hat{B}\Big]\Big] - \frac{1}{12}\Big[\hat{B}, \Big[\hat{A}, \hat{B}\Big]\Big] \\ &+ \mathcal{O}(\hat{A}^2\hat{B}^2) + \mathcal{O}(\hat{A}^3\hat{B}) + \mathcal{O}(\hat{A}\hat{B}^3)\Bigg\}\end{aligned} \tag{C.9}$$

has to be applied to show the equivalence of these expressions at relevant order. Since both $\hat{X}$ and $\hat{Y}$ are conveniently of order Δt, we obtain

$$\begin{aligned}\exp\left\{\frac{1}{2}\hat{X}\right\} \cdot \exp\left\{\hat{Y}\right\} \cdot \exp\left\{\frac{1}{2}\hat{X}\right\} &= \exp\Bigg\{\frac{1}{2}\hat{X} + \hat{Y} + \frac{1}{2}\cdot\frac{1}{2}\Big[\hat{X}, \hat{Y}\Big] + \frac{1}{12}\Bigg(\frac{1}{2}\cdot\frac{1}{2}\Big[\hat{X}, \Big[\hat{X}, \hat{Y}\Big]\Big] \\ &\quad - \frac{1}{2}\Big[\hat{Y}, \Big[\hat{X}, \hat{Y}\Big]\Big]\Bigg) + \mathcal{O}(\Delta t^4)\Bigg\} \cdot \exp\left\{\frac{1}{2}\hat{X}\right\} \\ &= \exp\Bigg\{\hat{X} + \hat{Y} + \frac{1}{4}\Big[\hat{X}, \hat{Y}\Big] + \frac{1}{12}\Bigg(\frac{1}{4}\Big[\hat{X}, \Big[\hat{X}, \hat{Y}\Big]\Big] - \frac{1}{2}\Big[\hat{Y}, \Big[\hat{X}, \hat{Y}\Big]\Big]\Bigg) + \frac{1}{4}\Big[\hat{Y}, \hat{X}\Big] \\ &\quad + \frac{1}{16}\Big[\Big[\hat{X}, \hat{Y}\Big], \hat{X}\Big] + \frac{1}{12}\Bigg(\frac{1}{4}\Big[\hat{X} + 2\hat{Y}, \Big[\hat{Y}, \hat{X}\Big]\Big] - \frac{1}{4}\Big[\hat{X}, \Big[\hat{Y}, \hat{X}\Big]\Big]\Bigg) + \mathcal{O}(\Delta t^4)\Bigg\} \\ &= \exp\Bigg\{\hat{X} + \hat{Y} + \frac{1}{12}\Bigg(\frac{1}{4}\Big[\hat{X}, \Big[\hat{X}, \hat{Y}\Big]\Big] - \frac{1}{2}\Big[\hat{Y}, \Big[\hat{X}, \hat{Y}\Big]\Big] + \underbrace{\frac{3}{4}\Big[\Big[\hat{X}, \hat{Y}\Big], \hat{X}\Big]}_{=-\frac{3}{4}\left[\hat{X}, \left[\hat{X}, \hat{Y}\right]\right]} \\ &\quad + \frac{1}{4}\Big[\hat{X}, \Big[\hat{Y}, \hat{X}\Big]\Big] + \overbrace{\frac{1}{2}\Big[\hat{Y}, \Big[\hat{Y}, \hat{X}\Big]\Big]}^{=-\frac{1}{2}\left[\hat{Y}, \left[\hat{X}, \hat{Y}\right]\right]} - \frac{1}{4}\Big[\hat{X}, \Big[\hat{Y}, \hat{X}\Big]\Big]\Bigg) + \mathcal{O}(\Delta t^4)\Bigg\}\end{aligned} \tag{C.10}$$

$$
\begin{aligned}
&= \exp\left\{ \hat{X} + \hat{Y} + \frac{1}{12} \left(\underbrace{-\frac{1}{2}\left[\hat{X}, \left[\hat{X}, \hat{Y}\right]\right]}_{=\left[\left[\hat{X},\hat{Y}\right],\frac{1}{2}\hat{X}\right]} \underbrace{-\left[\hat{Y}, \left[\hat{X}, \hat{Y}\right]\right]}_{=\left[\left[\hat{X},\hat{Y}\right],\hat{Y}\right]} \right) + \mathcal{O}(\Delta t^4) \right\} \\
&= \exp\left\{ \hat{X} + \hat{Y} + \frac{1}{12}\left[\left[\hat{X}, \hat{Y}\right], \frac{1}{2}\hat{X} + \hat{Y}\right] + \mathcal{O}(\Delta t^4) \right\},
\end{aligned}
$$

by exploiting the usual commutator rules

$$
\begin{gathered}
\left[\hat{A}, \hat{B}\right] \equiv \hat{A}\hat{B} - \hat{B}\hat{A} = -\left(\hat{B}\hat{A} - \hat{A}\hat{B}\right) = -\left[\hat{B}, \hat{A}\right], \\
\left[\hat{A}, \hat{B}\right] + \left[\hat{A}, \hat{C}\right] = \hat{A}\hat{B} - \hat{B}\hat{A} + \hat{A}\hat{C} - \hat{C}\hat{A} = \hat{A}\left(\hat{B} + \hat{C}\right) - \left(\hat{B} + \hat{C}\right)\hat{A} = \left[\hat{A}, \hat{B} + \hat{C}\right], \\
a\left[\hat{A}, \hat{B}\right] = a\left(\hat{A}\hat{B} - \hat{B}\hat{A}\right) = \left(a\hat{A}\right)\hat{B} - \hat{B}\left(a\hat{A}\right) = \left[a\hat{A}, \hat{B}\right],
\end{gathered}
\tag{C.11}
$$

for generic operators $\hat{A}$, $\hat{B}$, $\hat{C}$ and scalar a. This concludes the equivalence of Eq. (C.7) and Eq. (C.8) up to and including $\mathcal{O}(\Delta t^2)$, with leading deviation given by $1/12 \cdot \left[\left[\hat{X}, \hat{Y}\right], \hat{X}/2 + \hat{Y}\right]$. Putting back in the definition of $\hat{X}$ and $\hat{Y}$, we find

$$
\begin{aligned}
&\exp\left\{-\frac{i}{2}\hat{D}\Delta t\right\} \cdot \exp\left\{-i\left(\hat{L} + \hat{N} + \hat{V}_{dd}\right)\Delta t\right\} \cdot \exp\left\{-\frac{i}{2}\hat{D}\Delta t\right\} \\
&\quad = \exp\Bigg\{ -i\left(\hat{D} + \hat{L} + \hat{N} + \hat{V}_{dd}\right)\Delta t \\
&\qquad + \frac{1}{12}(-i)^3\left[\left[\hat{D}, \left(\hat{L} + \hat{N} + \hat{V}_{dd}\right)\right], \frac{1}{2}\hat{D} + \left(\hat{L} + \hat{N} + \hat{V}_{dd}\right)\right]\Delta t^3 + \mathcal{O}(\Delta t^4) \Bigg\} \\
&\quad = \exp\left\{ -i\hat{H}\Delta t + \frac{i}{12}\left[\left[\hat{D}, \left(\hat{L} + \hat{N} + \hat{V}_{dd}\right)\right], \frac{1}{2}\hat{D} + \left(\hat{L} + \hat{N} + \hat{V}_{dd}\right)\right]\Delta t^3 \right\} + \mathcal{O}(\Delta t^4) \\
&\quad = \hat{U}(\Delta t) + \mathcal{O}(\Delta t^3),
\end{aligned}
\tag{C.12}
$$

so the time evolution operator can be expressed as $\hat{U}(\Delta t) = e^{-\frac{i}{2}\hat{D}\Delta t} e^{-i\left(\hat{L}+\hat{N}+\hat{V}_{dd}\right)\Delta t} e^{-\frac{i}{2}\hat{D}\Delta t}$ in $\mathcal{O}(\Delta t^2)$. Applying Fourier transforms after the appropriate steps yields the split-step Fourier method equation Eq. (3.7).

C.3 Finding vortices in MATLAB

To analyze the number and distance distributions of vortices in a supersolid, it is integral to accurately find vortices and their positions first. This is done numerically by the algorithm presented below. It is implemented on MATLAB, release R2023a, and it finds vortices and the sign of their topological charge by periodically subtracting shifted copies of the phase of the wavefunction `psi`. A phase defect is identified if the modulus of the resulting phase-winding exceeds 2π within the numerical tolerance $\epsilon = 2\pi - 6.2 \approx 0.083$ for a 2×2 patch of condensate. In the end, vortex positions are expressed in terms of the space grid `X` and `Y`, and grid spacing `dx`, `dy`, in harmonic oscillator units. Important parts

of this algorithm are courtesy of W. Kirkby.

```
%% find vortex positions and signs of vortex charge
% compute phase and set tolerance
argpsi = angle(psi);
tolerance = 6.2;
% circshift phase array
argshift_1 = circshift(argpsi,-1,1);
argshift_2 = circshift(argpsi,-1,2);
argshift_3 = circshift(argpsi,[-1,-1]);
% periodically subtract shifted phase
Subs_1 = mod(argpsi - argshift_2 + pi, 2*pi) - pi;
Subs_2 = mod(argshift_2 - argshift_3 + pi, 2*pi) - pi;
Subs_3 = mod(argshift_3 - argshift_1 + pi, 2*pi) - pi;
Subs_4 = mod(argshift_1 - argpsi + pi, 2*pi) - pi;
% accumulate phase winding
phasesum = Subs_1 + Subs_2 + Subs_3 + Subs_4;
% check if phasewinding excceds 2pi within tolerance
vortexarray = double(abs(phasesum) > tolerance);
% compute sign of vortices
signarray = sign(phasesum) .* vortexarray;
% find vortex indices
vortex_indx = find(vortexarray);
% relate vortex indices to grid coordinates
x_positions = (2*X(vortex_indx)+dx)/2;
y_positions = (2*Y(vortex_indx)+dy)/2;
```

C.4 Extracting lattice structures in MATLAB

This subsection outlines the algorithm used to detect lattice defects in the droplet crystal lattice. It has been implemented on MATLAB, release R2023a. Given a wavefunction `psi`, all local density maxima are identified and filtering constraints are applied. We enforce a minimum density `maxima_treshold`, and dominance within `minsep` after filtering out high momentum modes using a Gaussian convolution filter with width `sigma`. `sigma`, `maxima_threshold` and `minsep` are parameters to be determined by extensive testing. We use `sigma` $= 2$, `maxima_treshold` $= 1.2$ and `minsep` $= 2$ μm. Fig. C.1 illustrates the effect of enforcing a minimum separation between vortices. Without applying this filtering criterion, single droplets are frequently identified as two droplets, which induces multiple fake lattice defects. However, overconstraining the droplet identification algorithm by enforcing too large minimum separations leads to fake lattice defects as well, as some existing droplets are no longer identified.

In the honeycomb phase, we enforce a maximum density `minima_threshold` $= 0.75$, i.e.

local density minima are only considered to be lattice points if their density does not exceed 75% of the average density.

```
%% Identify lattice structure in droplet phase
% compute density from wavefunction
density = psi.^2;
% filter high momentum modes
smoothed_density = imgaussfilt(density, sigma);
% pad smoothed density to account for periodic boundary
    conditions
smoothed_density = padarray(smoothed_density, [70 70], 'circular'
    );
% enforce minimum density
maxima = imregionalmax(smoothed_density, 8) & (smoothed_density >
     maxima_threshold);
% enforce minimum separation
% get row and colums index of maxima
[rows, cols] = find(maxima);
% combine maxima positions and values and sort by value
maxima_tensor = sortrows([rows, cols, smoothed_density(maxima)],
    -3);
% compute pairwise distance
maxima_dist = squareform(pdist(maxima_tensor(:, 1:2)));
% mask all maxima to be valid
valid_maxima = true(size(maxima_tensor, 1), 1);
% find maxima closer than a minimum separation and exploit
    symmetry
% of distance metric through triu()
[~, colIdx] = find(triu(maxima_dist < minsep, 1));
% mask maximum with lower density as false
valid_maxima(colIdx) = false;
% retain only valid maxima
maxima = maxima_tensor(valid_maxima, 1:2);
```

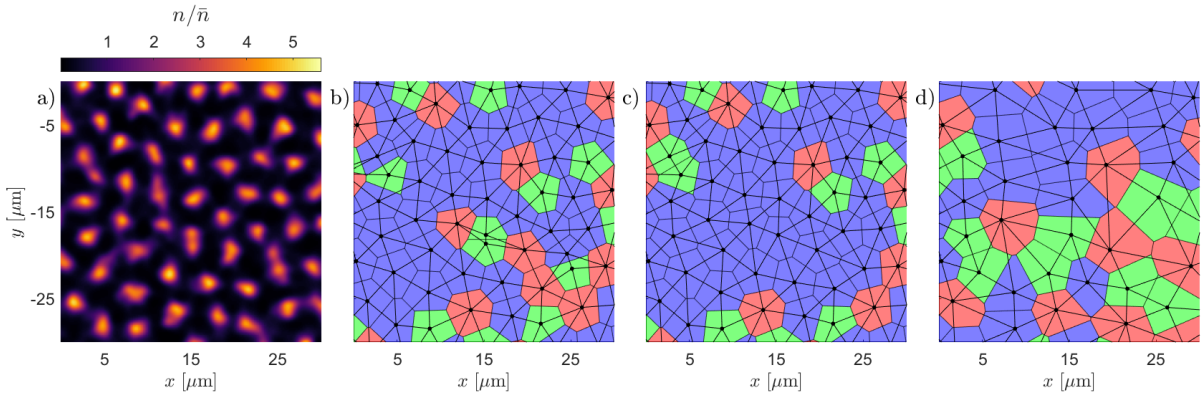

Figure C.1: Influence of the minimum separation filtering criterion on the calculation of the lattice structure. Panel a) shows the particle area density distribution of a droplet phase condensate 150 ms post quench in a $30 \times 30\,\mu\text{m}^2$ subdomain of the simulated grid. Panels {b), c), d)} display the corresponding Voronoi tesselations with different enforced minimum droplet separations $\texttt{minsep} = \{0, 2, 4\}\mu$m. Blue Voronoi cells signify neutral density maxima, whereas green cells distinguish negatively charged maxima from positively charged maxima in red cells. The Delaunay triangulation and the extracted positions of the density maxima are plotted in black atop the Voronoi tesselation.

D Extended perspective on the lattice defect decay

This section holds supplementary material regarding the defect decay and bond-order correlation analysis.

D.1 Scaling regimes of the algebraic decay of $N_D(t)$ across the parameter space

In Fig. D.1, we report the decay of the lattice defect number for all parameter combinations $\{\bar{n}, a_s\}$ considered in this thesis in both the droplet and honeycomb phase. We make the following observations:
Firstly, all states in the droplet phase experience two different algebraic scaling regimes. However, the transition time between the scaling regimes increases with a decrease in s-wave scattering length.
Secondly, the smaller the s-wave scattering length, the earlier our droplet finding algorithm tracks the formation of the lattice structure in quenches with uniform initialization. This implies that the condensate reaches the necessary density modulation for the droplet identification constraints faster if the ground state contrast is high as the ground state contrast is close to unity in these deep quenches (see also Fig. 4.2, panels d) and e)). Systems with large ground state contrasts are far out of equilibrium if they are initialized with a nearly unmodulated density distribution. A faster increase in density modulation

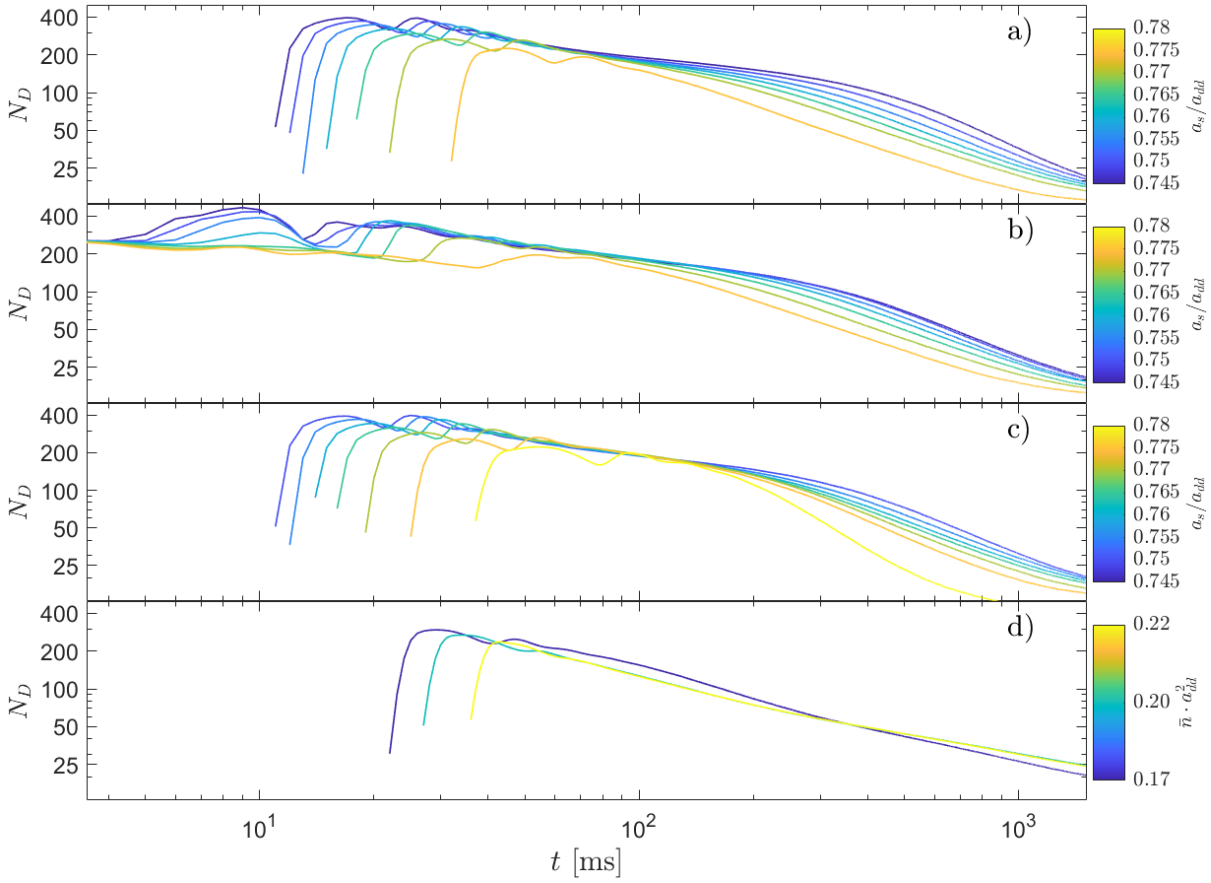

Figure D.1: Decay of the lattice defect number for different initial states and parameter combinations. Data shown in panels a) and b) corresponds to initial states with an average density of $\bar{n} \cdot a_{dd}^2 = 0.075$ and uniform and square lattice initialization, respectively. Panel c) shows the decay of the defect number at the average density $\bar{n} \cdot a_{dd}^2 = 0.085$ and uniform initialization. As panels a) through c) show the decay of the lattice defect number in the droplet phase, we use color to distinguish quenches with different s-wave scattering lengths. In panel d) we show the defect decay in the honeycomb phase at $a_s/a_{dd} = 0.78$ and with uniform initialization. Here, color serves to distinguish initial states with different average densities. Statistical errors are omitted for the purpose of readability.

is thus expected.

Thirdly, if systems are initialized in the square lattice initialization scheme, the lattice formation process can be tracked immediately post quench as the density modulation fulfills the filtering constraints of the droplet finding algorithm by construction of the initial state. Here, we seed droplets directly into the initial state. By arranging the droplets in a square lattice, these initial states have a non-vanishing lattice defect number post quench. The lattice defect number shows an oscillatory behavior initially, and then transitions to the same two-regime algebraic scaling observable for droplet states with uniform initialization.

Fourthly, in the honeycomb phase, the data does not clearly show two distinct scaling regimes but a mostly uniform algebraic scaling of the lattice defect number. However, this does not decisively rule out a two-regime scaling behavior. The second scaling regime

might be obscured either by transition times larger than the latest simulated time or by the initial lattice formation process, i.e. the first algebraic scaling regime might be too short to reliably observe in quenches with the considered average densities and under the density constraints enforced in the tracking of density minima.
Note that the appearance of two different scaling regimes is commonplace in Bose gases. The mean inter-vortex distance $l_v(t)$ is found to scale as $l_v(t) \propto t^{\beta}$, where the scaling exponent transitions from $\beta = 1/5$ to $\beta = 1/2$ in dilute Bose gases in the uniform superfluid regime. Additionally, the vortex number in these systems scales as $N_v(t) \propto t^{-2\beta}$, with the same transition of β from an early-time to a late-time scaling regime. In these systems, the transition of the scaling exponent between the two scaling regimes can be traced back to the existence of two different fixed points, c.f. [19, 20].

D.2 Bootstrapping

The idea of bootstrapping is to get an estimator for a fitting parameter and its error by doing repeated fits over resampled versions of the original dataset. This approach does not make assumptions on the underlying probability distribution, and specifically, it does not require Gaussian errors. We validate this approach for our defect decay data in Fig. D.2 by reporting the probability density distributions to find a given α and t^* in an individual bootstrap fit to a resampled dataset. Their distributions closely follow normal distributions. This justifies determining estimators for the true values of α and t^* by taking their respective means over all bootstrap fits, and estimating their error by taking the standard deviation of their respective distributions.
Since we consider fitting ranges of $\mathcal{O}(10^3)$ ms with millisecond time steps, it is impossible to consider all possible unordered resamplings with replacements when keeping the sample size constant. Their number is given by $\binom{2n-1}{n}$[11], which for $\mathcal{O}(n) = 10^3$ grows beyond all numerically reasonable bounds. Using Stirling's formula [81], we can approximate the total number of possible resamplings with replacement as

$$\begin{aligned}\log_{10}\binom{2n-1}{n} &= \log_{10}\frac{(2n-1)!}{n!(n-1)!} \approx \log_{10}\frac{\sqrt{2\pi\,(2n-1)}\left(\frac{2n-1}{e}\right)^{2n-1}}{\sqrt{2\pi n}\left(\frac{n}{e}\right)^{n}\sqrt{2\pi\,(n-1)}\left(\frac{n-1}{e}\right)^{n-1}} \\ &= (2n-1)\log_{10}(2n-1) - n\log_{10} n - (n-1)\log_{10}(n-1) \\ &\quad + \frac{1}{2}\log_{10}\left(\frac{2n-1}{2\pi n\,(n-1)}\right) \overset{n=10^3}{\approx} 600.\end{aligned} \tag{D.1}$$

Therefore, we resort to an approach known as Monte Carlo sampling bootstrap, where we generate a random subset of all possible resamplings and compute α and t^* from these. This is a tradeoff between computational time and accuracy. Results presented in the present work have been obtained by generating at least 500 resamplings, with deviations

[11] The problem condenses to drawing n time indices from $N = n$ possible time indices, so there are $\binom{N+n-1}{n} = \binom{2n-1}{n}$ possibilities.

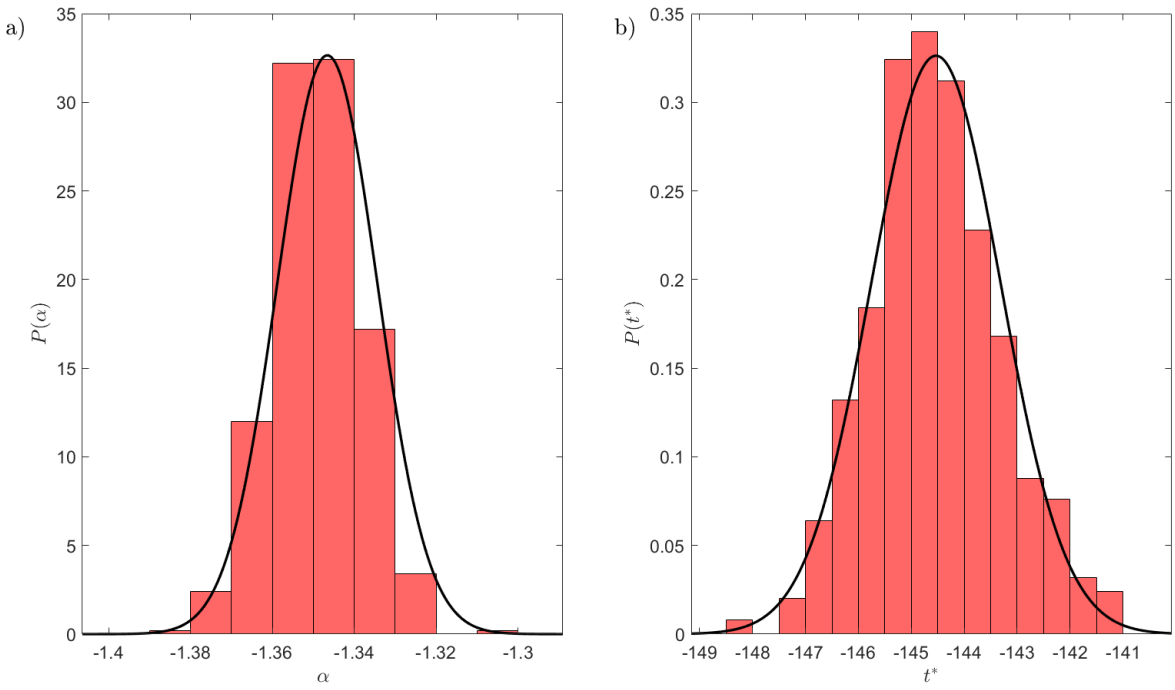

Figure D.2: Probability density distributions to find a given α (panel a)) and t^* (panel b)) in the bootstrap results. Black lines represent normal distributions fitted to the results. Data taken for $\bar{n} \cdot a_{dd}^2 = 0.075$, $a_s = 0.755 a_{dd}$ and a square lattice initial state. Results for 500 resamplings.

from this minimum pointed out in the respective figures.

D.3 Time evolution of topological lattice defect charge

The total topological charge is given by $Q_{tot} = \sum_i Q_i$, where the sum runs over all lattice points i. As discussed in Sec. 4.3, Q_{tot} is expected to vanish due to periodicity. This matches closely our observations depicted in Fig. D.3, panels a), c) and e). The only notable exception to this can be observed at early times when using the square lattice initialization scheme. However, the topological charge is not expected to vanish in this limit since in a square lattice, all lattice points carry the charge $Q_i = -2$. Our initial state is still neutral due to the Gaussian shifts we apply to the true droplet positions around the unit cell centers. Charge is briefly generated as the condensate evolves, but it vanishes after approximately 100 ms. A vanishing total charge still leaves the possibility for asymmetric charge generation as a topological defect with $Q = 2$ could be compensated for by two lattice defects with $Q = -1$. To rule out this possibility, we also show the evolution of signed squared charge,

$$Q_+^2 - Q_-^2 = \sum\nolimits_i^+ Q_i^2 - \sum\nolimits_j^- Q_j^2. \tag{D.2}$$

Here, the sum $\sum_i^+$ runs over all defects with $Q_i > 0$, and $\sum_j^-$ sums all defects subject to $Q_j < 0$. Since we add squares of charges but keep their sign, we can rule out asymmetric

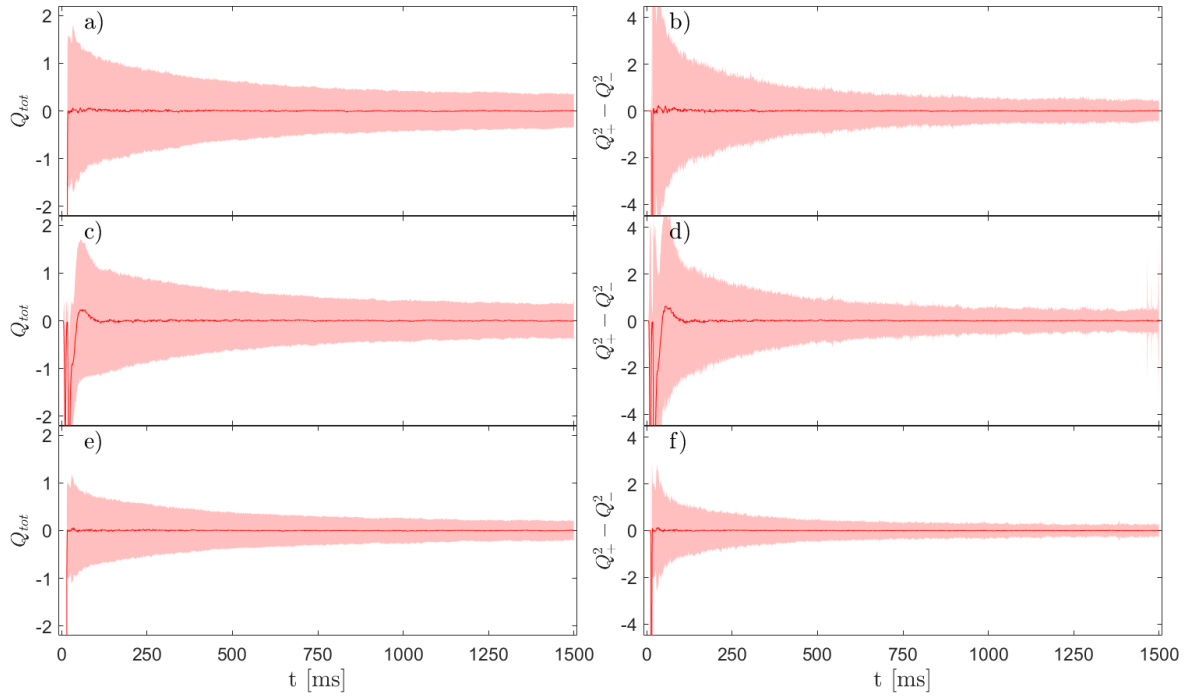

Figure D.3: Time evolution of topological charge for $a_s/a_{dd} = 0.76$. Panels on the left side show the time evolution of total charge, while panels on the right side present the evolution of signed squared charge. Panels top to bottom show data recorded for $\bar{n} \cdot a_{dd}^2 = 0.075$ with uniform initialization, $\bar{n} = 0.075$ with lattice initialization and $\bar{n} = 0.085$ with uniform initialization, respectively. Solid lines represent the means and shaded regions the standard deviations taken across all 3000 quenches.

charge generation as the total signed squared charge vanishes with the same exceptions as above (see Fig. D.3, panels b), d) and f)). This empirical result closely follows our observation that defects with more than unit charge are sparse.

D.4 Hexatic systems take II - the honeycomb phase

D.4.1 Angular susceptibility in the honeycomb phase

The honeycomb phase also represents a hexatic system, matching closely our observations in the droplet phase (Sec. 4.5). Fig. D.4 shows χ_6 distributions in the honeycomb phase for different subsystem sizes. We observe an increase of bond orientational order with time. Regardless of the size of the subsystem, the different χ_6 distributions indicate a homogeneous system as they are not the superposition of a fluid-like component and a solid-like component as expected for an inhomogeneous system. An increase in subsystem size causes an overall spread of the χ_6 distributions.

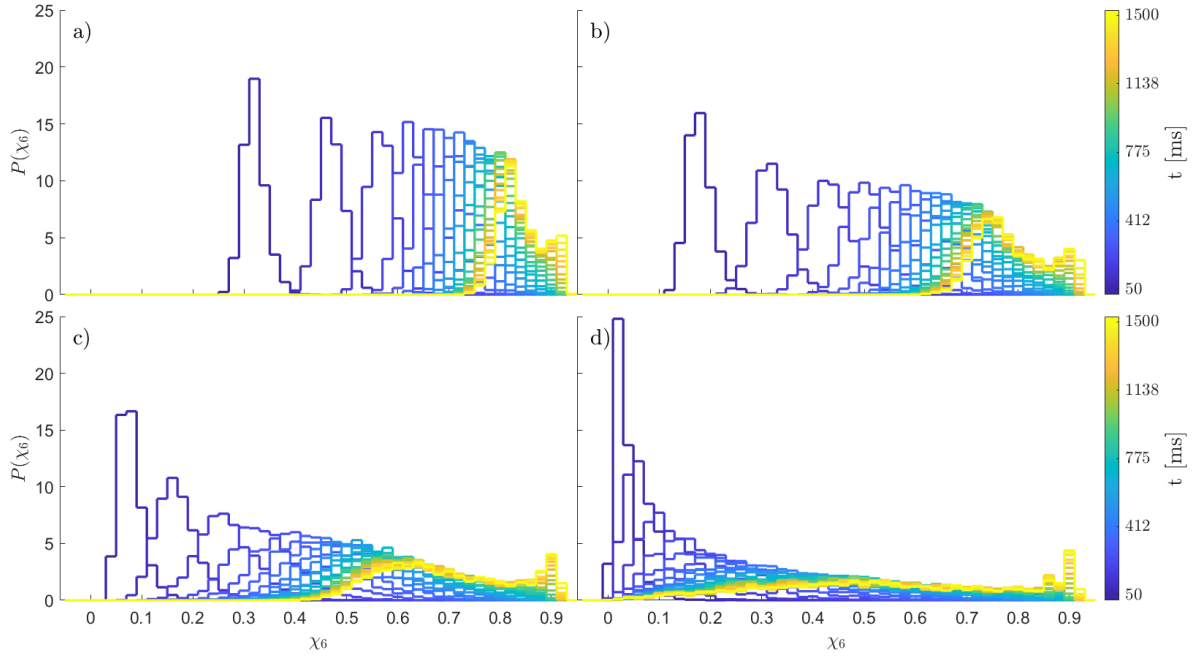

Figure D.4: Time evolution of χ_6 distributions for $\bar{n} \cdot a_{dd}^2 = 0.2$, $a_s/a_{dd} = 0.780$ and uniform initialization in the honeycomb phase. Panels a) through d) show χ_6 distributions recorded for increasing subsystems of size $l \times \sqrt{3} \cdot l$, where $l/l_x \in \{1, 2, 4, 8\}$.

D.4.2 Inter-defect distance in the honeycomb phase

We observe strong clustering of defects into pairs in the honeycomb phase as in the droplet phase. Similar to Fig. 4.8, we report the graph distance distribution to the nearest defect in Fig. D.5. The probability weight is concentrated in the bin representing separation by one edge, and the probability to find the next defect at more than one edge separation decreases rapidly.

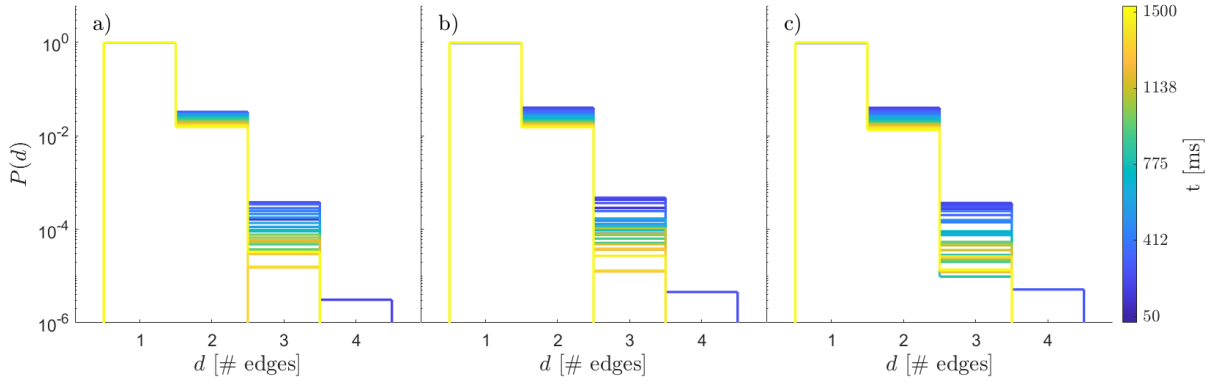

Figure D.5: Time evolution of graph distance distributions to the closest defect. Panels {a), b), c)} show data obtained with $\bar{n} \cdot a_{dd}^2 = \{0.17, 0.2, 0.22\}$ and $a_s/a_{dd} = 0.78$ with uniform initialization. Color distinguishes different times.